

This Document
Reproduced From
Best Available Copy

TECHNICAL INFORMATION SERIES

R65SD4

A STUDY OF THE REFLECTION AND
POLARIZATION CHARACTERISTICS OF SELECTED
NATURAL AND ARTIFICIAL SURFACES

K.C. GOULSON
E.L. GRAY
G.M. BOURICIUS

4.00
1.00
150 P
JUL 1964
TISIA E

SPACE SCIENCES
LABORATORY

MISSILE AND SPACE DIVISION

GENERAL  ELECTRIC

ARCHIVE COPY

619032

This Document
Reproduced From
Best Available Copy

SPACE SCIENCES LABORATORY
SPACE PHYSICS SECTION

A STUDY OF THE REFLECTION AND POLARIZATION
CHARACTERISTICS OF SELECTED NATURAL AND
ARTIFICIAL SURFACES

By

K. C. Coulson
E. L. Gray
G. M. Bouricius

Work supported by the U. S. Naval Ordnance Test Station,
China Lake, California under contract N123(60530)51172A.

R65SD4
May 1965

MISSILE AND SPACE DIVISION

GENERAL  ELECTRIC

This Document
Reproduced From
Best Available Copy

SPACE SCIENCES LABORATORY
MISSILE AND SPACE DIVISION

GENERAL ELECTRIC

TECHNICAL INFORMATION SERIES

AUTHOR K. L. Coulson E. L. Gray G. M. Bouricius	SUBJECT CLASSIFICATION Geophysics	NO. R64SD4 DATE May, 1965
TITLE A Study of the Reflection and Polarization Characteristics of Selected Natural and Artificial Surfaces		G. E. CLASS I GOV. CLASS Unclassified
REPRODUCIBLE COPY FILED AT MSD LIBRARY, DOCUMENTS LIBRARY UNIT, VALLEY FORGE SPACE TECHNOLOGY CENTER, KING OF PRUSSIA, PA.		NO. PAGES 147
SUMMARY <p>This report covers two aspects of the short wave regime of planetary radiation. First, extensive measurements of the reflection properties of a number of surfaces have been made, both the directional reflectance and the degree of polarization of the reflected radiation having been determined. It is found that most surfaces show pronounced "limb-brightening" for large angles of incidence, while for small angles of incidence the reflectance does not vary greatly with angle at which the surface is viewed. The degree of polarization shows a characteristic pattern for most surfaces, a maximum being located in the principal plane at 100° to 120° from the antisource direction and a small region of negative polarization being observed in the vicinity of the antisource direction. For most surfaces the reflectance increases and the maximum degree of polarization decreases with increasing wavelength.</p> <p>The second part of the research has been the introduction of the reflectance values into the theory of radiative transfer to determine the characteristics of the radiation field at high altitudes above the surface. It is seen that for the cases of clear and slightly turbid atmospheres the surface properties have a strong influence on the contrasts which would be observed from a high altitude vantage point. A possibility of using polarization characteristics to enhance contrasts is demonstrated.</p>		
KEY WORDS		

BY CUTTING OUT THIS RECTANGLE AND FOLDING ON THE CENTER LINE, THE ABOVE INFORMATION CAN BE FITTED INTO A STANDARD CARD FILE

AUTHOR K. L. Coulson E. L. Gray G. M. B. Bouricius

COUNTERSIGNED J. R. Hart

Abstract

This report covers two aspects of the short wave regime of planetary radiation. First, extensive measurements of the reflection properties of a number of surfaces have been made, both the directional reflectance and the degree of polarization of the reflected radiation having been determined. It is found that most surfaces show pronounced "limb-brightening" for large angles of incidence, while for small angles of incidence the reflectance does not vary greatly with angle at which the surface is viewed. The degree of polarization shows a characteristic pattern for most surfaces, a maximum being located in the principal plane at 100° to 120° from the antisource direction and a small region of negative polarization being observed in the vicinity of the antisource direction. For most surfaces the reflectance increases and the maximum degree of polarization decreases with increasing wavelength.

The second part of the research has been the introduction of the reflectance values into the theory of radiative transfer to determine the characteristics of the radiation field at high altitudes above the surface. It is seen that for the cases of clear and slightly turbid atmospheres the surface properties have a strong influence on the contrasts which would be observed from a high altitude vantage point. A possibility of using polarization characteristics to enhance contrasts is demonstrated.

TABLE OF CONTENTS

	PAGE
I. INTRODUCTION	1
II. INSTRUMENTATION	4
III. MEASUREMENTS	16
A. Theory of Measurements	16
B. Mode of Operation	20
C. Data Obtained from the Measurements	22
1. Black Loam Soil	23
2. Desert Sand	23
3. Green Grass	40
4. Dry Grass	40
5. Dead Leaves	57
6. Broad leafed Plants	57
7. Crushed Limestone Gravel	57
8. Blacktop (Asphalt) Road Surface	82
9. Concrete	82
10. Canvas	82
IV. THEORY	107
V. RESULTS OF COMPUTATIONS	127
REFERENCES	135

LIST OF FIGURES

		PAGE
Fig. 1	Schematic representation of apparatus used in reflection measurements	5
Fig. 2	Schematic diagram of photoelectric reflectometer	5
Fig. 3	Relative transmission, as a function of wavelength, of filters used in these reflection measurements	7
Fig. 4	Schematic diagram of the electronic components of the reflectometer	9
Fig. 5 (a)	A. C. Amplifier for Photomultiplier Detector	11
(b)	Rectifier	12
Fig. 6	Instrument calibration curves which have been applicable at various stages of the measurements	13
Fig. 7	Infrared (1.05μ) Detector and AC Amplifier Circuit	15
Table I	Summary of values of the parameters for which reflectance and polarization measurements were made on each of ten selected surfaces	22
Fig. 8	Directional reflectance of black loam soil (Principal plane, $\theta_o = 78.5^\circ$)	24
Fig. 9	Degree of polarization of radiation reflected from black loam soil (principal plane, $\theta_o = 78.5^\circ$)	25
Fig. 10	Directional reflectance of black loam soil (principal plane, $\theta_o = 53.1^\circ$)	26
Fig. 11	Degree of polarization of radiation reflected from black loam soil (principal plane, $\theta_o = 53.1^\circ$)	27
Fig. 12	Directional reflectance of black loam soil (results independent of azimuth, $\theta_o = 0^\circ$)	

LIST OF FIGURES

		PAGE
Fig. 13	Degree of polarization of radiation reflected from black loam soil (results independent of azimuth, $\theta_o = 0^\circ$)	29
Fig. 14	Hemispheric map of the directional reflectance of black loam soil ($\theta_o = 53.1^\circ$, $\lambda = 6340\text{\AA}$)	30
Fig. 15	Hemispheric map of the degree of polarization of radiation reflected from black loam soil ($\theta_o = 53.1^\circ$, $\lambda = 6430\text{\AA}$)	31
Fig. 16	Directional reflectance of desert sand (principal plane, $\theta_o = 78.5^\circ$)	32
Fig. 17	Degree of polarization of radiation reflected from desert sand (principal plane, $\theta_o = 78.5^\circ$)	33
Fig. 18	Directional reflectance of desert sand (principal plane, $\theta_o = 53.1^\circ$)	34
Fig. 19	Degree of polarization of radiation reflected from desert sand (principal plane, $\theta_o = 53.1^\circ$)	35
Fig. 20	Directional reflectance of desert sand (results independent of azimuth, $\theta_o = 0^\circ$)	36
Fig. 21	Degree of polarization of radiation reflected from desert sand (results independent of azimuth, $\theta_o = 0^\circ$)	37
Fig. 22	Hemispheric map of the directional reflectance of desert sand ($\theta_o = 53.1^\circ$, $\lambda = 6430\text{\AA}$)	38
Fig. 23	Hemispheric map of the degree of polarization of radiation reflected from desert sand ($\theta_o = 53.1^\circ$, $\lambda = 6430\text{\AA}$)	39
Fig. 24	Directional reflectance of clipped green grass (principal plane, $\theta_o = 78.5^\circ$)	41

LIST OF FIGURES

	PAGE
Fig. 25 Degree of polarization of radiation reflected from clipped green grass (principal plane, $\theta_o = 78.5^\circ$)	42
Fig. 26 Directional reflectance of clipped green grass (principal plane, $\theta_o = 53.1^\circ$)	43
Fig. 27 Degree of polarization of radiation reflected from clipped green grass (principal plane, $\theta_o = 53.1^\circ$)	44
Fig. 28 Directional reflectance of clipped green grass (results independent of azimuth, $\theta_o = 0^\circ$)	45
Fig. 29 Degree of polarization of radiation reflected from clipped green grass (results independent of azimuth, $\theta_o = 0^\circ$)	46
Fig. 30 Hemispheric map of the directional reflectance of clipped green grass ($\theta_o = 53.1^\circ$, $\lambda = 6430\text{\AA}$)	47
Fig. 31 Hemispheric map of the degree of polarization of radiation reflected from clipped green grass ($\theta_o = 53.1^\circ$, $\lambda = 6430\text{\AA}$)	48
Fig. 32 Directional reflectance of dry grass (principal plane, $\theta_o = 78.5^\circ$)	49
Fig. 33 Degree of polarization of radiation reflected from dry grass (principal plane, $\theta_o = 78.5^\circ$)	50
Fig. 34 Directional reflectance of dry grass (principal plane, $\theta_o = 53.1^\circ$)	51
Fig. 35 Degree of polarization of radiation reflected from dry grass (principal plane, $\theta_o = 53.1^\circ$)	52
Fig. 36 Directional reflectance of dry grass (results independent of azimuth, $\theta_o = 0^\circ$)	53

LIST OF FIGURES

		PAGE
Fig. 37	Degree of polarization of radiation reflected from dry grass (results independent of azimuth, $\theta_o = 0^\circ$)	54
Fig. 38	Hemispheric map of the directional reflectance of dry grass ($\theta_o = 53.1^\circ$, $\lambda = 6430\text{\AA}$)	55
Fig. 39	Hemispheric map of the degree of polarization of radiation reflected from dry grass ($\theta_o = 53.1^\circ$, $\lambda = 6430\text{\AA}$)	56
Fig. 40	Directional reflectance of dead leaves (principal plane, $\theta_o = 78.5^\circ$)	58
Fig. 41	Degree of polarization of radiation reflected from dead leaves (principal plane, $\theta_o = 78.5^\circ$)	59
Fig. 42	Directional reflectance of dead leaves (principal plane, $\theta_o = 53.1^\circ$)	60
Fig. 43	Degree of polarization of radiation reflected from dead leaves (principal plane, $\theta_o = 53.1^\circ$)	61
Fig. 44	Directional reflectance of dead leaves (results independent of azimuth, $\theta_o = 0^\circ$)	62
Fig. 45	Degree of polarization of radiation reflected from dead leaves (results independent of azimuth, $\theta_o = 0^\circ$)	63
Fig. 46	Hemispheric map of the directional reflectance of dead leaves ($\theta_o = 53.1^\circ$, $\lambda = 6430\text{\AA}$)	64
Fig. 47	Hemispheric map of the degree of polarization of radiation reflected from dead leaves ($\theta_o = 53.1^\circ$, $\lambda = 6430\text{\AA}$)	65
Fig. 48	Directional reflectance of broad-leaved plants (principal plane, $\theta_o = 78.5^\circ$)	66

LIST OF FIGURES

		PAGE
Fig. 49	Degree of polarization of radiation reflected from broad-leaved plants (principal plane, $\theta_o = 78.5^\circ$)	67
Fig. 50	Directional reflectance of broad-leaved plants (principal plane, $\theta_o = 53.1^\circ$)	68
Fig. 51	Degree of polarization of radiation reflected from broad-leaved plants (principal plane, $\theta_o = 53.1^\circ$)	69
Fig. 52	Directional reflectance of broad-leaved plants (results independent of azimuth, $\theta_o = 0^\circ$)	70
Fig. 53	Degree of polarization of radiation reflected from broad-leaved plants (results independent of azimuth, $\theta_o = 0^\circ$)	71
Fig. 54	Hemispheric map of the directional reflectance of broad-leaved plants ($\theta_o = 53.1^\circ$, $\lambda = 6430\text{\AA}$)	72
Fig. 55	Hemispheric map of the degree of polarization of radiation reflected from broad-leaved plants ($\theta_o = 53.1^\circ$, $\lambda = 6430\text{\AA}$)	73
Fig. 56	Directional reflectance of crushed limestone (principal plane, $\theta_o = 78.5^\circ$)	74
Fig. 57	Degree of polarization of radiation reflected from crushed limestone (principal plane, $\theta_o = 78.5^\circ$)	75
Fig. 58	Directional reflectance of crushed limestone (principal plane, $\theta_o = 53.1^\circ$)	76
Fig. 59	Degree of polarization of radiation reflected from crushed limestone (principal plane, $\theta_o = 53.1^\circ$)	77

LIST OF FIGURES

		PAGE
Fig. 60	Directional reflectance of crushed limestone (results independent of azimuth, $\theta_o = 0^\circ$)	78
Fig. 61	Degree of polarization of radiation reflected from crushed limestone (results independent of azimuth, $\theta_o = 0^\circ$)	79
Fig. 62	Hemispheric map of the directional reflectance of crushed limestone gravel ($\theta_o = 53.1^\circ$, $\lambda = 6430\text{\AA}$)	80
Fig. 63	Hemispheric map of the degree of polarization of radiation reflected from crushed limestone gravel ($\theta_o = 53.1^\circ$, $\lambda = 6430\text{\AA}$)	81
Fig. 64	Directional reflectance of weathered blacktop (principal plane, $\theta_o = 78.5^\circ$)	83
Fig. 65	Degree of polarization of radiation reflected from weathered blacktop (principal plane, $\theta_o = 78.5^\circ$)	84
Fig. 66	Directional reflectance of weathered blacktop (principal plane, $\theta_o = 53.1^\circ$)	85
Fig. 67	Degree of polarization of radiation reflected from weathered blacktop (principal plane, $\theta_o = 53.1^\circ$)	86
Fig. 68	Directional reflectance of weathered blacktop (results independent of azimuth, $\theta_o = 0^\circ$)	87
Fig. 69	Degree of polarization of radiation reflected from weathered blacktop (results independent of azimuth, $\theta_o = 0^\circ$)	88
Fig. 70	Hemispheric map of the directional reflectance of weathered blacktop ($\theta_o = 53.1^\circ$, $\lambda = 6430\text{\AA}$)	89
Fig. 71	Hemispheric map of the degree of polarization of radiation reflected from weathered blacktop ($\theta_o = 53.1^\circ$, $\lambda = 6430\text{\AA}$)	90
Fig. 72	Directional reflectance of weathered concrete (principal plane, $\theta_o = 78.5^\circ$)	91

LIST OF FIGURES

		PAGE
Fig. 73	Degree of polarization of radiation reflected from weathered concrete (principal plane, $\theta_o = 78.5^\circ$)	92
Fig. 74	Directional reflectance of weathered concrete (principal plane, $\theta_o = 53.1^\circ$)	93
Fig. 75	Degree of polarization of radiation reflected from weathered concrete (principal plane, $\theta_o = 53.1^\circ$)	94
Fig. 76	Directional reflectance of weathered concrete (results independent of azimuth, $\theta_o = 0^\circ$)	95
Fig. 77	Degree of polarization of radiation reflected from weathered concrete (results independent of azimuth, $\theta_o = 0^\circ$)	96
Fig. 78	Hemispheric map of the directional reflectance of weathered concrete ($\theta_o = 53.1^\circ$, $\lambda = 6430\text{\AA}$)	97
Fig. 79	Hemispheric map of the degree of polarization of radiation reflected from weathered concrete ($\theta_o = 53.1^\circ$, $\lambda = 6430\text{\AA}$)	98
Fig. 80	Directional reflectance of canvas (principal plane, $\theta_o = 78.5^\circ$)	99
Fig. 81	Degree of polarization of radiation reflected from canvas (principal plane, $\theta_o = 78.5^\circ$)	100
Fig. 82	Directional reflectance of canvas (principal plane, $\theta_o = 53.1^\circ$)	101
Fig. 83	Degree of polarization of radiation reflected from canvas (principal plane, $\theta_o = 53.1^\circ$)	102
Fig. 84	Directional reflectance of canvas (results independent of azimuth, $\theta_o = 0^\circ$)	103
Fig. 85	Degree of polarization of radiation reflected from canvas (results independent of azimuth, $\theta_o = 0^\circ$)	104

LIST OF FIGURES

		PAGE
Fig. 86	Hemispheric map of the directional reflectance of canvas ($\theta_o = 53.1^\circ$, $\lambda = 6430\text{\AA}$)	105
Fig. 87	Hemispheric map of the degree of polarization of radiation reflected from canvas ($\theta_o = 53.1^\circ$, $\lambda = 6430\text{\AA}$)	106
Fig. 88	A Simplified Representation of the Contrast Determination Problem	110
Fig. 89	The relative contributions of the various intensity "components" in the principal plane, for Desert Soil, $\theta_o = 53.1^\circ$, and $\lambda = 6430\text{\AA}$	126
Fig. 90	The contrast attenuation coefficients as a function of Nadir angle in the principal plane, for $\theta_o = 53.1^\circ$, and $\lambda = 6430\text{\AA}$	128
Fig. 91	The contrast attenuation coefficient y_r as a function of azimuth, for Desert Soil, $\theta_o = 53.1^\circ$, and $\lambda = 6430\text{\AA}$	129
Fig. 92	The contrast attenuation coefficient y as a function of azimuth, for Desert Soil, $\theta_o = 53.1^\circ$, and $\lambda = 6430\text{\AA}$	130
Fig. 93	The contrast attenuation coefficient y_e as a function of azimuth, for Desert Soil, $\theta_o = 53.1^\circ$, and $\lambda = 6430\text{\AA}$	131
Fig. 94	The relative advantage, $\frac{y_e - y}{y} \times 100$, of using a polarizer, as a function of azimuth, for Desert Soil, $\theta_o = 53.1^\circ$, and $\lambda = 6430\text{\AA}$	132

I. Introduction

It is well known that the radiation which is directed to space from the upper limits of the atmosphere, as well as that which is proceeding upward inside the atmosphere, is composed partially of radiation which has been reflected from the planetary surface. One has only to look at television pictures taken from the TIROS or Nimbus meteorological satellites, at photographs obtained by Astronauts while in orbit around the Earth, at photographs taken on an aerial mapping or reconnaissance mission, or indeed at the sunlit scene presented at the window of a high altitude aircraft, to see just how important surface reflection is in determining the characteristics of the upwelling radiation. The intensity and polarization of the radiation observed in such circumstances are obviously functions of the angle at which the sunlight strikes the surface, the angle at which the surface is viewed, the wavelength of the radiation, the physical properties of the surface itself, and the transmission and scattering properties of the intervening atmosphere. The present research work has been an investigation of the effects introduced by these various parameters individually and of the characteristics of the total radiation which proceeds outward through the upper reaches of the atmosphere.

Measurements by different authors have already indicated some of the reflective properties of various types of surfaces. The results obtained by Miller (1955) show that a new snow surface may reflect more than 80 percent of the visible radiation which is incident on it. The extensive measurements by Krinov (1947) show total reflectance values of soil and rocks varying from

as little as 0.02 for black sandy loam to 0.35 - 0.75 for highly reflecting clay, limestone, and shale. Bauer and Dutton (1962) measured wavelength-integrated total hemispheric reflectance of farmlands and wooded hills of Wisconsin by radiometers mounted on aircraft, obtaining values of 0.10 to 0.20 in the absence of snow cover. Snow increased the average reflectance to 0.50 - 0.80 for otherwise similar conditions. Except for the effects of snow, the measurements showed little change of total reflectance with season, although it is to be expected that the wavelength distribution of the reflected radiation would vary with seasonal changes of vegetation.

The variation of reflectance with angle at which radiation is incident on the surface and angle at which the surface is viewed has received much less attention than has the total hemispherical reflectance. The effect of angle of incidence has been investigated, both theoretically and experimentally, more for water surfaces than for other types of surfaces. Of particular note here are the works of Cox and Munk (1955) in determining the effects of surface roughness on the reflectance properties of the sea, and of Anderson (1952) in measuring the energy reflected from an inland lake. The theoretically predicted strong dependence of reflectance of water on incident angle is borne out in the measurements, although roughness of the sea surface is influential in determining both the total reflectance and the intensity distribution of the reflected light. For natural land surfaces, the effect of incident angle is considered by Kondratev and Manolova (1955) in relation to the radiation balance of slopes. Ashburn and Weldon (1956) and Coulson (1956) showed a considerable dependence of the reflection properties

of semi-desert surfaces on solar zenith angle, and a number of investigators, Middleton and Mungall (1952), and Christie (1953), for example, have shown a strong functional dependence of snow reflection on angle of incidence.

Measurements of the directional reflectance properties of terrestrial surfaces, as evidenced by the angular intensity distribution of the reflected light, have been oriented mainly toward interpreting the reflectance properties of the Moon. Orlova (1956) has made reflectance measurements of a number of surfaces in the laboratory and classified the "indicatrices" into orthotropic, reflecting, rough, and mixed categories, depending on the number and position of reflection maxima. Additional measurements on very complex terrestrial materials, similarly directed toward the interpretation of photometric properties of the Moon, have been made by vanDiggelen (1959), Hapke and vanHorn (1963), and others. Most of these measurements have been confined to the principal plane. Krinov's (1947) measurements were made mainly in the direction of the nadir, but for a few cases the instrument was directed at a 45° nadir angle and 90° azimuth angle with respect to the azimuth of the sun.

Measurements on the polarizing properties of materials extend back to the pioneering work of Arago and to the relatively extensive set of measurements performed by Brewster (1865) on painted surfaces, paper, cloth, snow, and white powders of various kinds. Lyot and Dollfus (1949), by the use of a polarimeter invented by Lyot, determined the degree of polarization of light reflected by the Moon. The polarizing properties of a number of types of natural and artificially-produced materials have been measured by Dollfus

(1961, 1957) using the technique of Lyot. Dollfus applied his polarization results to interpreting the composition of the lunar and Martian surfaces and to a deduction of an upper limit for the density of the atmosphere of the Moon and in determining the total mass of the atmosphere of Mars.

Unfortunately none of these investigations has been adequate for present requirements in equipment development, more complete data on all of the different parameters being required. The general approach taken in this investigation was designed to provide results of maximum utility in the practical problem of object detection by an imaging device, be the device the human eye or a photographic or television camera. In particular, the possibilities of using the polarization characteristics of the radiation to enhance contrasts in the viewed field are of major interest. The investigation has encompassed measurements of the directional reflectance and degree of polarization of the reflected radiation for ten different types of surfaces, the instrumental requirements for making those measurements, the theory of radiative transfer by which the measurements can be quantitatively interpreted in the context of the problem, and the computational results obtained. Each of these aspects will be discussed below.

II. Instrumentation

The instrument which has been used for the measurements is shown schematically in Fig. 1. The material sample is contained in a 2 feet square sample tray S which is illuminated by a light source L from a zenith angle θ_0 .

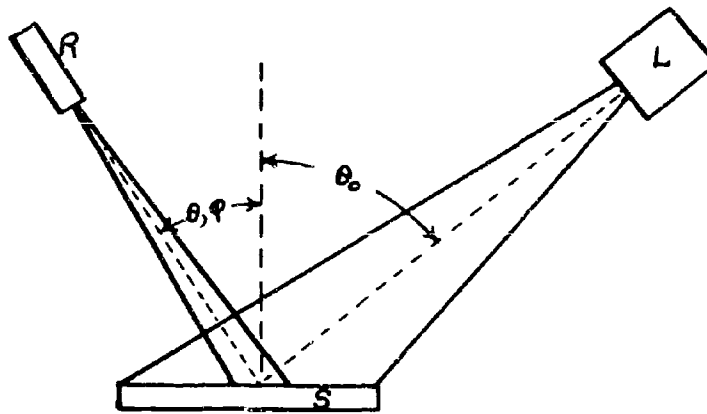


Fig. 1 - Schematic representation of apparatus used in reflection measurements

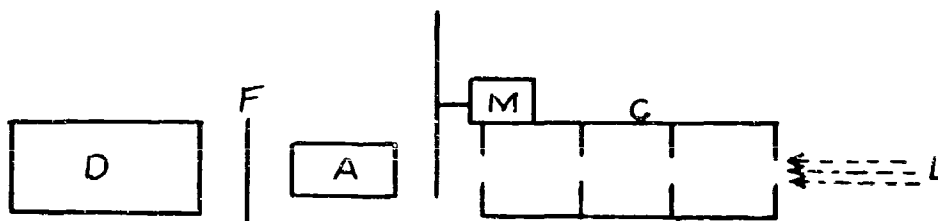
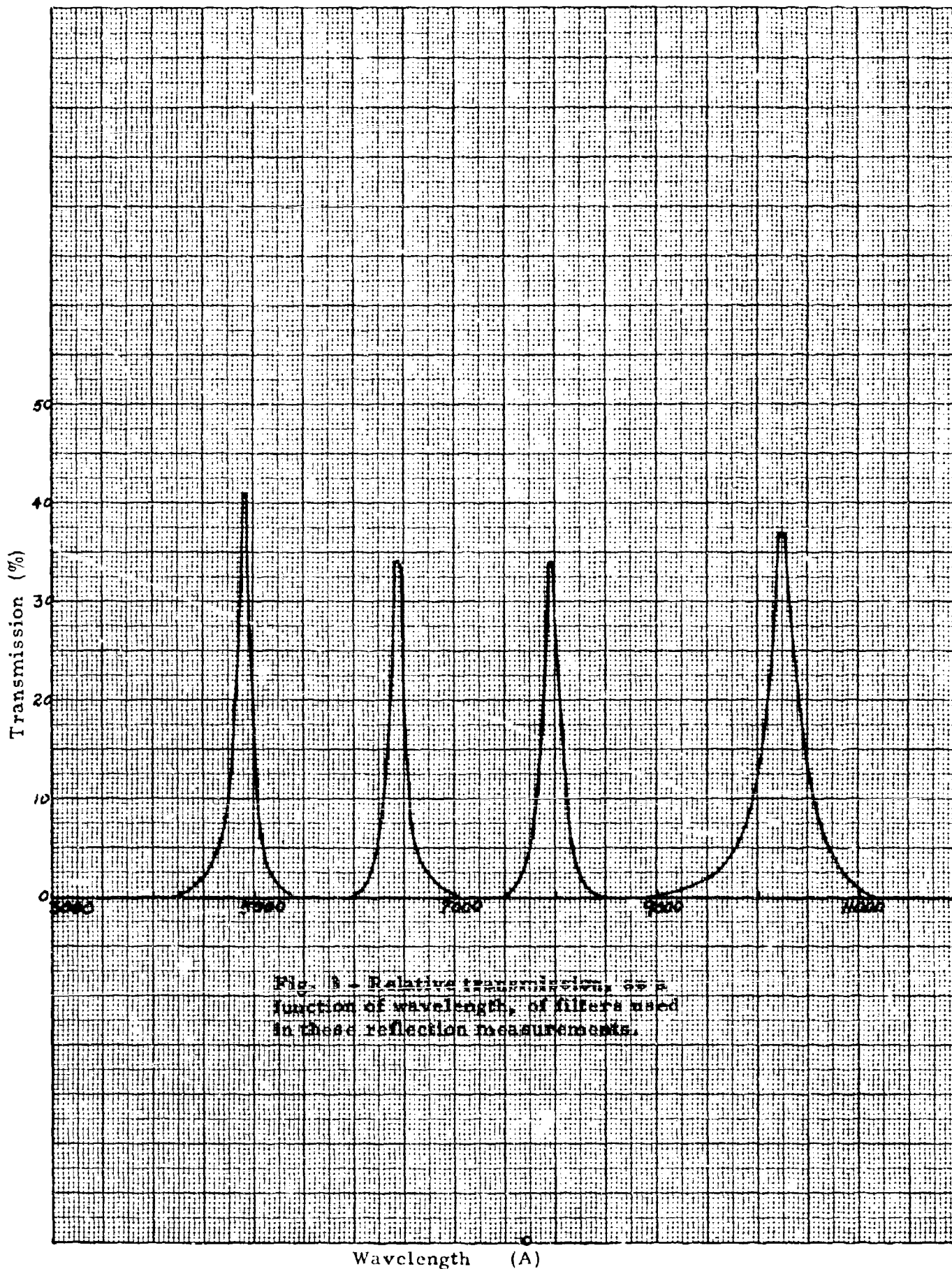


Fig. 2 - Schematic diagram of photoelectric reflectometer

The surface is viewed from a zenith angle θ and azimuth ϕ by the photo-electric reflectometer R.

The reflectometer itself is shown schematically in Fig. 2. The light L enters the collimator tube C, is chopped by a chopper rotated by motor M, and passes successively through a rotating analyzer A and optical filter F, and finally activates a radiation detector D. The detector for radiation of wavelengths $\lambda \leq 7960\text{\AA}$ has been a photomultiplier tube (RCA), and for $\lambda = 1.025\mu$ a silicon photodiode has been used. The response of the detector is amplified and recorded on a standard strip-chart recorder. The acceptance field for the instrument is limited to a 2.5° half-angle cone by the diaphragms within the collimator tube. In order to minimize possible polarization sources within the instrument, the optical components have been restricted to the bare essentials, no lenses or mirrors being in the optical train. The analyzer which has been used for most of the measurements is a sheet polarizer (Polaroid HN-22) which gives better than 99.9% polarization throughout the spectral range of $\lambda \leq 7960\text{\AA}$. A Glan-Thompson prism was used at $\lambda = 1.025\mu$.

The measurements have been made in four spectral regions defined by interference filters and centered at wavelengths 4920 \AA , 6430 \AA , 7960 \AA , and 1.025μ . Transmission curves for the filters are shown in Fig. 3. The first three of those particular wavelengths correspond, respectively, to normal optical thicknesses of 0.15, 0.05, and 0.02 for the Earth's molecular atmosphere. The wavelength of 1.025μ was chosen so as to minimize atmospheric effects, both of scattering by the atmospheric components and absorption by atmospheric



water vapor.

A schematic diagram of the components of the reflectometer, for the case in which the photomultiplier tube was used as the detector, is shown as Fig. 4. The basic configuration is a standard one for a photomultiplier tube. The most stringent requirement for the present application was that of obtaining the required sensitivity. A low reflectance of some of the surfaces combined with a narrow bandpass filter resulted in a very small energy flux incident on the detector. The problem was particularly severe at 7960\AA , for which case the S-20 type cathode surface has a low sensitivity. A tube with an S-1 response was not available in time for use on this short period contract.

These difficulties required a high-gain amplifier to be installed in the system, a fact which introduced a severe noise pickup problem. It was necessary to entirely repackage the amplifier in order to bring the noise down to a tolerable level. The repackaging task required a considerable expenditure of both time and effort and caused the measurement program to fall behind in the schedule which had been planned.

A concentrated effort was made to bring the measurements back to schedule, a goal which was only partially achieved. The net result of the whole instrumentation problem was to eliminate the possibility, within the time and funds available on the contract, of making measurements in the ultraviolet spectral region as had been anticipated.

The circuit diagram of the final electronic configuration used with the

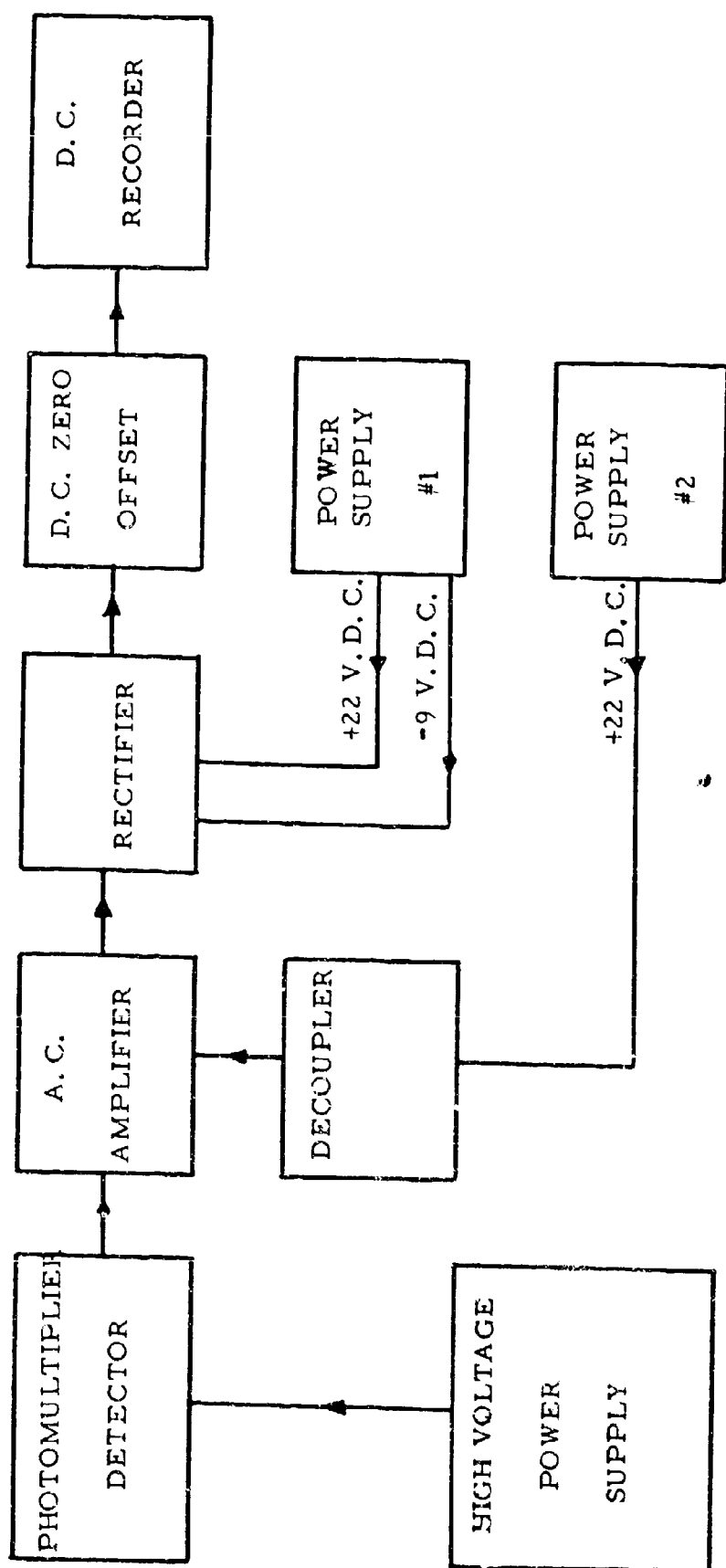


Fig. 4 - Schematic diagram of the electronic components of the reflectometer.

photomultiplier tube is included as Fig. 5. In making the measurements, a procedure was established by which an instrument calibration was performed, by means of a series of calibrated neutral density filters, after the instrument had stabilized at the beginning of each day's measurements. This helped to assure the validity of the measurements and it turned out to be very useful in final interpretation of the data. The system response was found to change at two different times in the measurement program. At the beginning of the measurements, the response was linear with radiation intensity throughout the full scale deflection but there was a constant scale offset correction which had to be applied. This calibration curve, which is plotted as Curve I in Fig. 6, was valid until September 15, at which time the major modification to the amplifier was made.

The amplifier modification introduced a nonlinearity into the instrument response, as shown by the calibration Curve II of Fig. 6. This nonlinearity was taken into account during the data reduction process by fitting the curve by a third degree polynomial and programming the computer to automatically correct each measurement value appropriately. This added only a negligible increase in the computer time required. Curve II was applicable for the period September 25 to October 25, inclusive.

At the start of measurements on October 26 it was found that a slight shift of the calibration for low light levels had occurred between the calibrations of October 25 and October 26, while the original curve was still valid at deflections greater than about fifty scale divisions. The new response, shown by Curve III

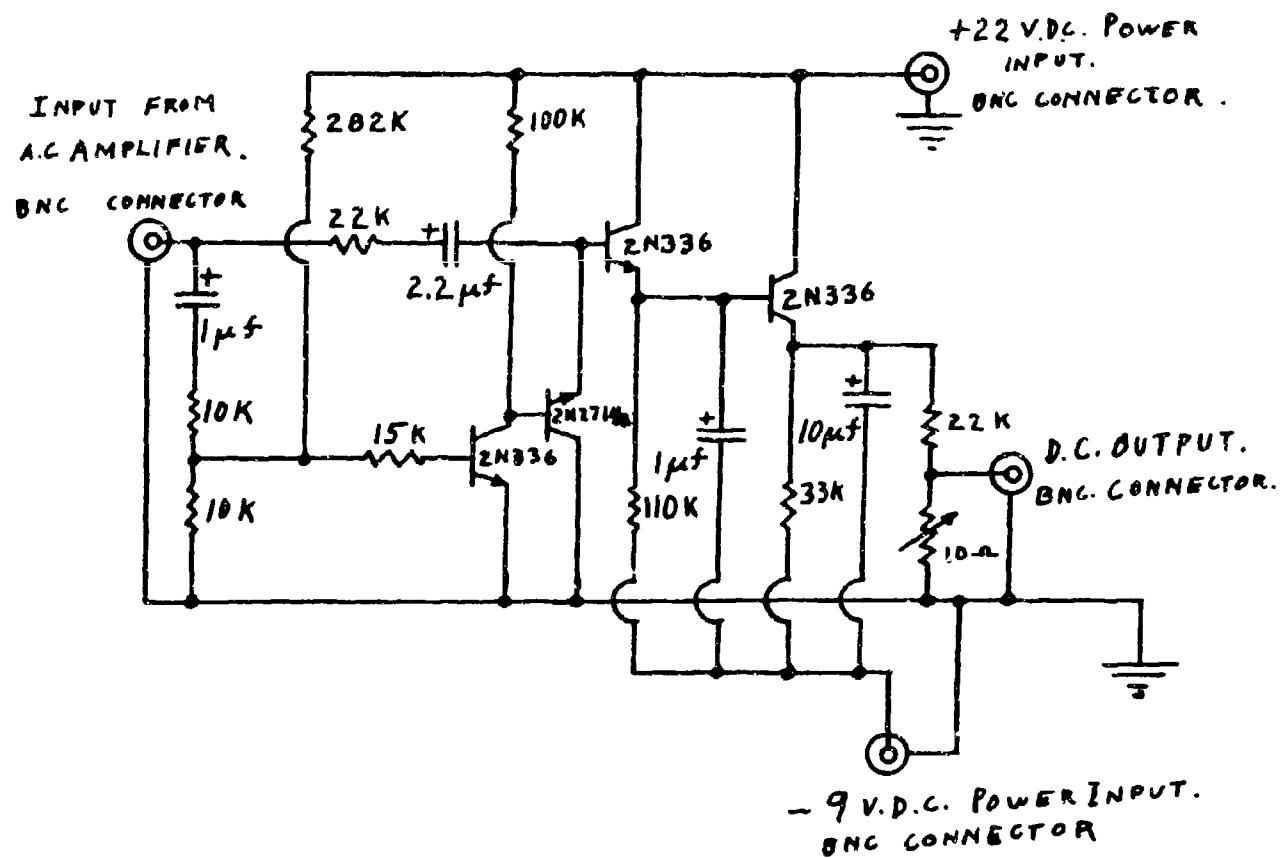


Fig. 5(b)
RECTIFIER.

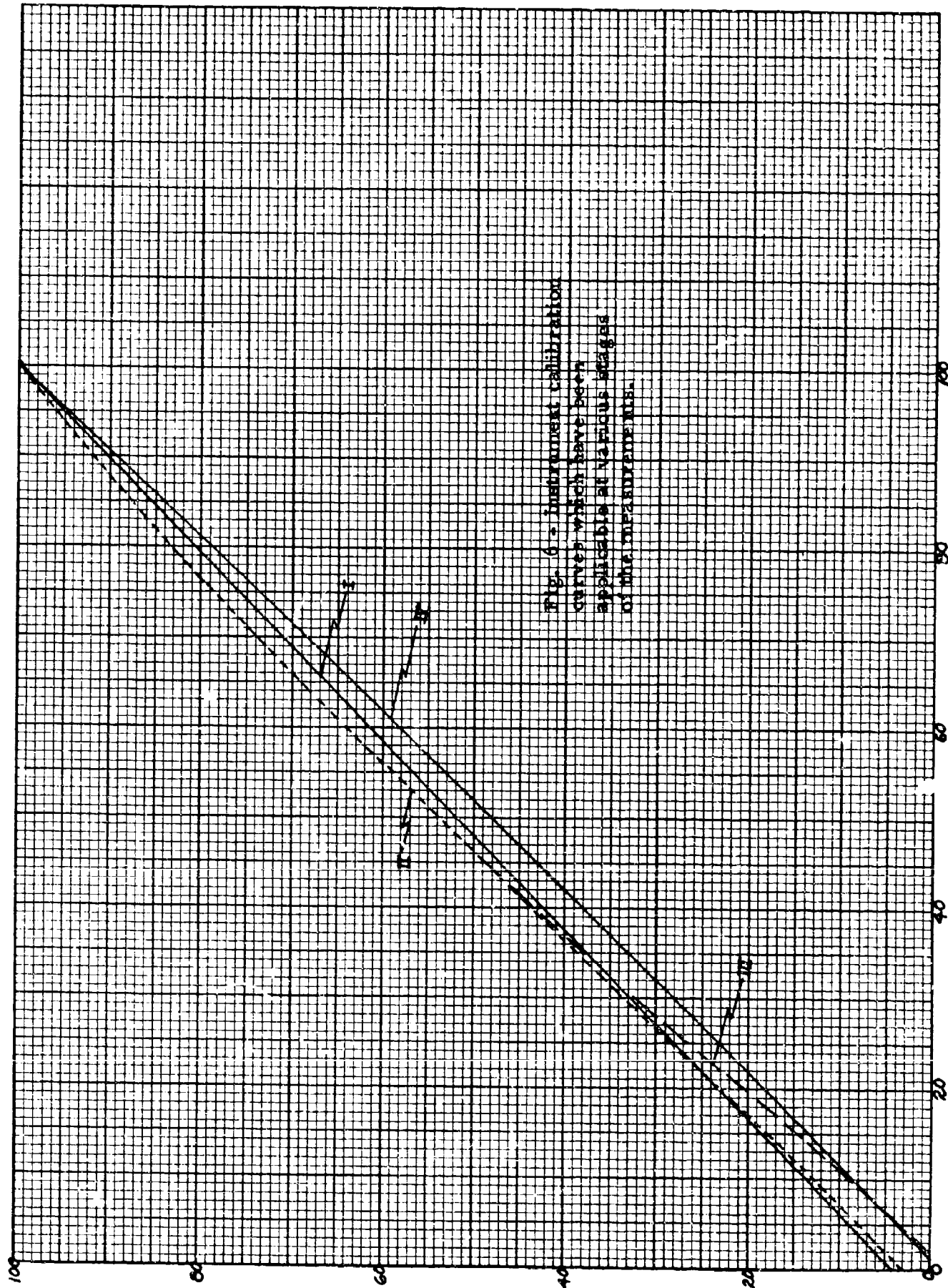


Fig. 6 - Instrument calibration curves which have been applicable at various stages of the measurements.

in Fig. 6, changed very little up until the end of the measurements with the photomultiplier, and it was fitted with another third degree polynomial for data reduction. The reason for the relatively sudden shift has still not been determined.

The final calibration curve of the equipment, Curve IV of Fig. 6, is that applicable for the silicon detector and its attendant electronics. A slight non-linearity was again taken account of by a polynomial approximation in the data reduction program.

In order to extend the spectral range of the measurements to beyond one micron, it was necessary to replace the photomultiplier with a silicon photodiode detector and to install a Glan-Thompson analyzer in place of the Polaroid disk. The photodiode was supplied by the Navy and the Glan-Thompson prism was available from another project.

Sensitivity problems again were encountered and were finally overcome by increasing the incident radiation by the use of two infrared heat lamps as the source. This had an undesirable effect of increasing the dimensions of the source itself, but it was the only alternative available within the scope of the project. Increasing the area of the source tends to smooth out the angular dependence in the measurements.

The electronic circuit diagram of the amplifier used with the silicon photodiode detector is shown as Fig. 7.

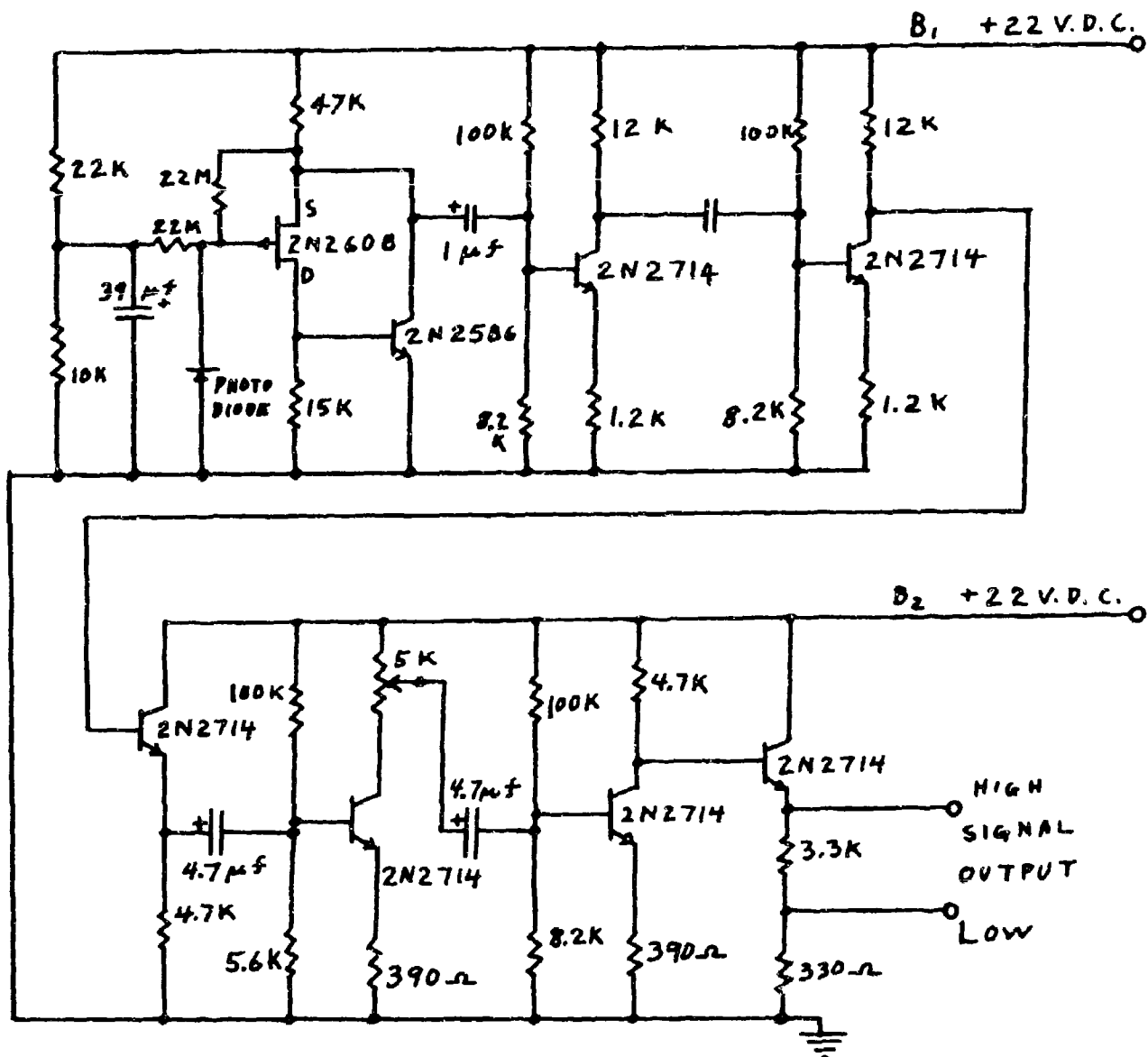


Fig. 7 - Infrared (1.025 μ)

Detector and AC Amplifier Circuit.

III. Measurements

A. Theory of measurements

A radiation field in an arbitrary state of polarization can be represented in terms of four quantities, which are usually called the Stokes parameters after the English physicist of the 19th century, Sir George Stokes. If we denote two orthogonal directions in the plane normal to the direction of propagation of the radiation by i and j , then the intensities I_i and I_j are, respectively, the squares of the amplitudes of the electric vector along the i and j directions. The total intensity of the radiation, which is the first of the Stokes parameters, is given by

$$I = I_i + I_j \quad (1)$$

The other three of the Stokes parameters are defined in terms of the orthogonal components as follows:

$$\begin{aligned} Q &= I_i - I_j \\ U &= 2(I_i I_j)^{1/2} \cos \delta \\ V &= 2(I_i I_j)^{1/2} \sin \delta \end{aligned} \quad (2)$$

δ is the phase angle between the vibrations in the i and j directions. If ψ is the angle between the direction i and the major axis of the ellipse described by the vibration of the electric vector of the radiation, then

$$U = Q \tan 2\psi. \quad (3)$$

The parameter V is expressed in terms of the major and minor axes of the ellipse, denoted by a and b respectively, by the relations

$$V = I \sin 2 \beta$$

$$\beta = \arctan \left(\frac{b}{a} \right) \quad (4)$$

The degree of polarization is

$$P = \frac{(Q^2 + U^2 + V^2)^{1/2}}{I} \quad (5)$$

In the present measurements it is assumed that the only type of polarization present is linear, in which case

$$V = 0 \quad (6)$$

Then the only quantities necessary to characterize this partially linearly polarized radiation are I_i , I_j , and ψ . In the reflectometer being used, the output from the detector is monitored continuously as the analyzer is rotated around the optical axis of the instrument. This means that the maximum signal is obtained when the plane of transmission of the analyzer is parallel to the direction i , in which case $\psi = 0$. The minimum is obtained after another 90° rotation of the analyzer, or at $\psi = \pi/2$. In both cases $U = 0$, and the intensity and degree of polarization of the measured radiation are given by

$$I = I_i + I_j = I_{\max} + I_{\min}$$

$$P = \frac{I_i - I_j}{I_i + I_j} = \frac{I_{\max} - I_{\min}}{I_{\max} + I_{\min}} \quad (7)$$

Directional reflectance of the surface is obtained in the following manner.

It is known that a surface composed of magnesium oxide represents, to a good approximation, a perfectly diffuse surface with a reflectance of 1.0 for visible light. Such a surface is used as a standard reflector. If F units of energy per

unit time and unit frequency interval are incident on a unit area of the standard surface, the intensity I_s of energy reflected into an incremental solid angle $d\omega$ is independent of direction and satisfies the relation

$$\int_{\Omega} I \mu d\omega = R_s F = F, \quad (8)$$

where $\mu = \cos \theta$, θ being the nadir angle at which the surface is viewed. R_s represents the total reflectance of the standard surface, which is taken as unity for the magnesium oxide, and the integration is taken over the entire hemisphere. A directional reflection coefficient ρ_s also has significance, and can be defined by the relation

$$\rho_s = \frac{I_s}{F} \quad (9)$$

Obviously ρ_s is a constant for a perfect standard (Lambert) surface. By Eq. (8) and Eq. (9), integration over a hemisphere yields, for the standard surface,

$$\int_{\Omega} \rho_s \mu d\omega = R_s = 1 \quad (10)$$

and

$$\rho_s = \frac{1}{\pi} \quad (11)$$

Let $I(\mu, \varphi)$ denote the intensity of radiation reflected from a sample surface into a direction given by the nadir angle θ and azimuth φ for the condition in which the sample is likewise illuminated by F units of energy per unit time and unit frequency interval. We can now define a direction-dependent reflection coefficient $\rho(\mu, \varphi)$ for the surface by the relation

$$I(\mu, \varphi) = \rho(\mu, \varphi) F. \quad (12)$$

These quantities must satisfy the relations

$$\int_{\Omega} I(\mu, \varphi) \mu d\omega = R F \quad (13)$$

$$\int_{\Omega} \rho(\mu, \varphi) \mu d\omega = R, \quad (14)$$

where R is the ratio of the total reflected energy to the total incident energy.

The procedure followed for the actual measurements is to illuminate the magnesium oxide standard surface from a direction given by the zenith angle $\theta_0 \equiv \arccos \mu_0$ and azimuth angle $\varphi_0 = 0$ and set the instrument to view the standard surface from a direction (θ, φ) . If the standard were a perfect Lambert surface, the measured intensity would be independent of θ and φ . However, in order to assure uniformity in the measurements, the standard surface is always viewed from the direction of the surface-normal, in which case $\theta = 0$ and φ is indeterminate. Thus, an instrument response D_s for the standard surface is obtained. The intensity I_s of the reflected light is then

$$I_s = \Delta_s D_s, \quad (15)$$

where Δ_s is the instrument transfer function at intensity I_s .

The standard surface is then replaced by the sample for which the reflection characteristics are desired. The sample is viewed from any desired direction, given by (θ, φ) , and a second instrument response $D(\theta, \varphi)$ is obtained. The intensity $I(\theta, \varphi)$ is

$$I(\theta, \varphi) = \Delta D(\theta, \varphi) \quad (16)$$

where Δ is the instrument transfer function at this new intensity.

The instrument transfer function may or may not be independent of intensity,

the only requirement being that it be a known function. The most convenient situation is that Δ is a constant over the range of intensities of interest, or $\Delta_s = \Delta$. This ideal situation existed during the first part of the present measurements, as was seen by the linear behavior of calibration Curve I of Fig. 6 above. Unfortunately the instrument response has been non-linear since the modifications introduced after September 15. A method of introducing the corrections by computer was devised, however, and the non-linear behavior has caused no significant problem in the measurements.

On taking the ratio of Eq. (16) to Eq. (15) and introducing Eq. (9) and Eq. (12) we obtain

$$\frac{I(\theta, \varphi)}{I_s(0, -)} = \frac{D(\theta, \varphi)}{D_s(0, -)} = \frac{\rho(\theta, \varphi)}{\rho_s(0, -)} \quad (17)$$

The assumption has been made that the incident flux F is constant.

Finally, by introducing the known value of ρ_s given by Eq. (11), we obtain the final expression for the directional reflectance of the sample surface in the (θ, φ) direction as

$$\rho(\theta, \varphi) = \frac{1}{\pi} \frac{D(\theta, \varphi)}{D_s(0, -)} \quad , \quad (18)$$

B. Mode of Operation

The mode of operation in the measurements was typically as follows:

The sample was placed in the sample tray in such a manner that the surface was level with the sides of the tray. For soil and sand samples the surface was carefully levelled off by means of a straight edge. Every effort was made to avoid directional effects being introduced during the levelling process. For plant materials the effective top of the plants, as judged by

eye, was made to coincide with the level of the sides of the sample tray. The surfaces of solid materials such as concrete and blacktop were easily adjusted to the correct height, and the sample of canvas was tightly stretched over the top of the sample tray.

Once the sample was properly prepared, it was placed on the stage of the reflectometer mount. The stage is constructed so that it rotates in azimuth as the reflectometer itself is rotated. The light source, a tungsten filament bulb, was then positioned for a given angle of incidence. In these measurements three angles of incidence were used, namely, 0° , 53.1° , and 78.5° .

The first data taken at the start of a day's operation was an instrument calibration curve. This was done by placing calibrated neutral filters of varying density serially in front of the entrance aperture of the instrument and recording the instrument response on the strip chart recorder. After calibration, the reflectometer was set to view the surface in the direction normal to the surface ($\theta = 0^{\circ}$), and the standard smoked magnesium oxide plate was superimposed a few millimeters above the sample. After a record of the instrument output was obtained for the standard, the plate was removed and a similar measurement of the reflectance of the surface at $\theta = 0^{\circ}$ was made. Thus the sample surface itself as viewed from $\theta = 0^{\circ}$ became a secondary standard of known reflectance, and the later measurements for this particular sample, wavelength, and source position were normalized to the secondary standard value of reflectance in the data reduction process.

After the above steps had been completed, the series of measurements

at the azimuth $\varphi=180^\circ$ was made varying the angle of view from $\theta = 0^\circ$ to $\theta = 70^\circ$ in ten degree steps and from $\theta = 70^\circ$ to $\theta = 80^\circ$ in five degree steps. When this was accomplished the reflectometer was returned to $\theta = 0^\circ$ and the measurement on the secondary standard (sample viewed at $\theta = 0^\circ$) was repeated. Thus a record was obtained from the secondary standard once every ten minutes or so, by which the drift of the instrument response or light source output could be compensated for in the data reduction process. The reflectometer was then rotated to a new azimuth and another series of measurements from $\theta = 0^\circ$ to $\theta = 80^\circ$ was begun.

Finally, at the end of the series of sweeps at various azimuths another set of measurements was made on the magnesium oxide standard and secondary standard, after which either the wavelength, source position, or sample was changed and the process was begun once more under the changed conditions.

C. Data obtained from the measurements

Measurements of the directional reflectance and degree of polarization of the reflected radiation were made on each of ten different types of surfaces. The values of the various parameters for which data were obtained are listed as Table I.

Table I: Summary of values of the parameters for which reflectance and polarization measurements were made on each of ten selected surfaces

$\lambda (\text{\AA})$	$\theta_0 (^\circ)$	$\varphi (^\circ)$
4920	0, 53.1, 78.5	0, 180
6430	0, 53.1, 78.5	0, 45, 90, 135, 180
7960	0, 53.1, 78.5	0, 180
10250	0, 53.1, 78.5	0, 180

The data for the principal plane are presented in the form of plots of directional reflectance versus nadir angle of observation and degree of polarization versus nadir angle of observation. These plots make a total of 240 separate curves for the principal plane alone. In addition, two hemispheric maps, one for reflectance and one for degree of polarization, are given for each of the ten surfaces, thereby making a total of twenty such hemispheric maps. Thus eight different figures are given for each surface, making a total of eighty different figures for the measured results. They are separated according to surface and presented below.

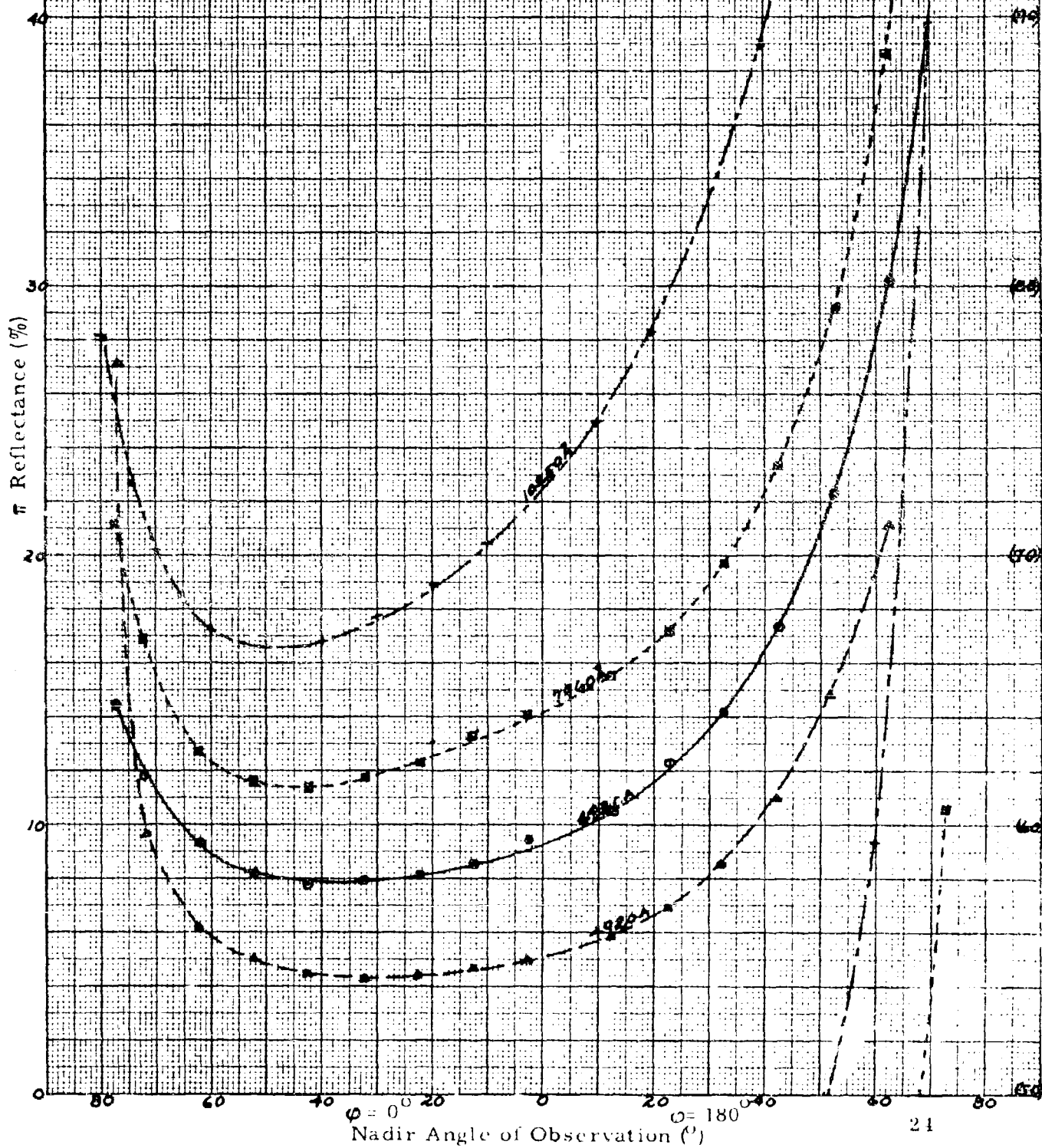
1. Black loam soil

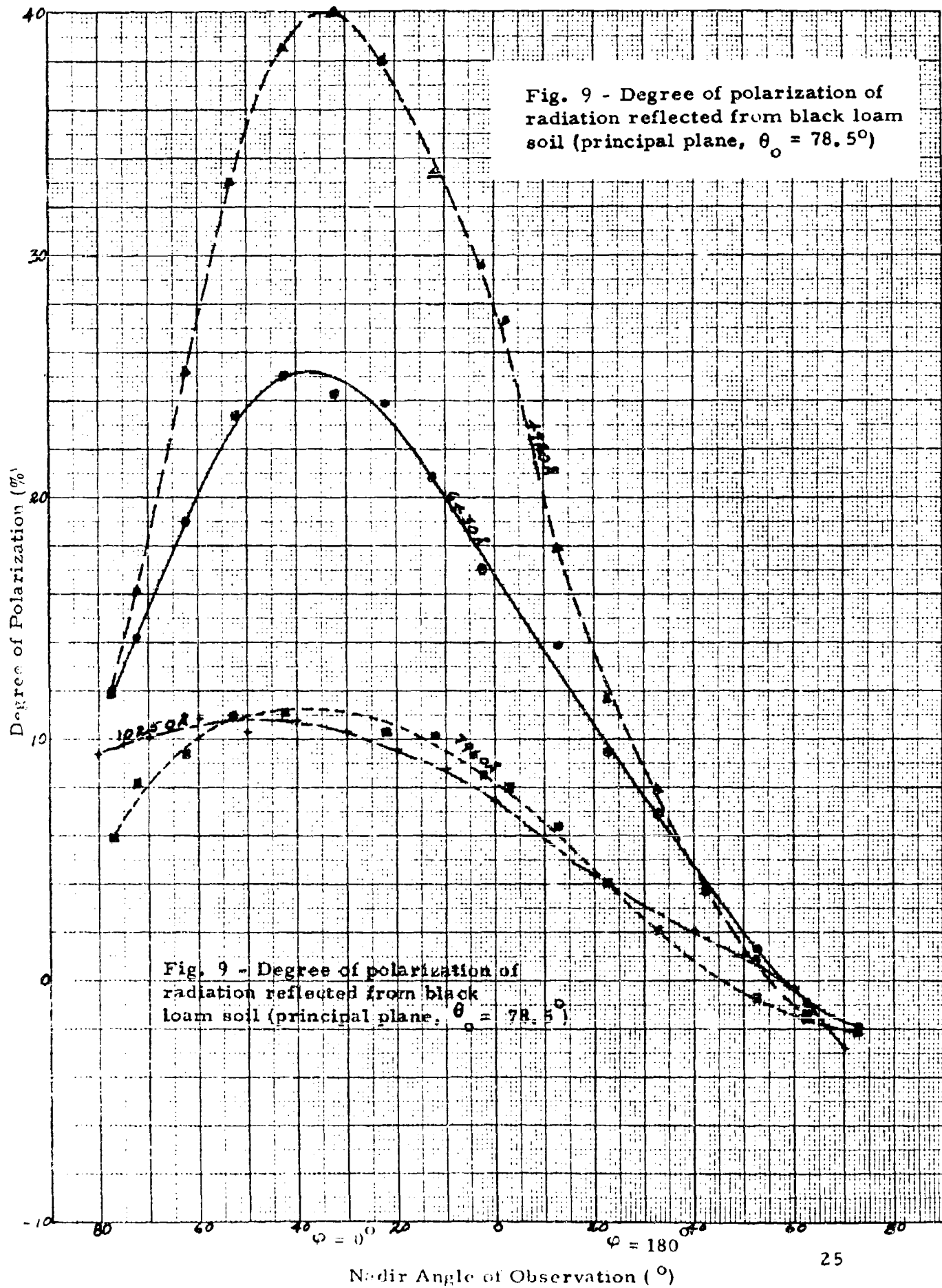
The sample of black loam soil was obtained in Southwestern Iowa near the town of Mt. Ayr. It is typical of the soil covering large areas of the Midwest, particularly that of the corn belt. The results of the measurements are shown by Figures 8 through 13 for the principal plane and by Figures 14 and 15 for the hemisphere at $\lambda = 6430\text{\AA}$. Since the results are symmetrical with respect to the principal plane only one half of the hemisphere is shown. The other half is simply a mirror image of the one represented.

2. Desert Sand

The sample of desert sand was obtained from the Mojave Desert about eleven miles northeast of Mojave. It is interesting that where the sample was collected there was no appreciable change of darkness of the material with depth below the surface. This is not the case for a sample collected previously from a spot about one mile northeast of Mojave. At that time it was noticed that the surface appeared to be bleached out, the material a few millimeters

Fig. 8 - Directional reflectance
of black loam soil (principal
plane, $\theta_0 = 78.5^\circ$)





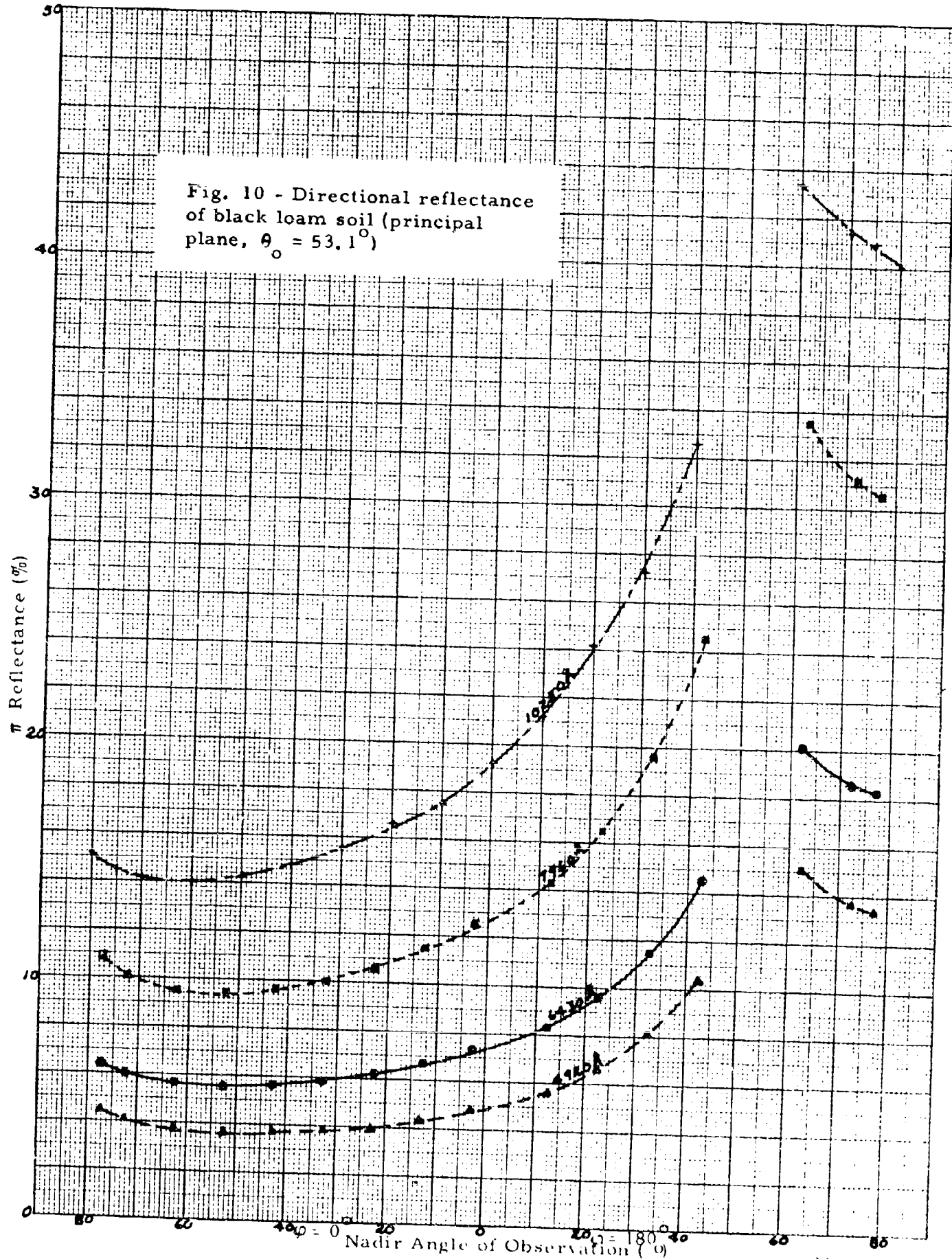


Fig. 11 - Degree of polarization of radiation reflected from black loam soil (principal plane, $\theta_o = 53.1^\circ$)

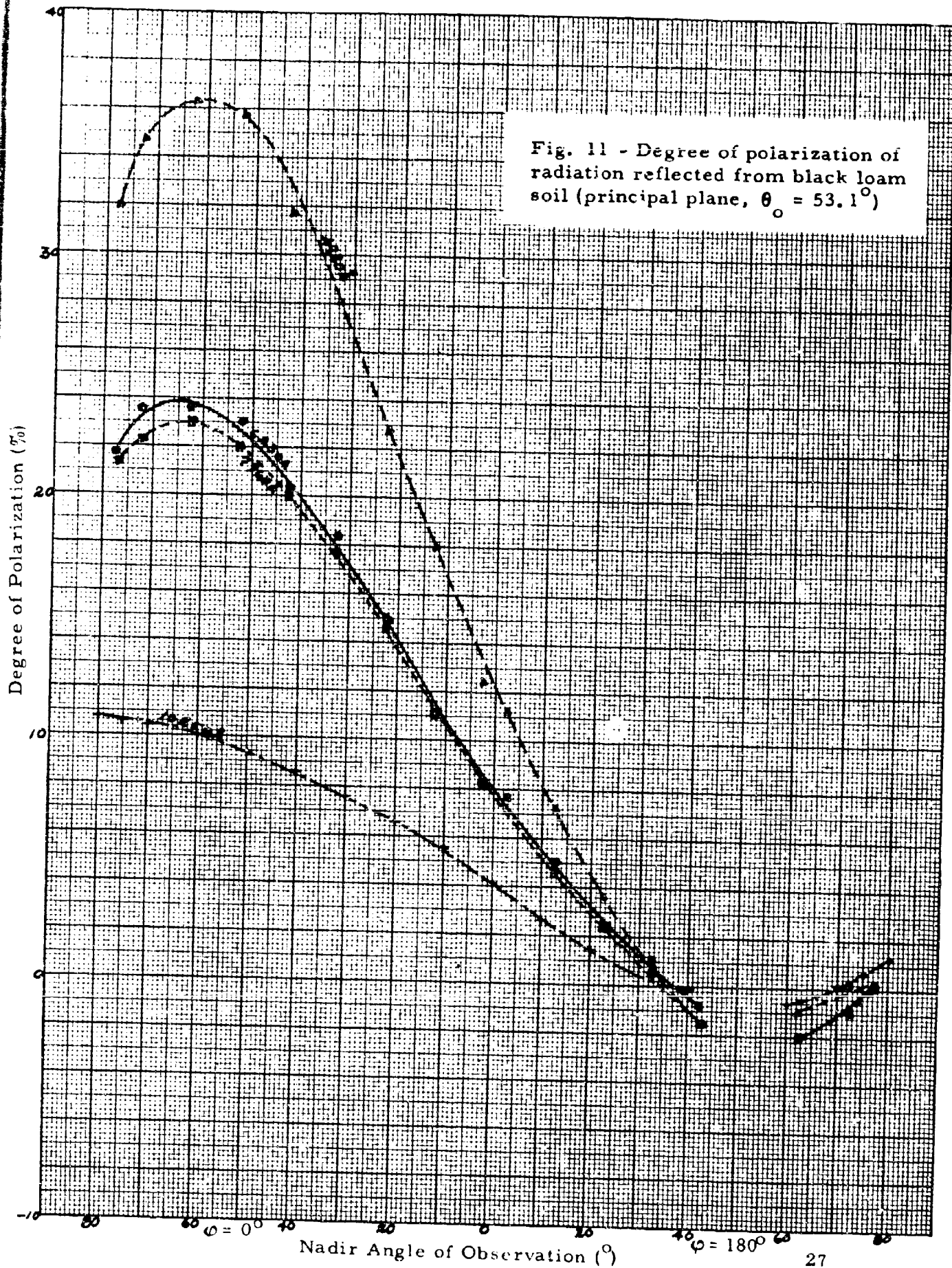


Fig. 12 - Directional reflectance
of black loam soil. (results
independent of azimuth, $\theta_o = 0^\circ$)

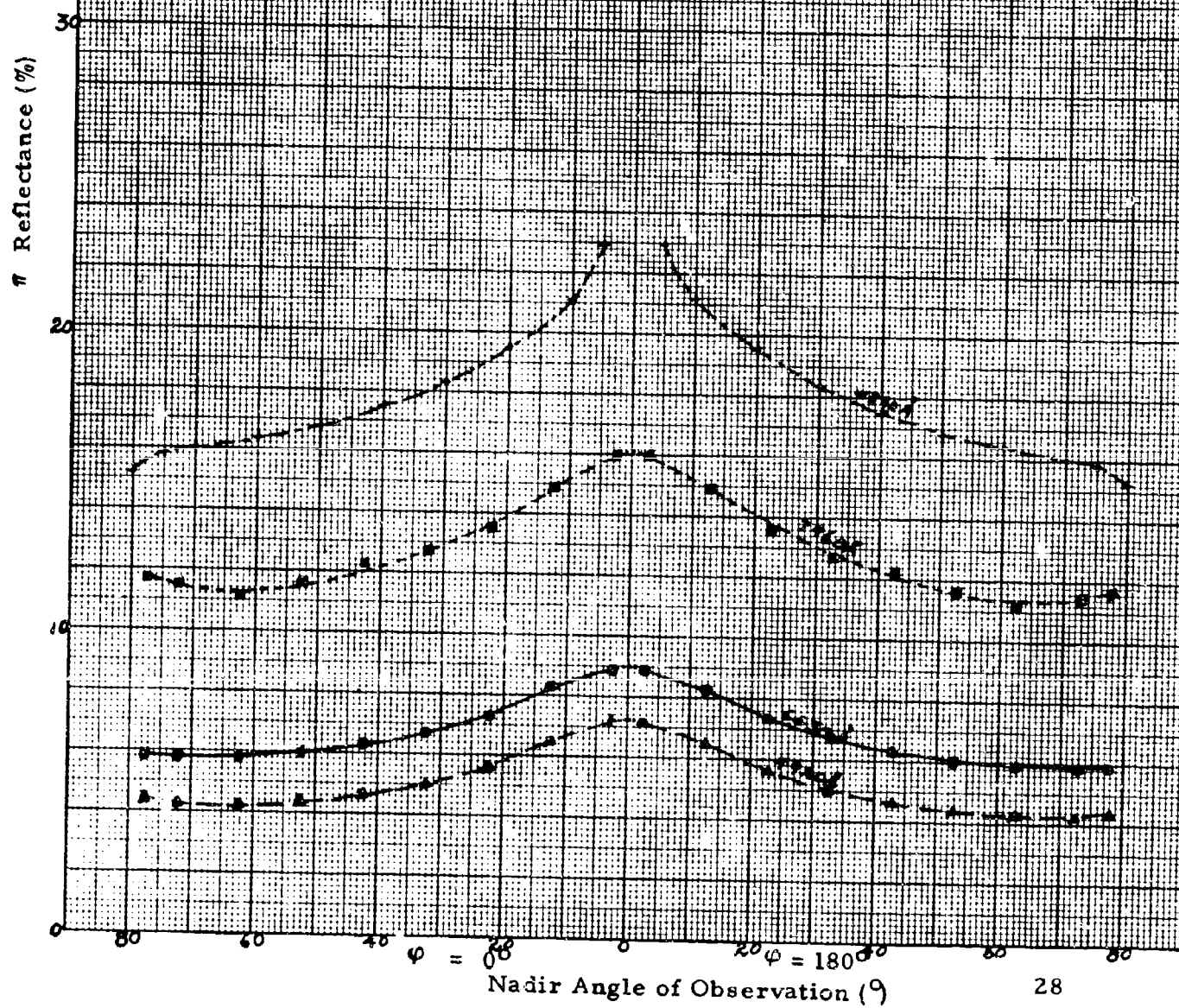
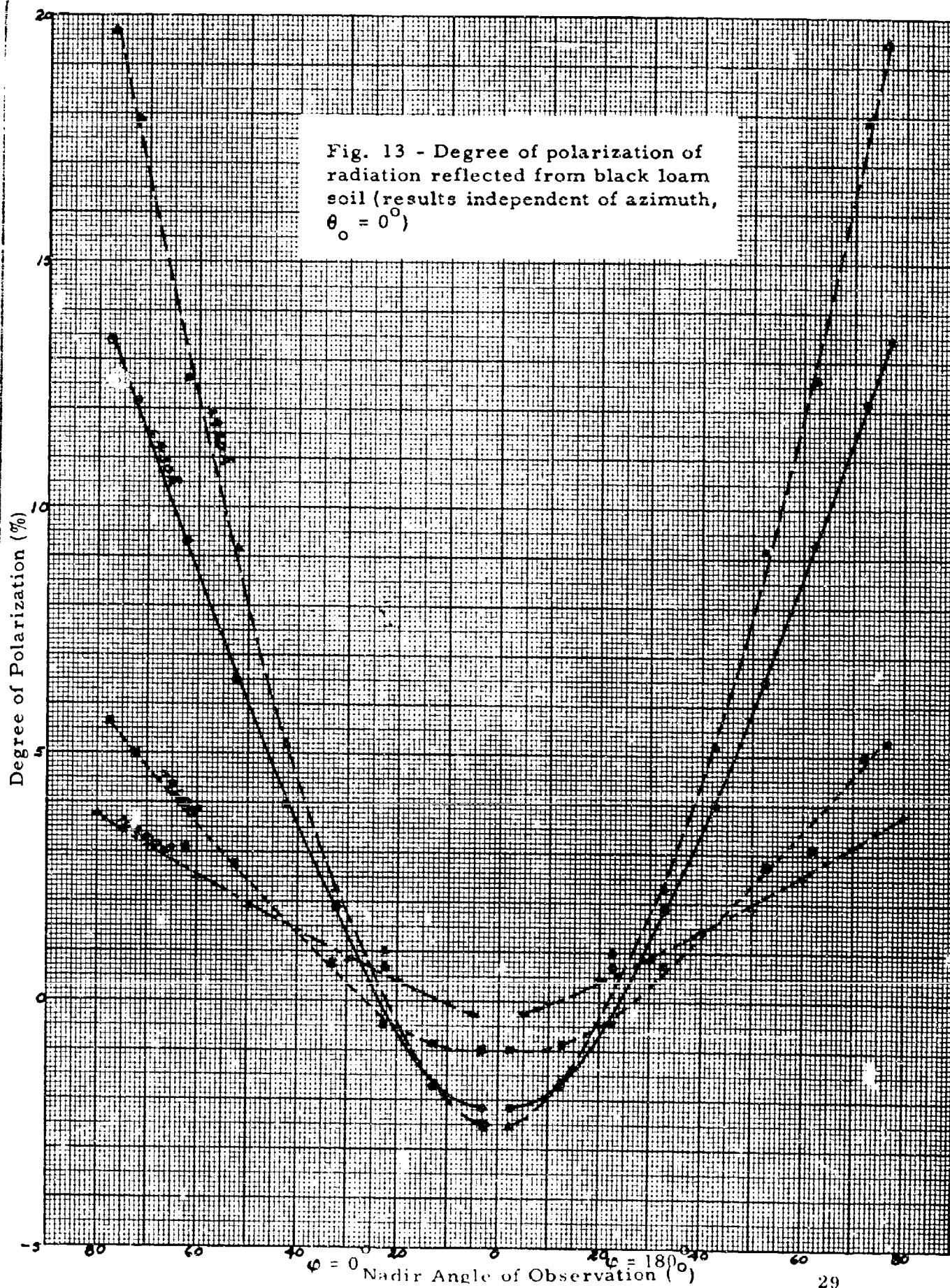


Fig. 13 - Degree of polarization of radiation reflected from black loam soil (results independent of azimuth, $\theta_0 = 0^\circ$)



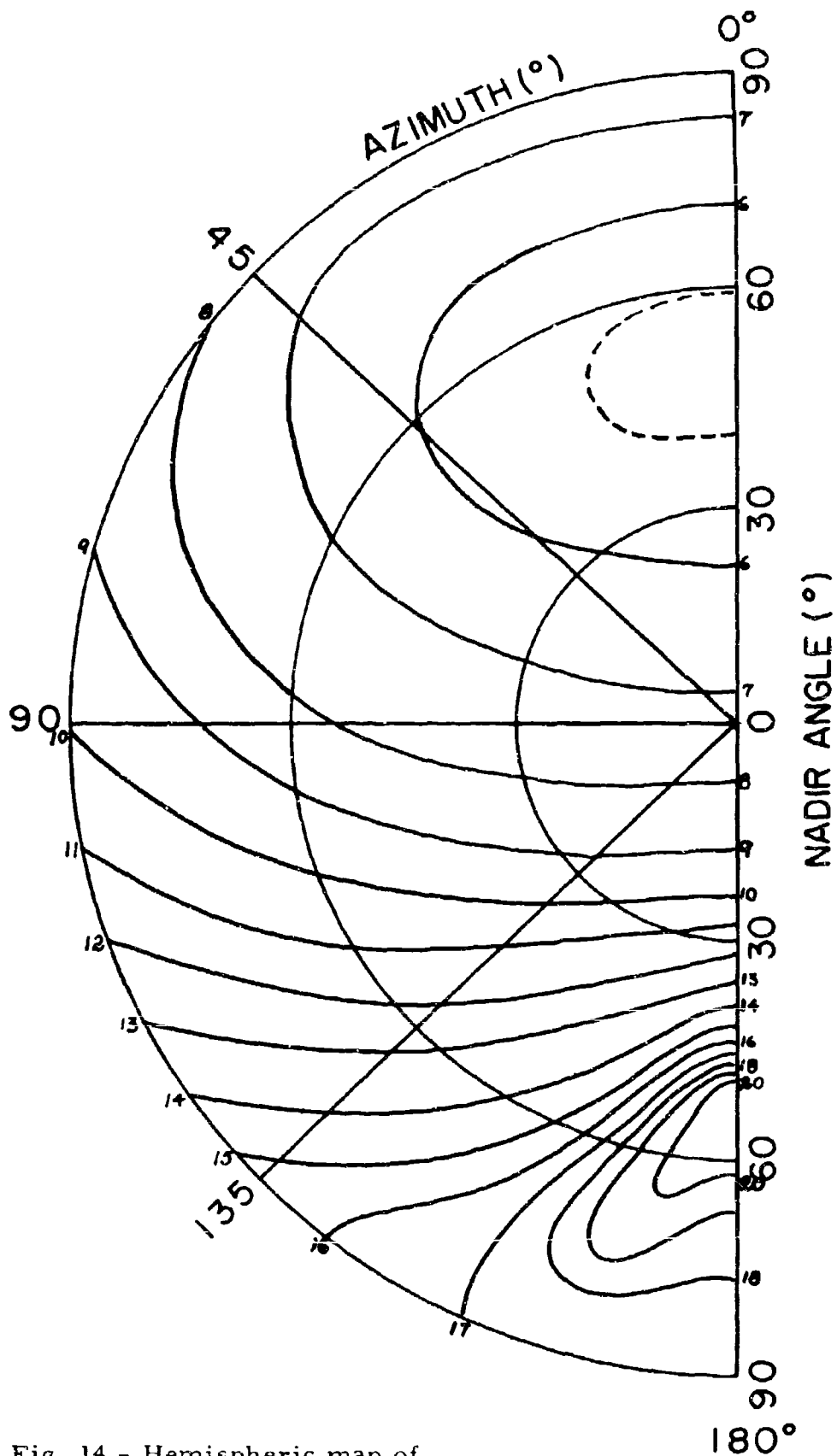


Fig. 14 - Hemispheric map of the directional reflectance of black loam soil ($\theta_0 = 53.1^\circ$, $\lambda = 6430\text{\AA}$)

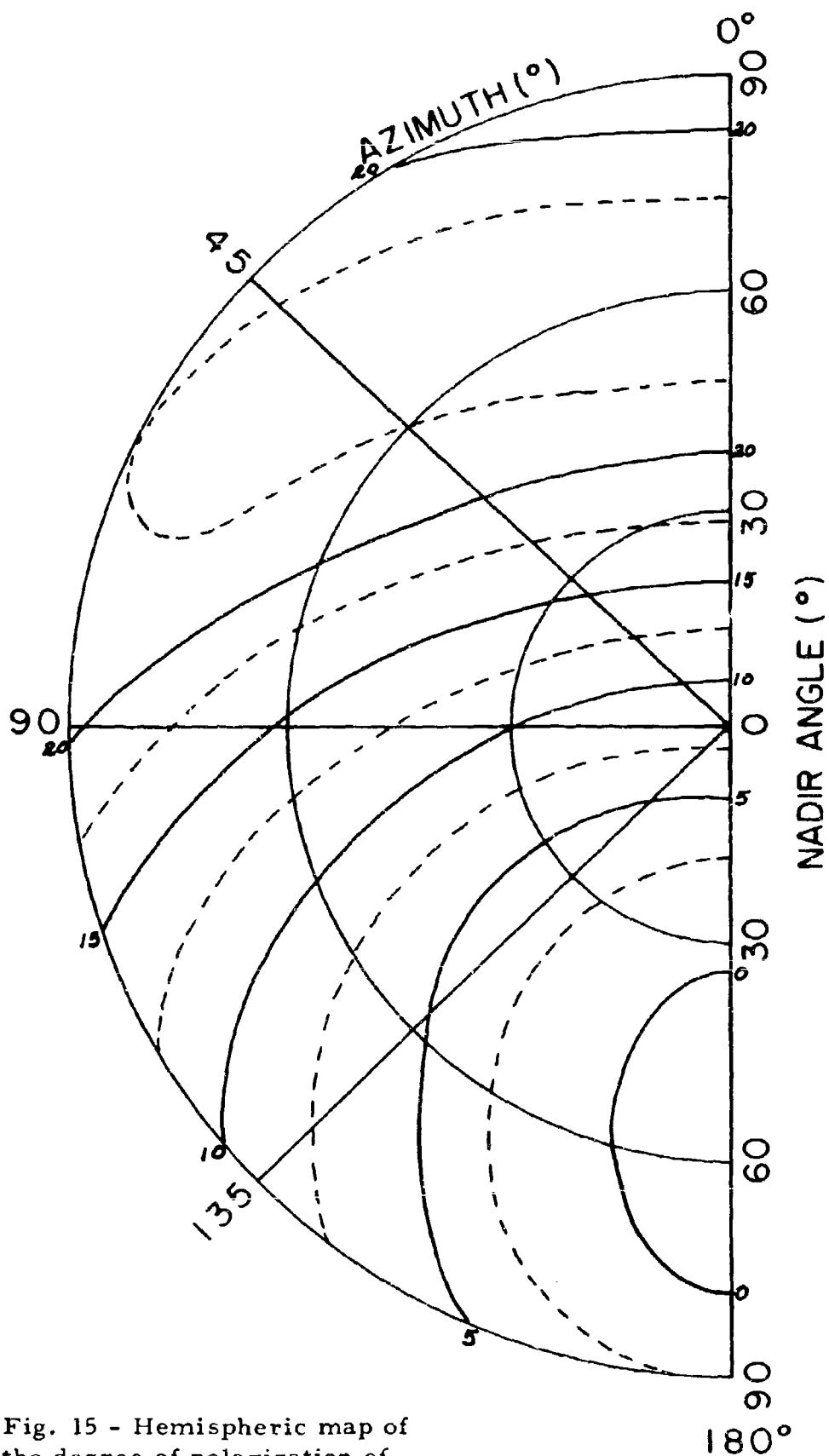


Fig. 15 - Hemispheric map of the degree of polarization of radiation reflected from black loam soil ($\theta_0 = 53.1^\circ$, $\lambda = 6430\text{\AA}$)

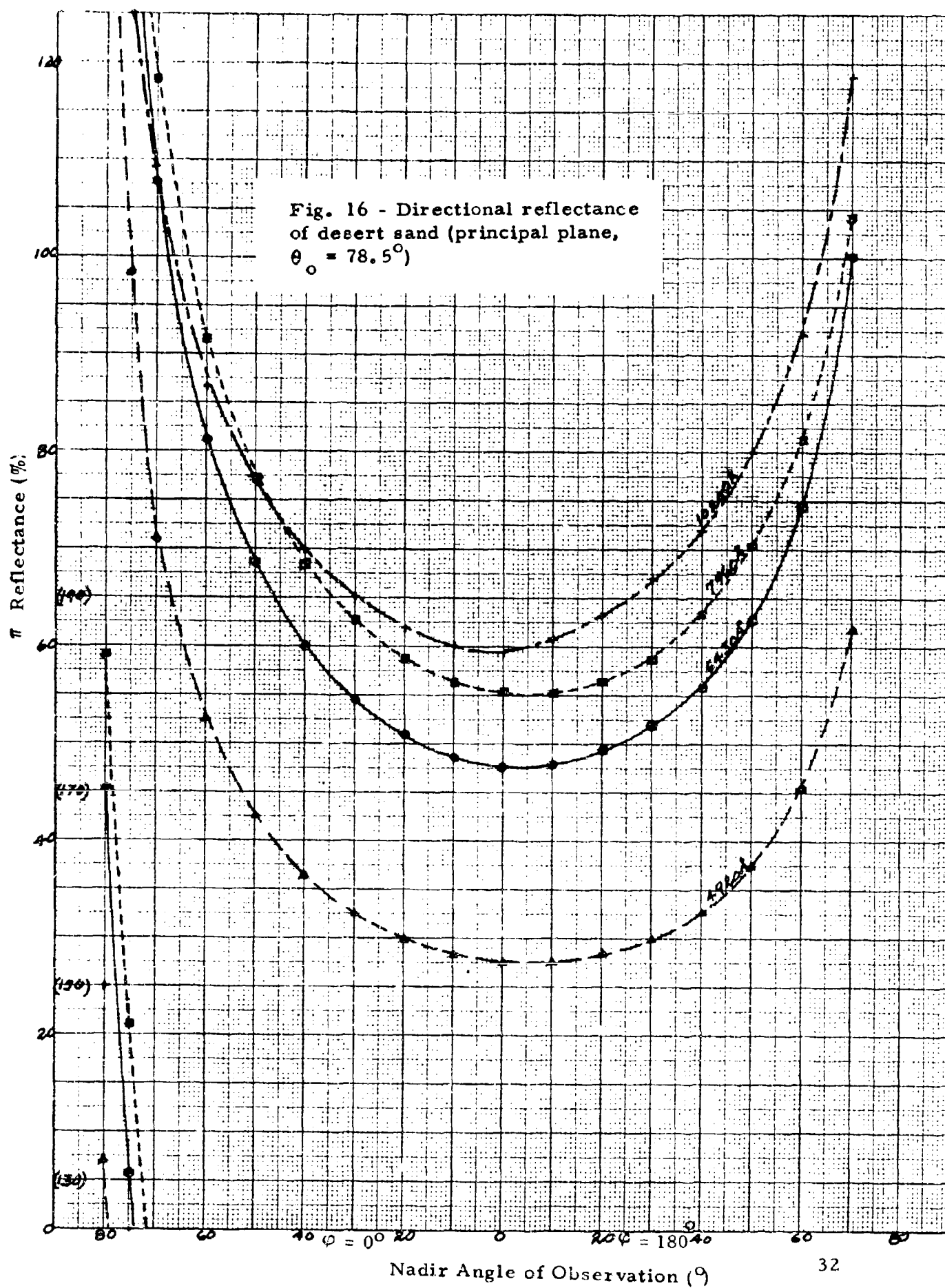


Fig. 17 - Degree of polarization of radiation reflected from desert sand (principal plane, $\theta_0 = 78.5^\circ$)

Degree of Polarization (%)

20

10

0

-10

Nadir Angle of Observation ($^\circ$)

180

Fig. 18 - Directional reflectance
of desert sand (principal plane,
 $\theta_o = 53.1^\circ$)

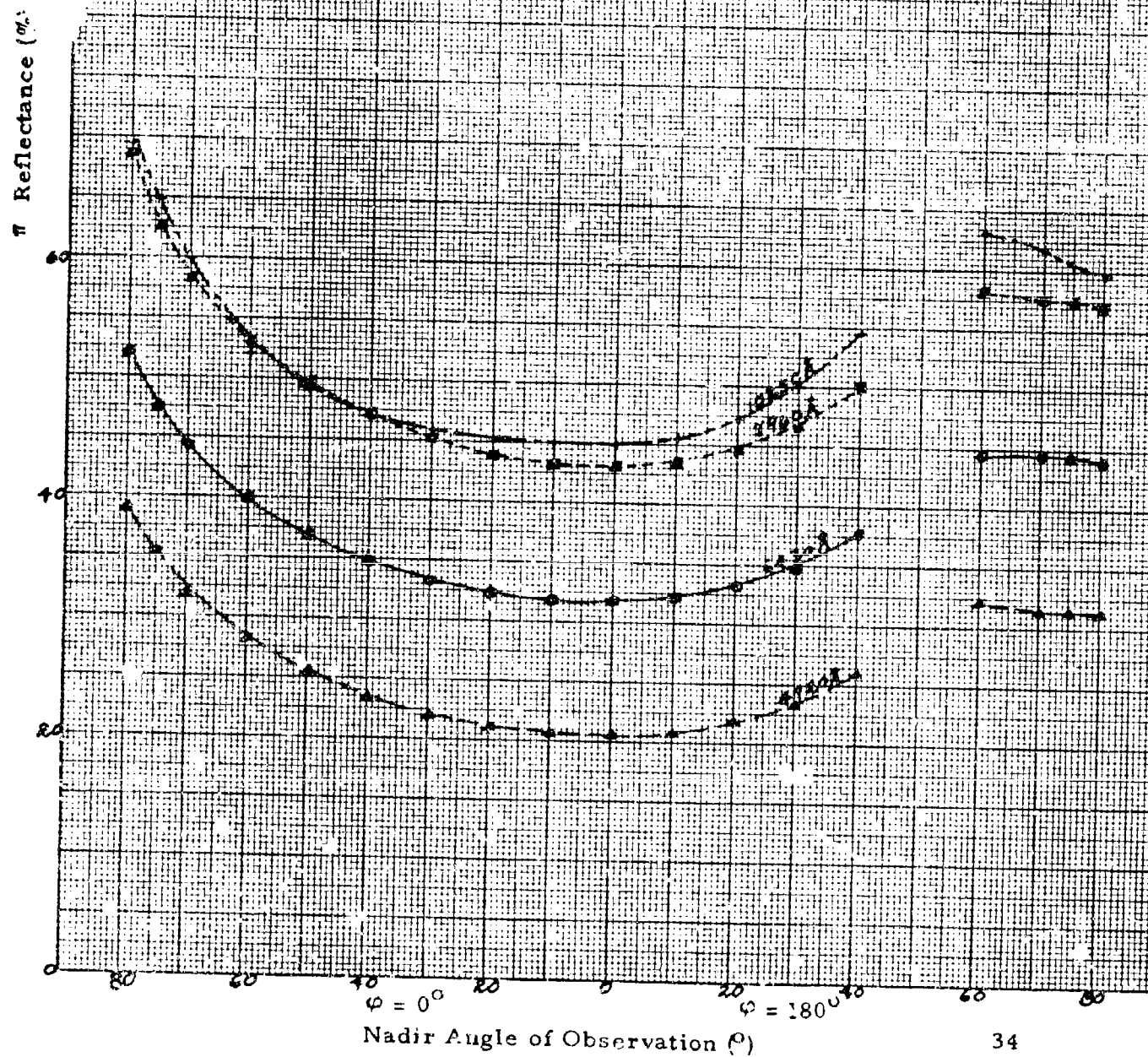


Fig. 19 - Degree of polarization
of radiation reflected from desert
sand (principal plane, $\theta_0 = 53.1^\circ$)

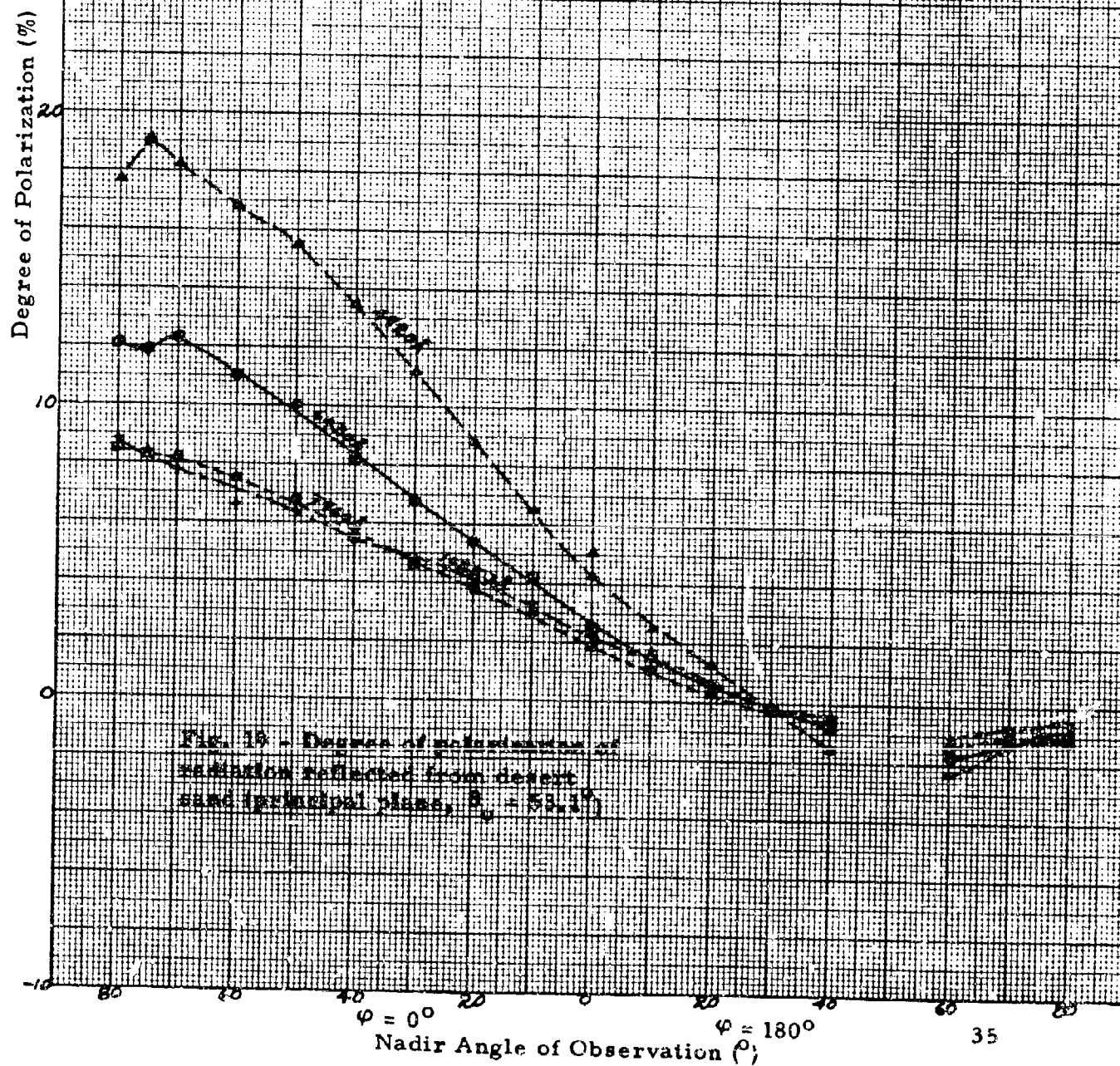
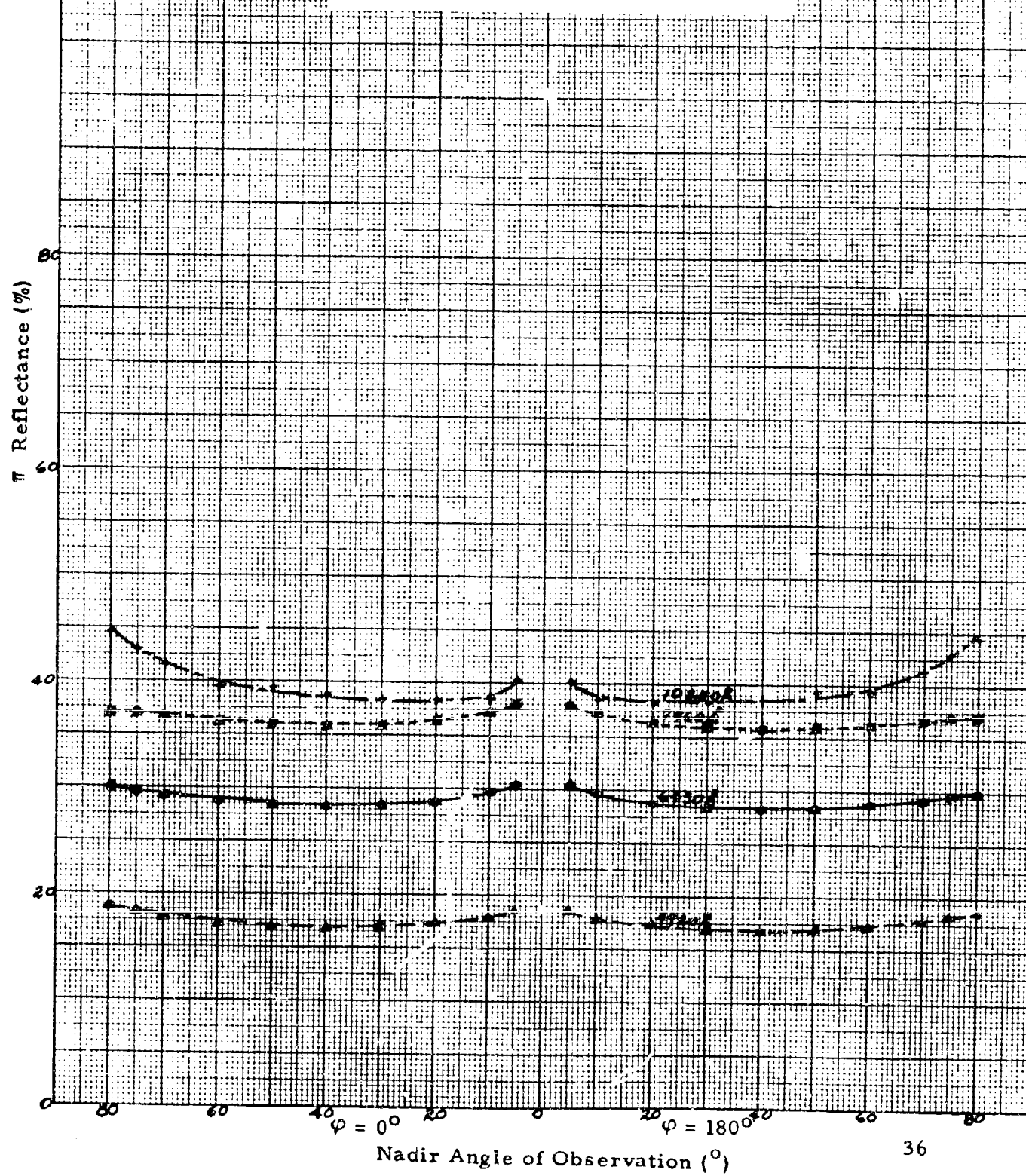


Fig. 18 - Degree of polarization of
radiation reflected from desert
sand (principal plane, $\theta_0 = 53.1^\circ$)

Fig. 20 - Directional reflectance
of desert sand (results independent
of azimuth, $\theta_o = 0^\circ$)



Degree of Polarization (%)

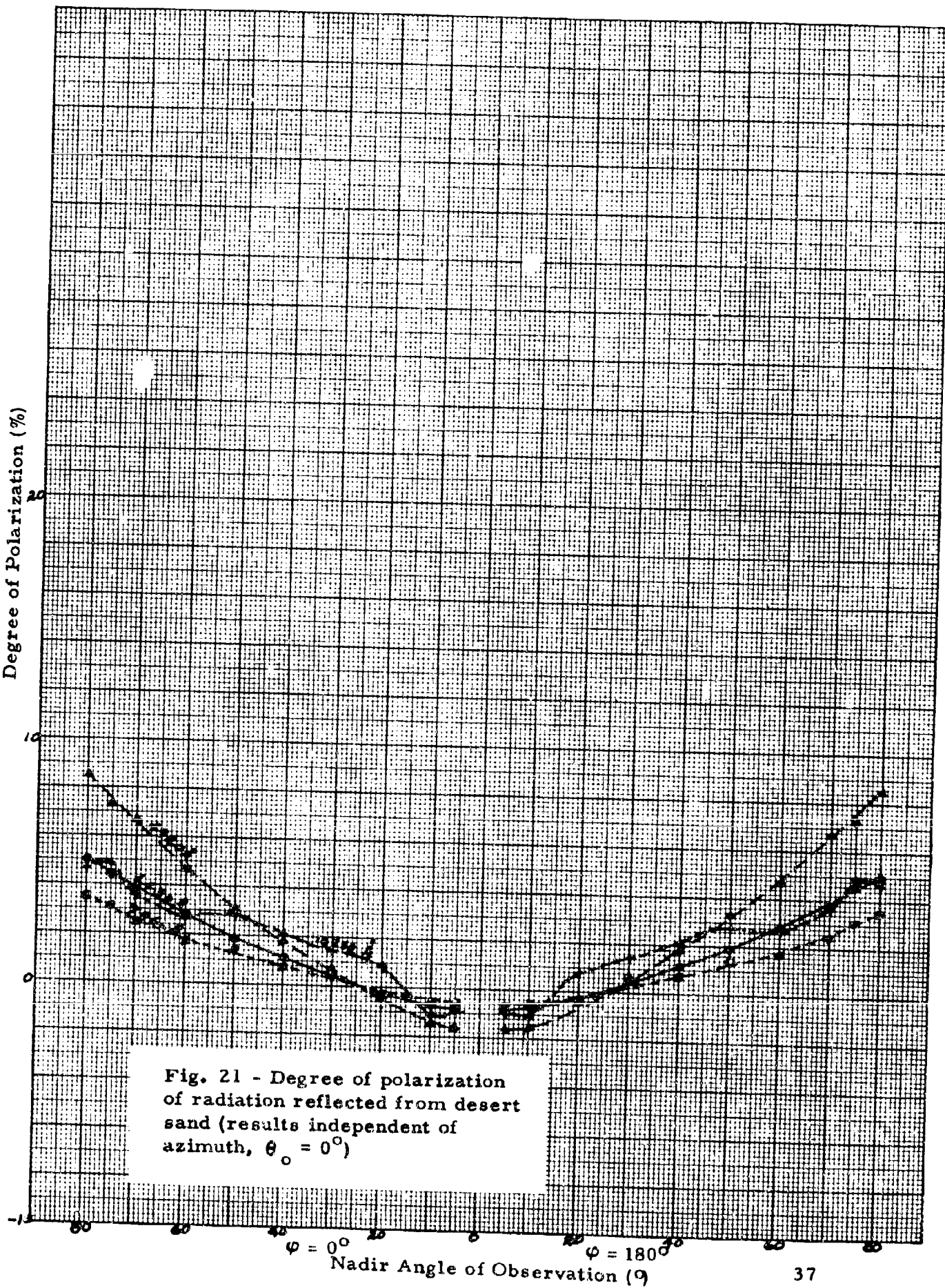


Fig. 21 - Degree of polarization of radiation reflected from desert sand (results independent of azimuth, $\theta_o = 0^\circ$)

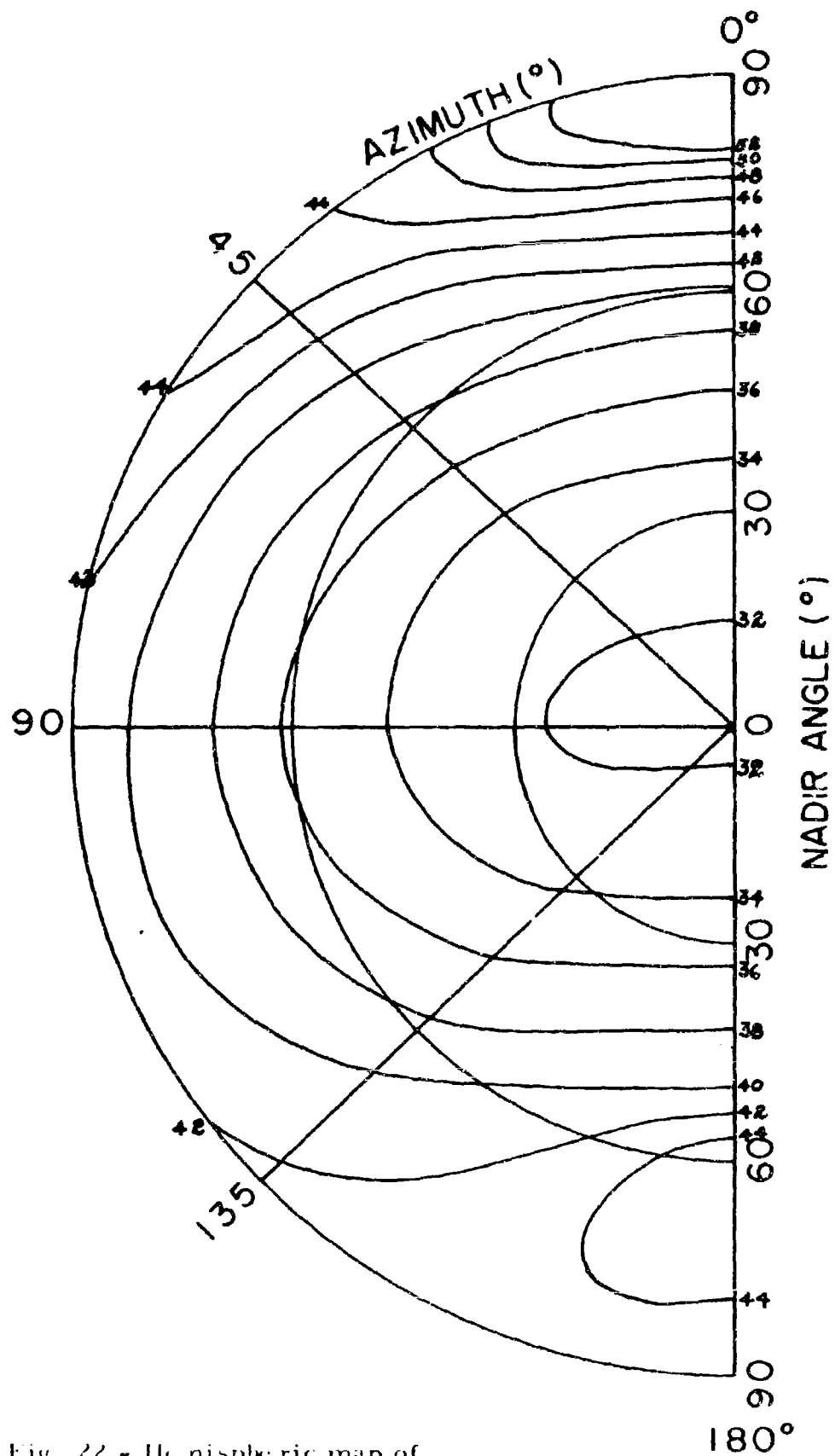


Fig. 22 - Hemispheric map of the directional reflectance of desert sand ($\theta_0 = 53.1^\circ$, $\lambda = 6430\text{\AA}$)

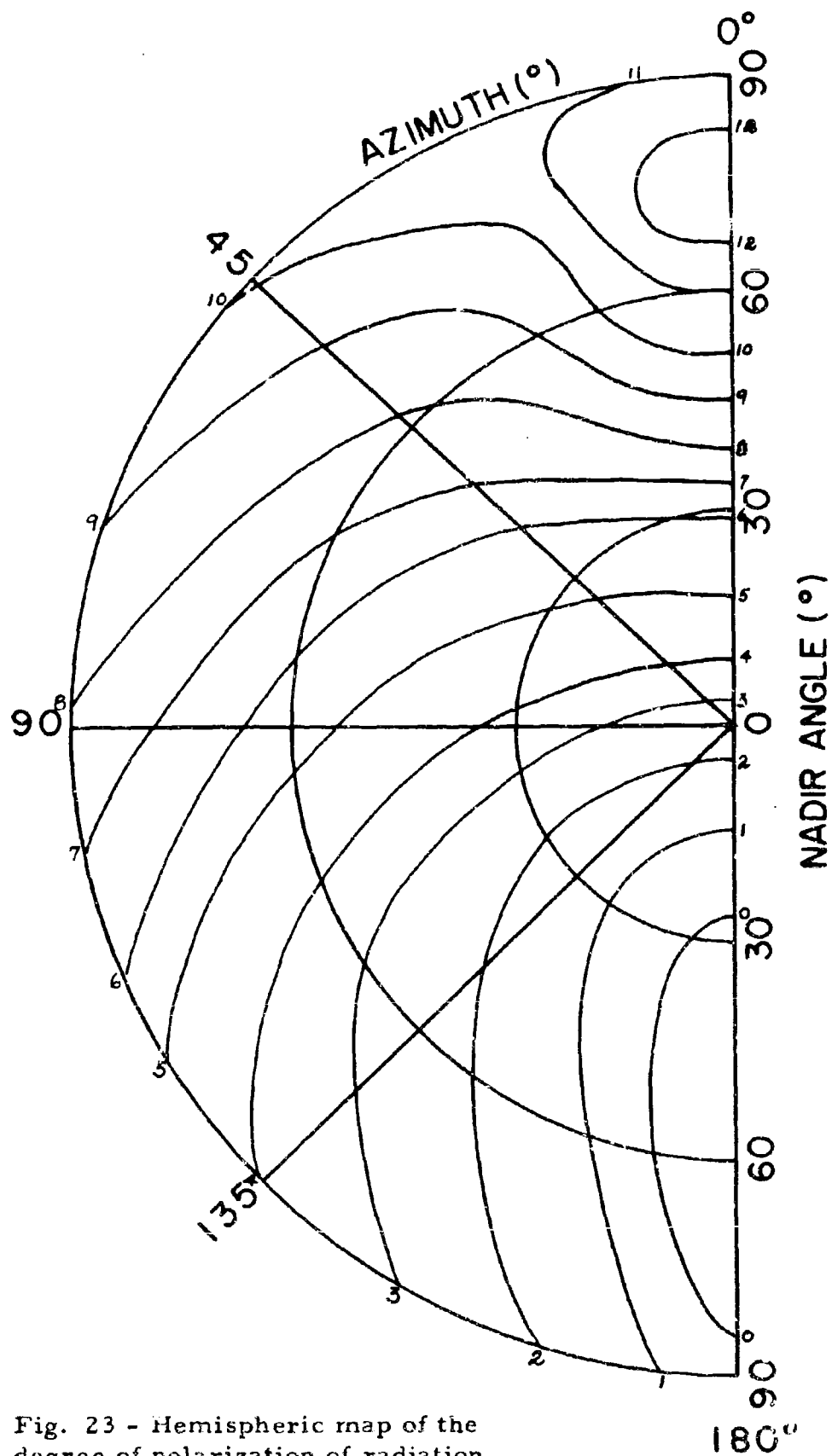


Fig. 23 - Hemispheric map of the degree of polarization of radiation reflected from desert sand ($\theta_0 = 53.1^\circ$, $\lambda = 6430\text{\AA}$)

below the surface being considerably darker than that just at the surface. The darkness was not due only to a change of moisture, as seen by an inspection of the collection site a few months later. The disturbed area still showed up as considerably darker than its surroundings in that case. The desert surface is obviously different in the two locations.

3. Green Grass

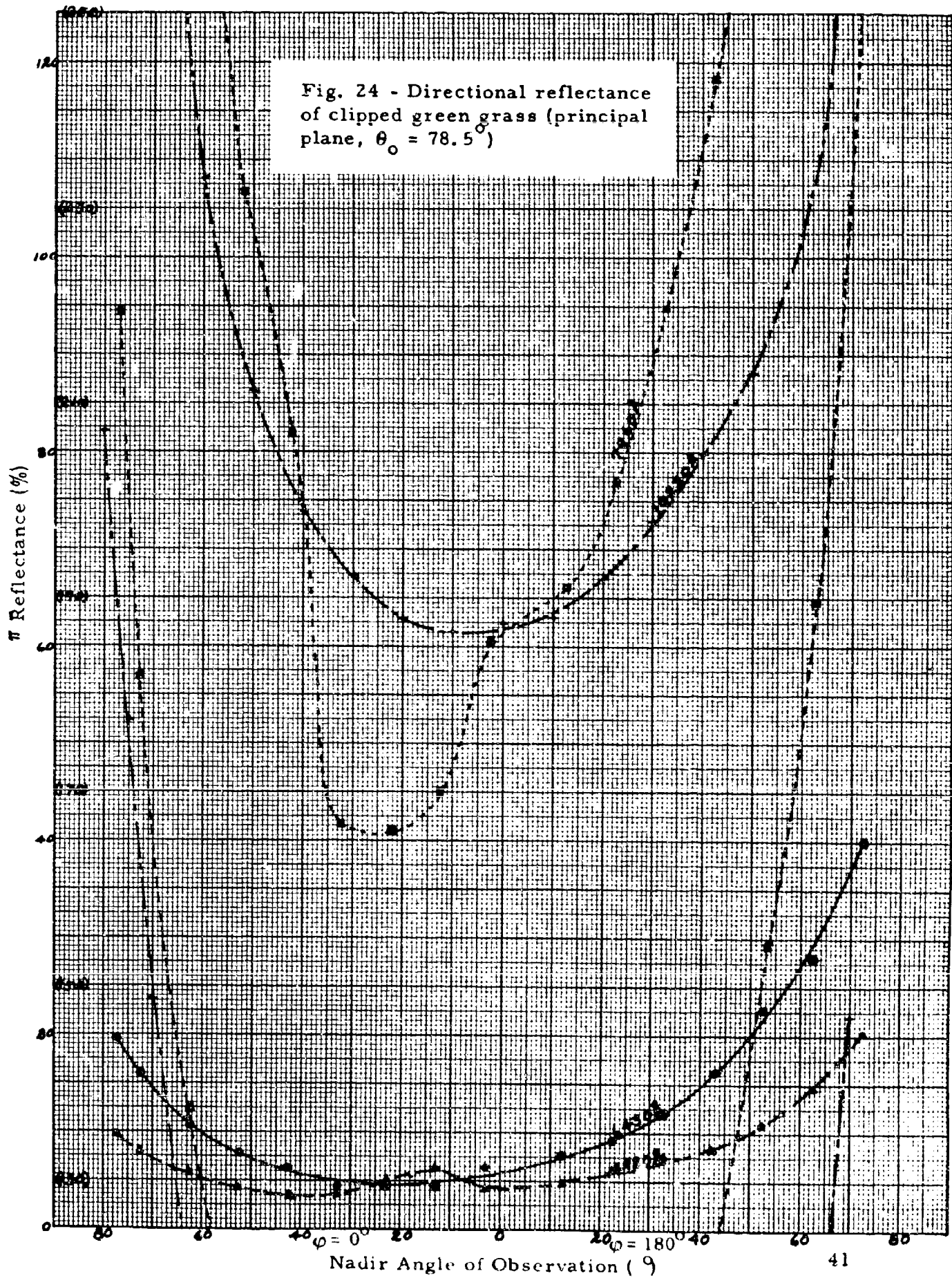
The sample of grass for which the data were taken is a lush, closely clipped blue grass obtained from a lawn near Philadelphia.

4. Dry Grass

This sample is also lush bluegrass, but it was permitted to die by lack of water. There are a few blades in which the chlorophyll has not bleached out although the entire sample is completely dry and shows no sign of life at present.

It can be seen from the curves that there is a discontinuity in the reflectance and polarization at $\theta = 0^\circ$. This comes about because of a preferred orientation of the blades of grass. The sample was taken from an operation in which strips of sod were being put on a lawn, so it had been part of a roll of sod. It can be seen by close inspection that the blades are more frequently bent in the direction toward the photometer as the sample was installed than in the opposite direction. As a consequence the incident light penetrated more deeply into the grass for the measurements at $\varphi = 180^\circ$ than at $\varphi = 0^\circ$. One can conceive of conditions in which such an effect would be of interest.

Fig. 24 - Directional reflectance
of clipped green grass (principal
plane, $\theta_0 = 78.5^\circ$)



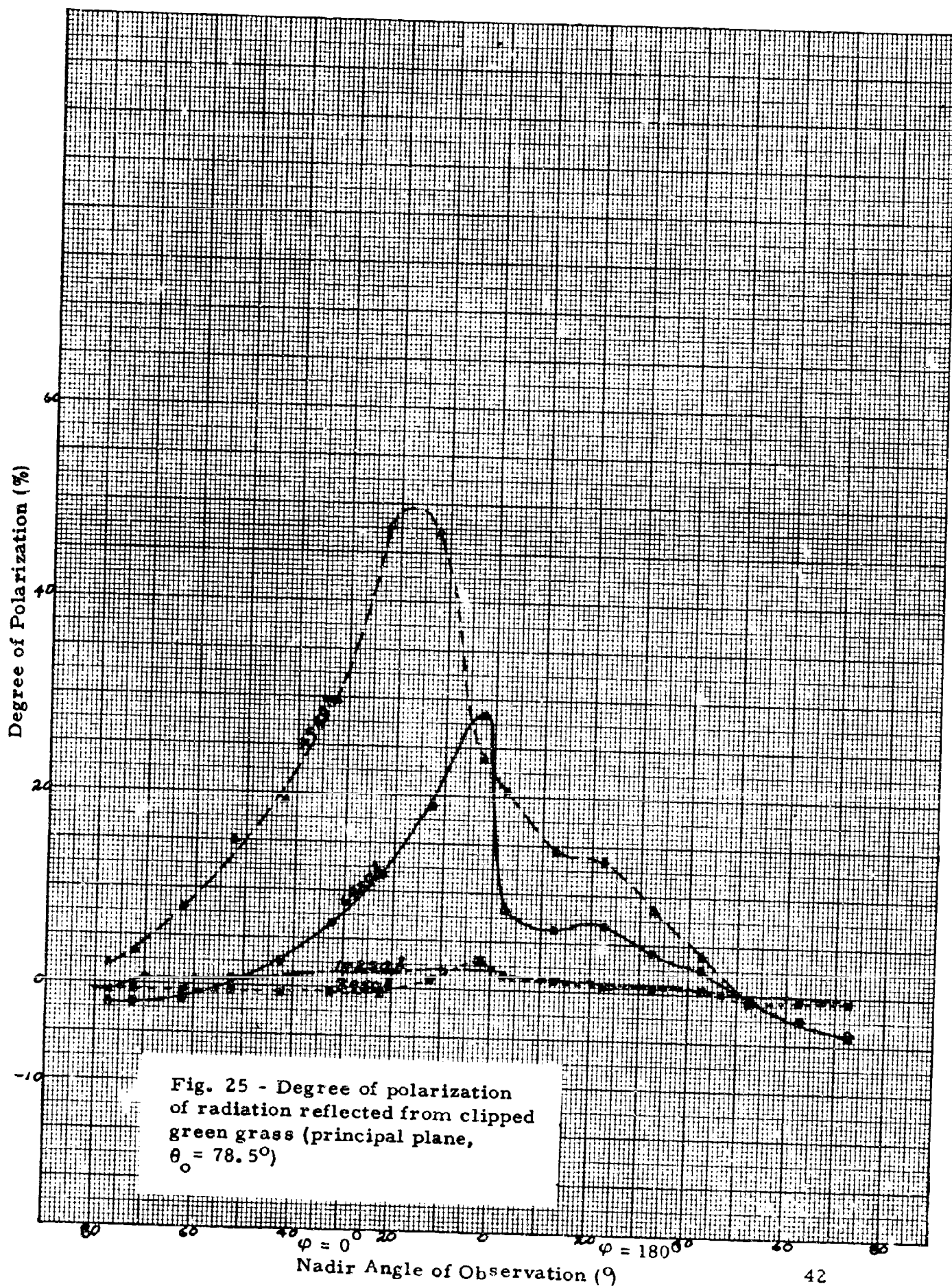
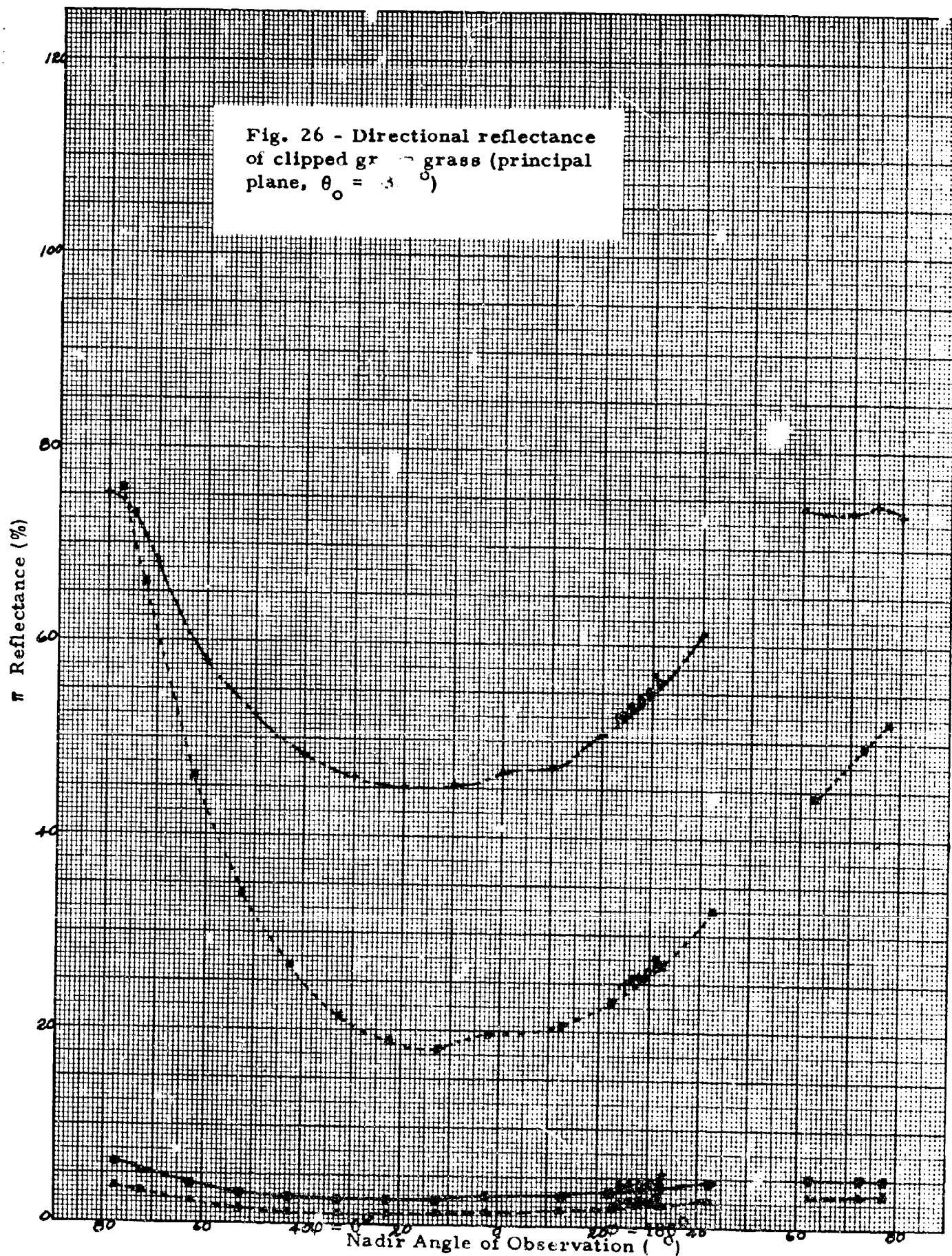


Fig. 26 - Directional reflectance of clipped grass (principal plane, $\theta_0 = 30^\circ$)



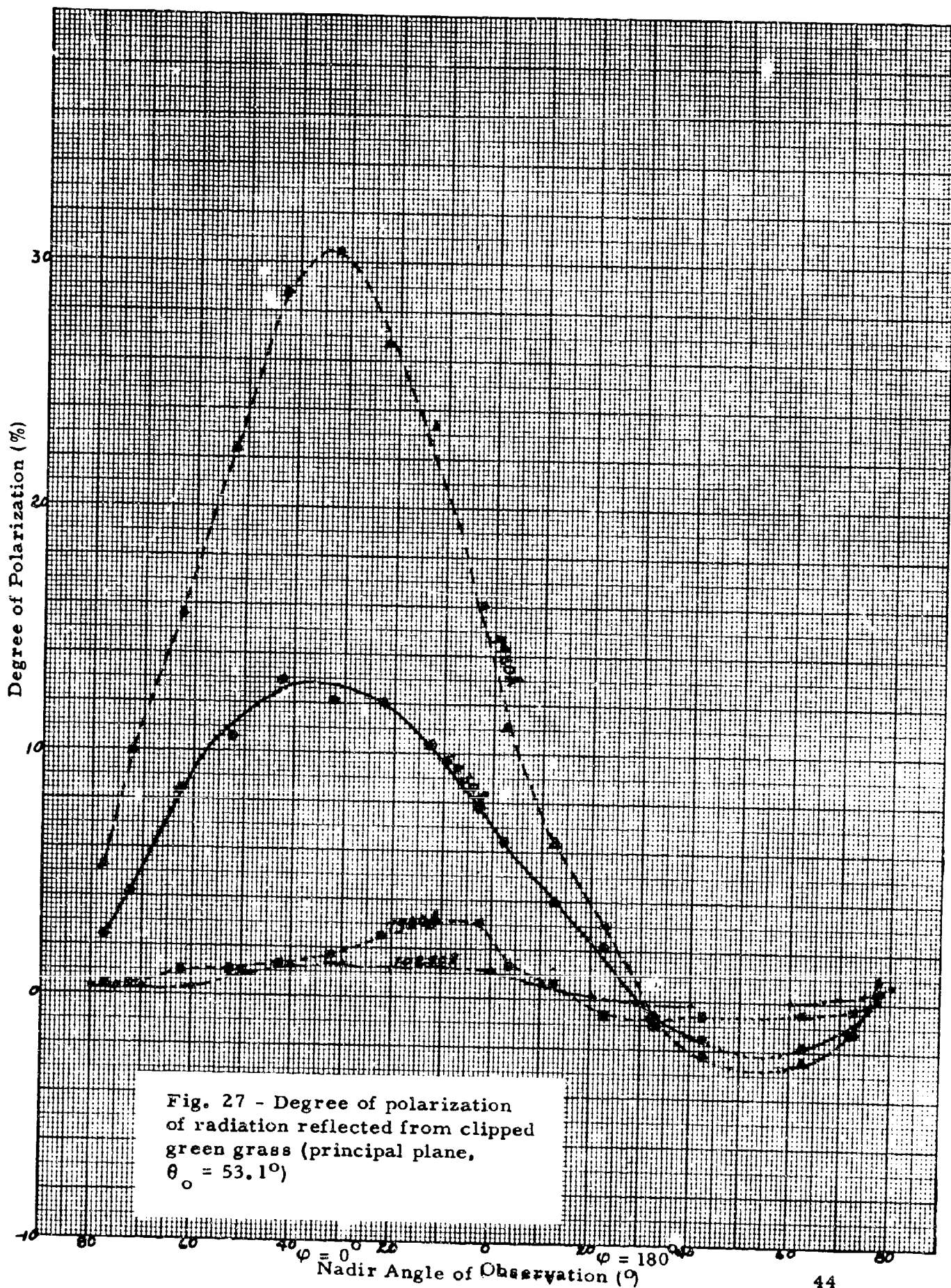
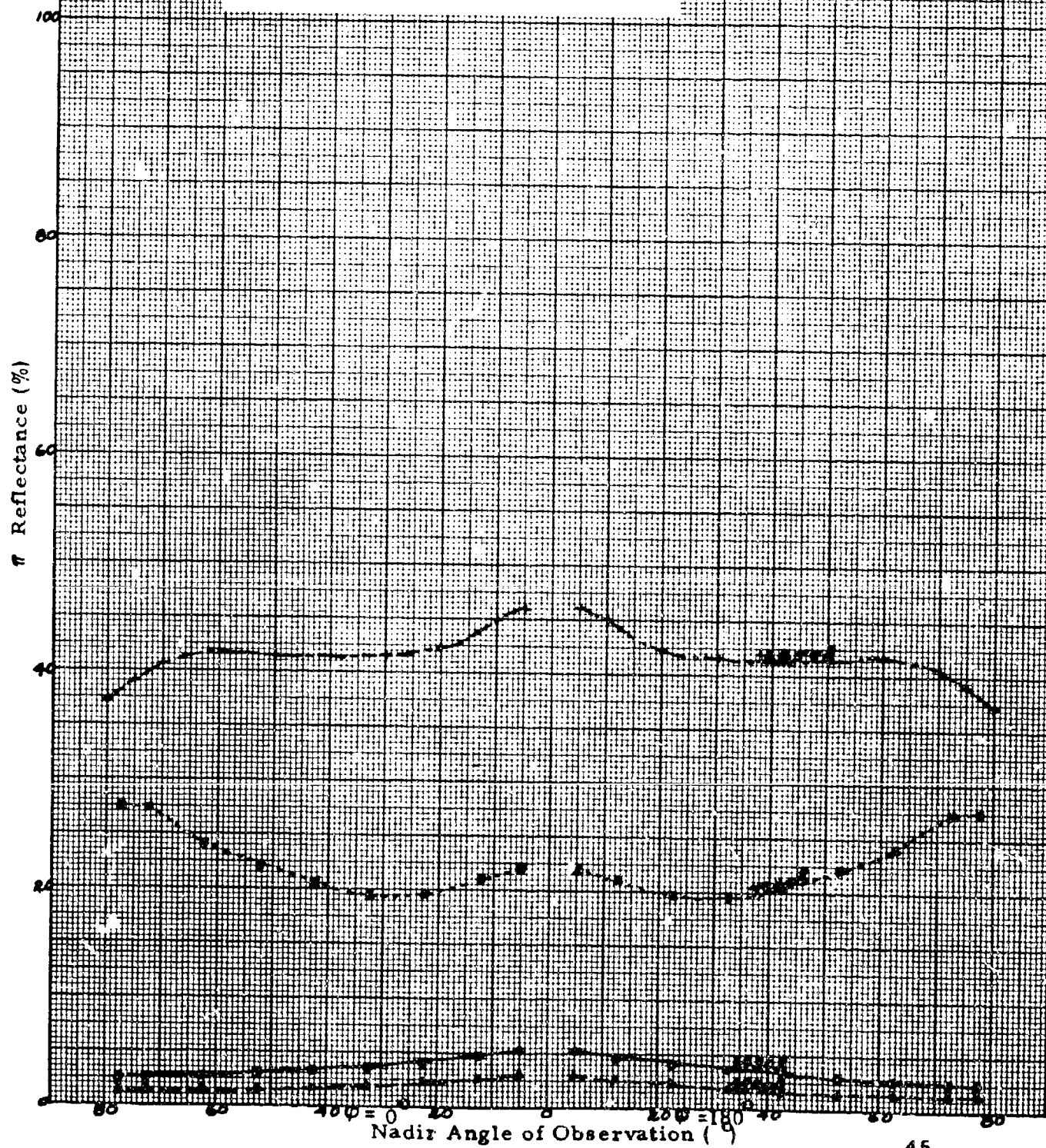
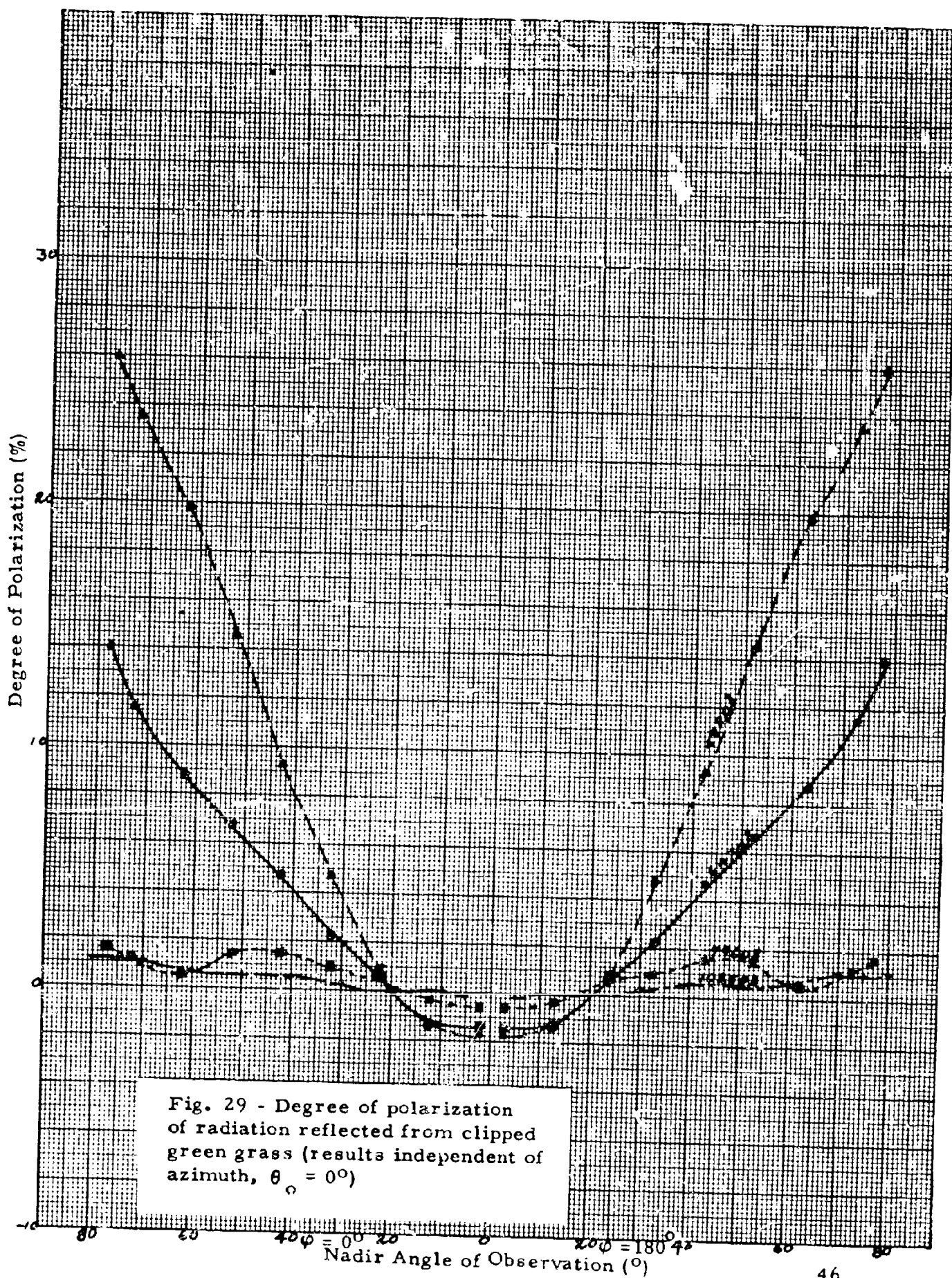


Fig. 28 - Directional reflectance
of clipped green grass (results
independent of azimuth, $\theta_0 = 0^\circ$)





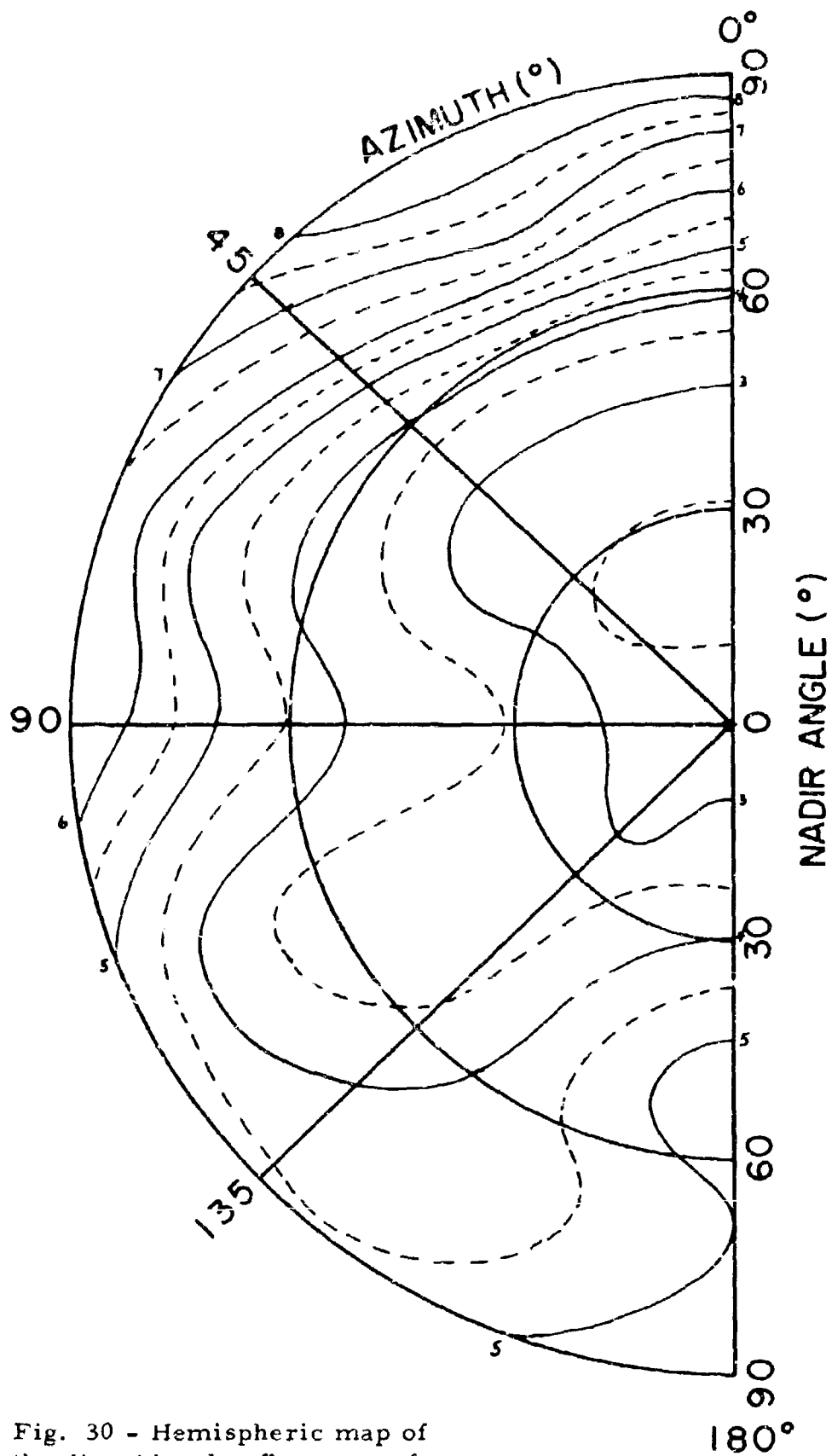


Fig. 30 - Hemispheric map of the directional reflectance of clipped green grass ($\theta_o = 53.1^\circ$, $\lambda = 6430\text{\AA}$)

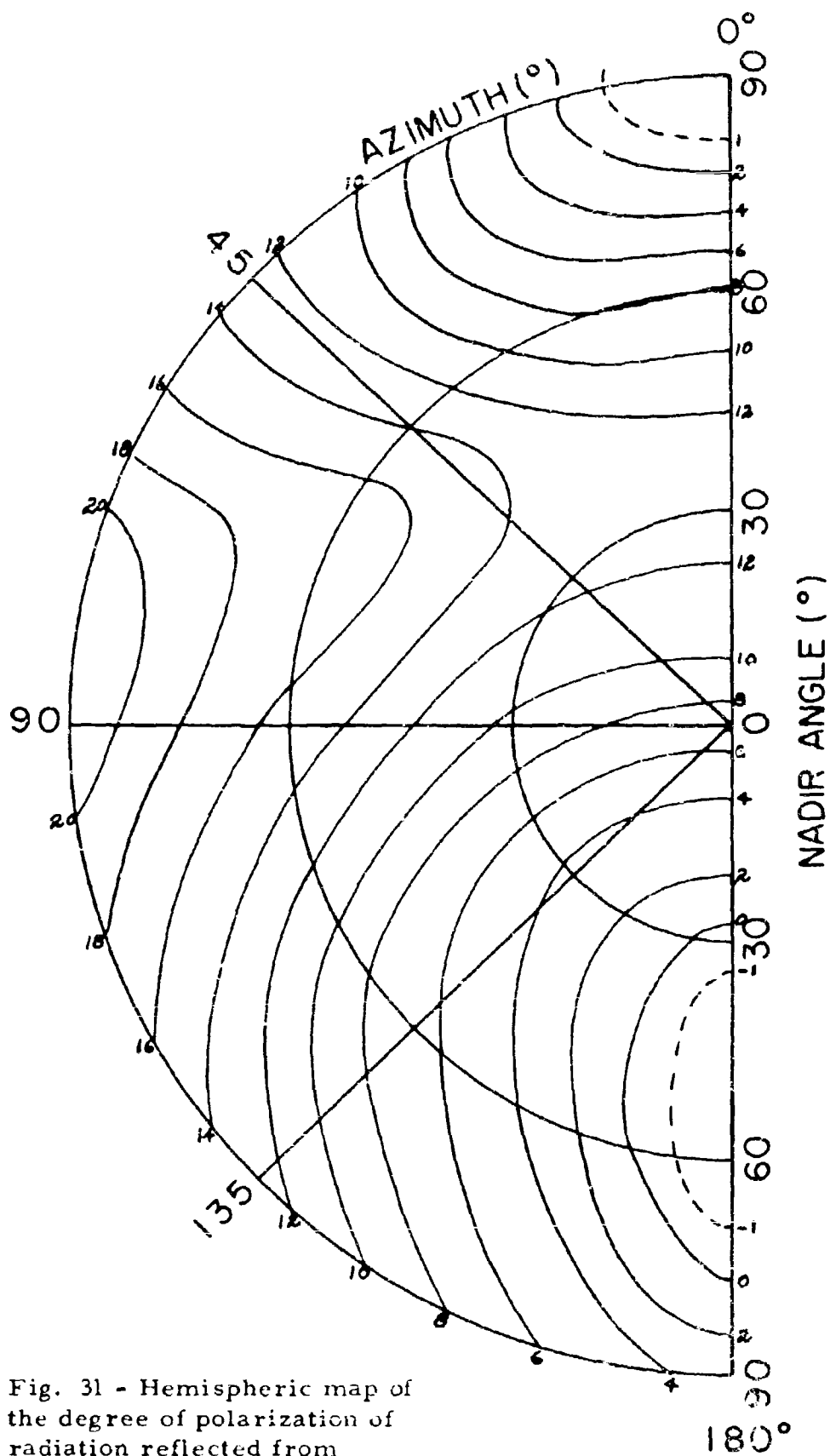


Fig. 31 - Hemispheric map of the degree of polarization of radiation reflected from clipped green grass ($\theta_0 = 53.1^\circ$, $\lambda = 6430\text{\AA}$)

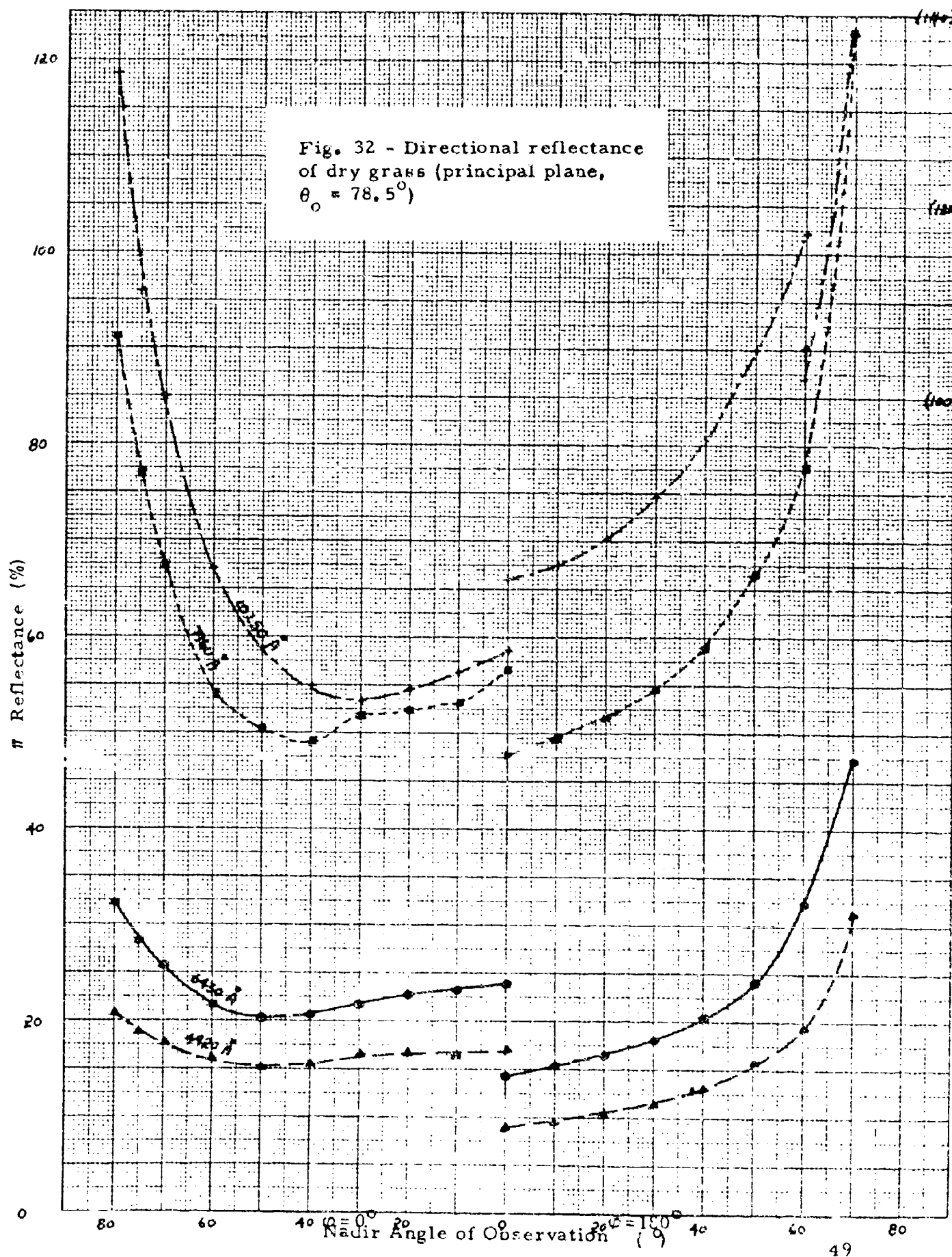


Fig. 33 - Degree of polarization of radiation reflected from dry grass (principal plane, $\theta_0 = 78.5^\circ$)

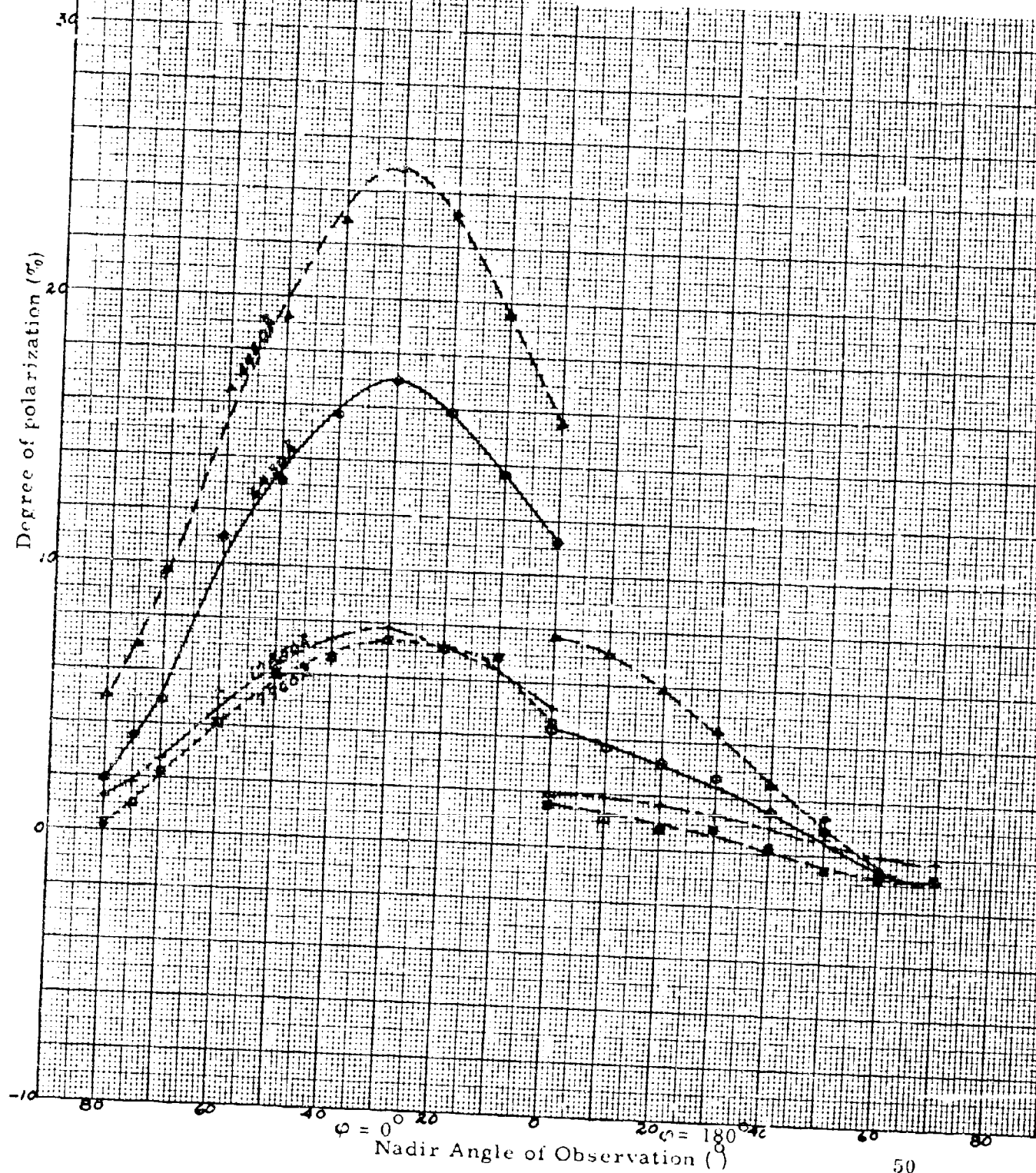


Fig. 34 - Directional reflectance
of dry grass (principal plane,
 $\theta_o = 53.1^\circ$)

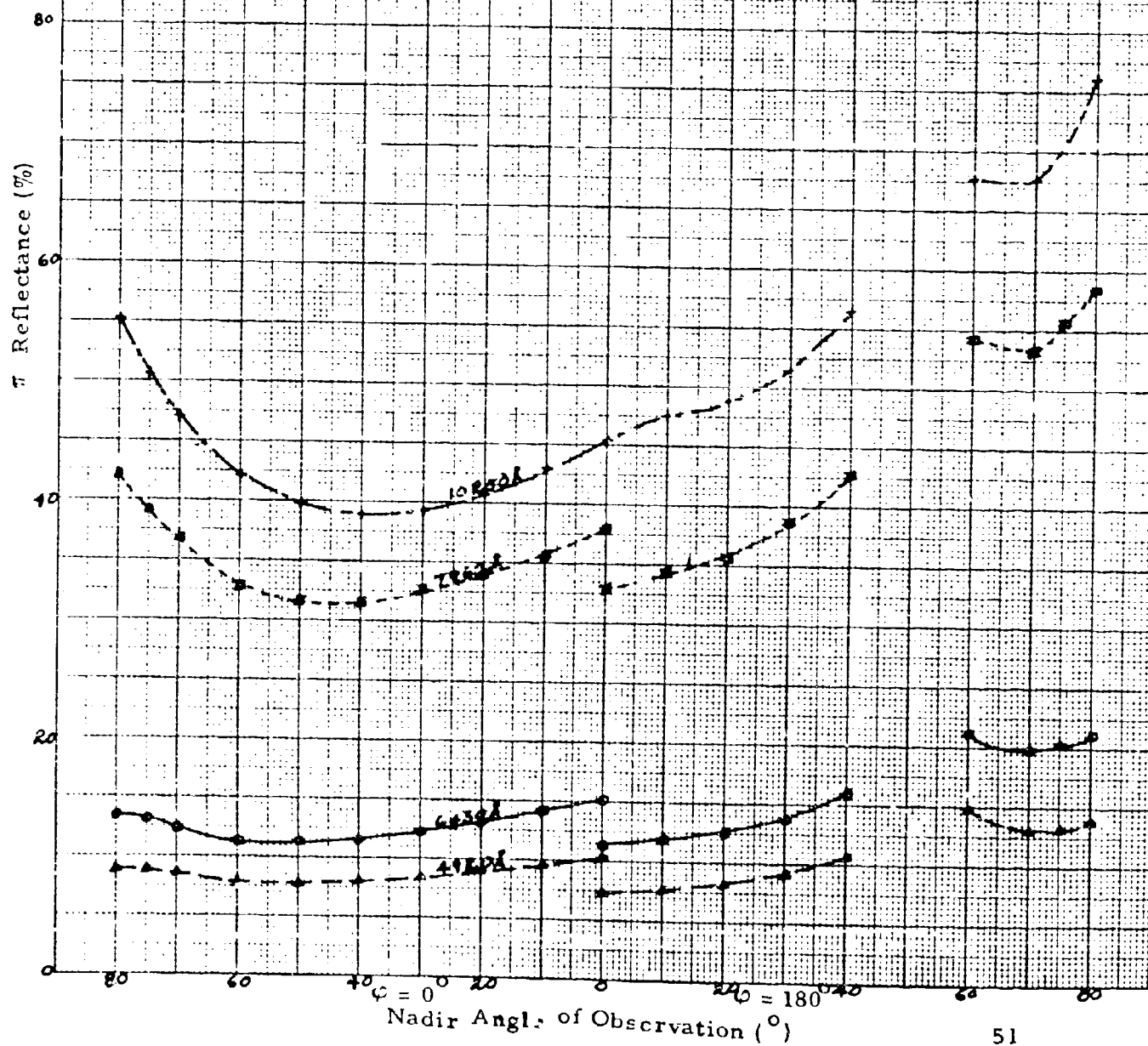


Fig. 35 - Degree of polarization
of radiation reflected from dry
grass (principal plane, $\theta_0 = 53.1^\circ$)

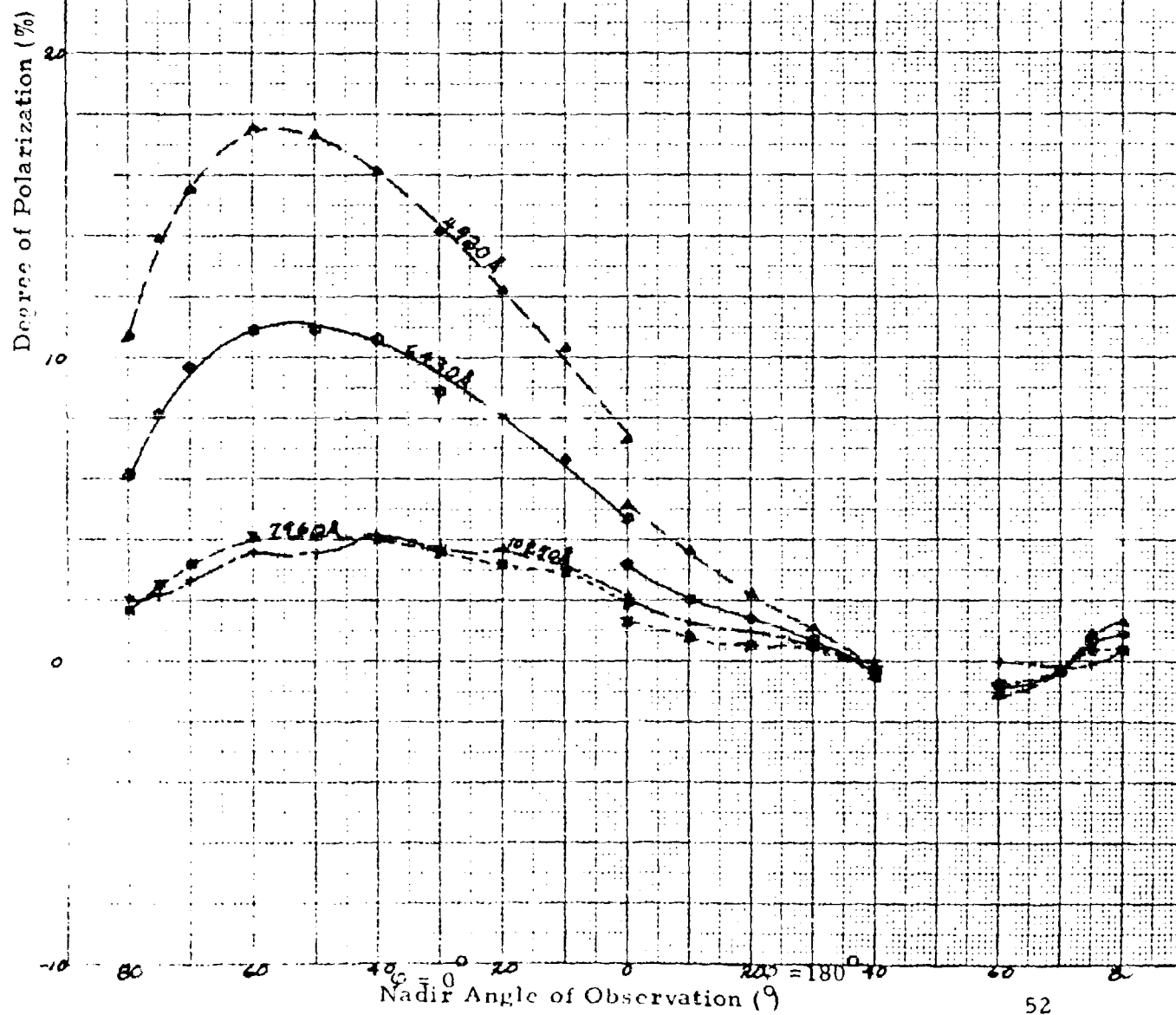
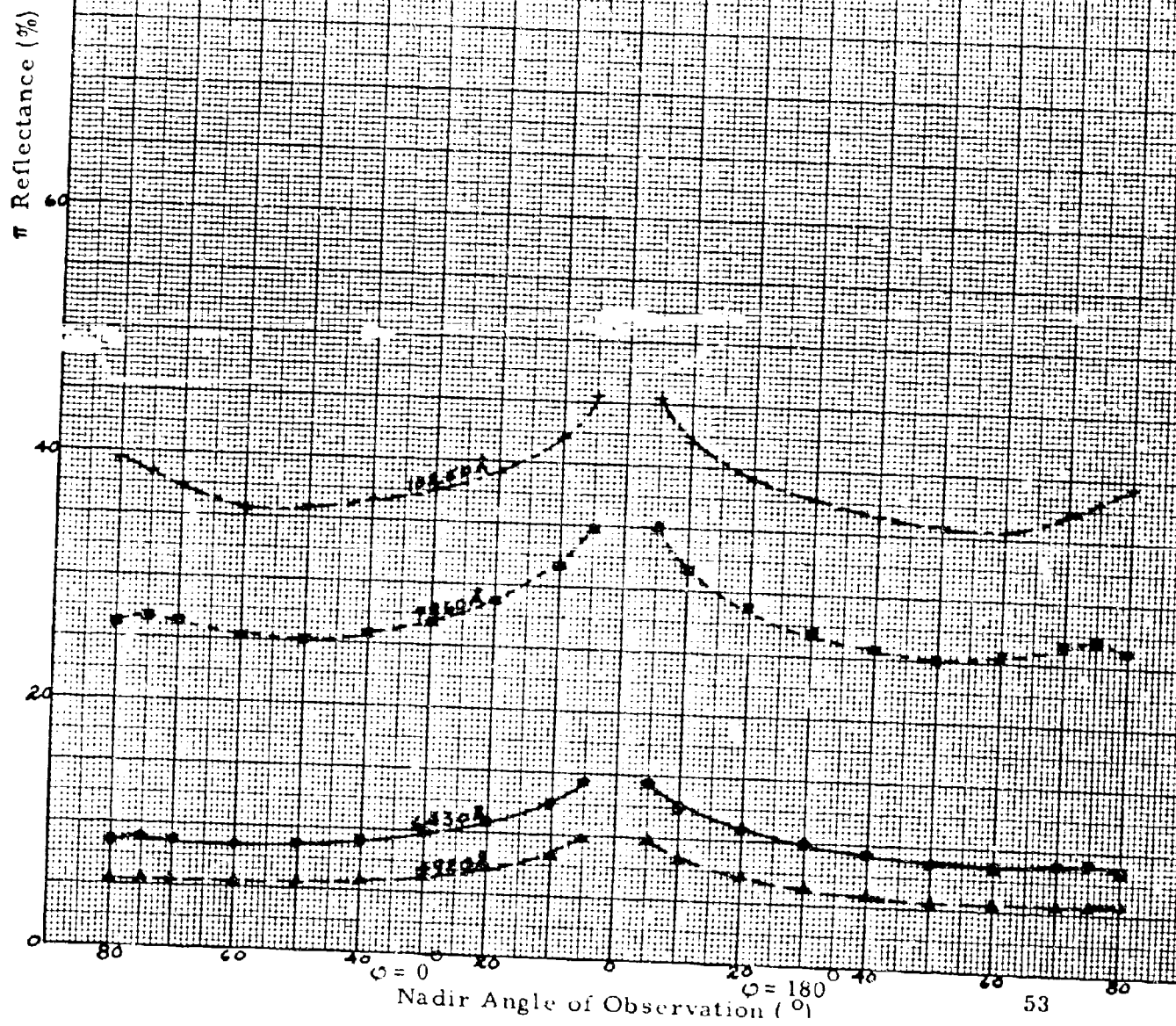


Fig. 36 - Directional reflectance of dry grass (results independent of azimuth, $\theta_0 = 0^\circ$)



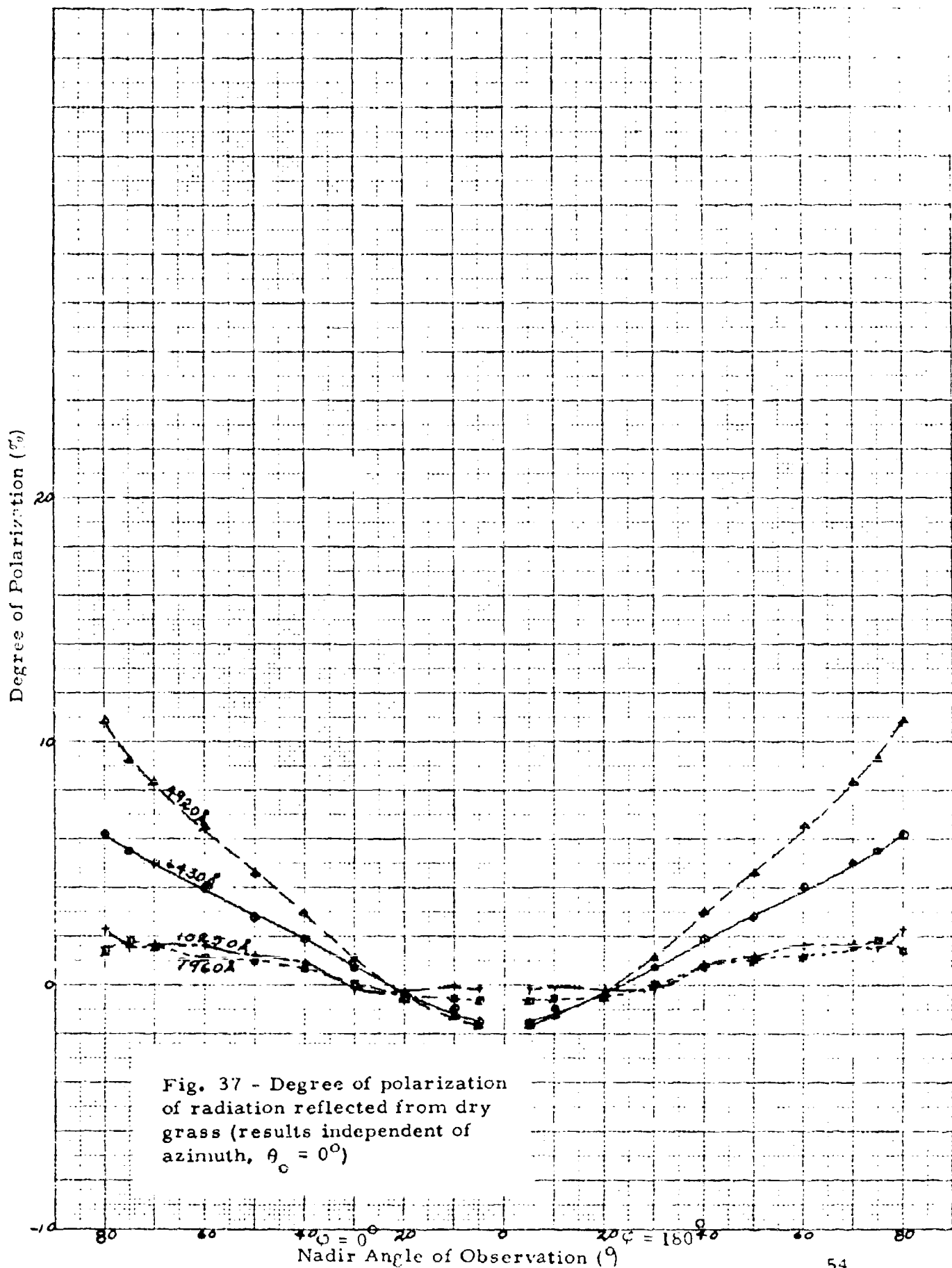


Fig. 37 - Degree of polarization of radiation reflected from dry grass (results independent of azimuth, $\theta_0 = 0^\circ$)

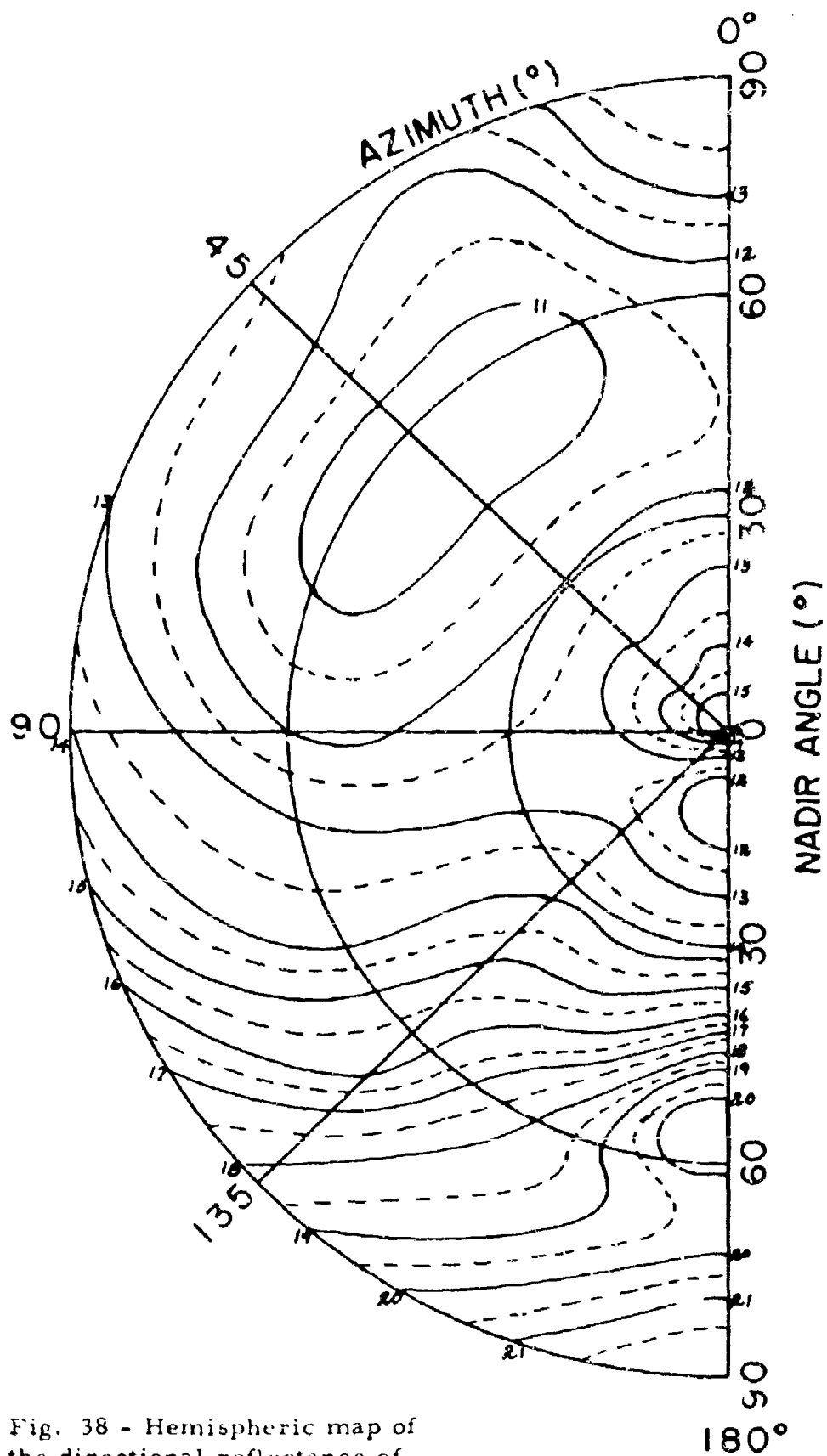


Fig. 38 - Hemispheric map of the directional reflectance of dry grass ($\theta_0 = 53.1^\circ$, $\lambda = 6430\text{\AA}$)

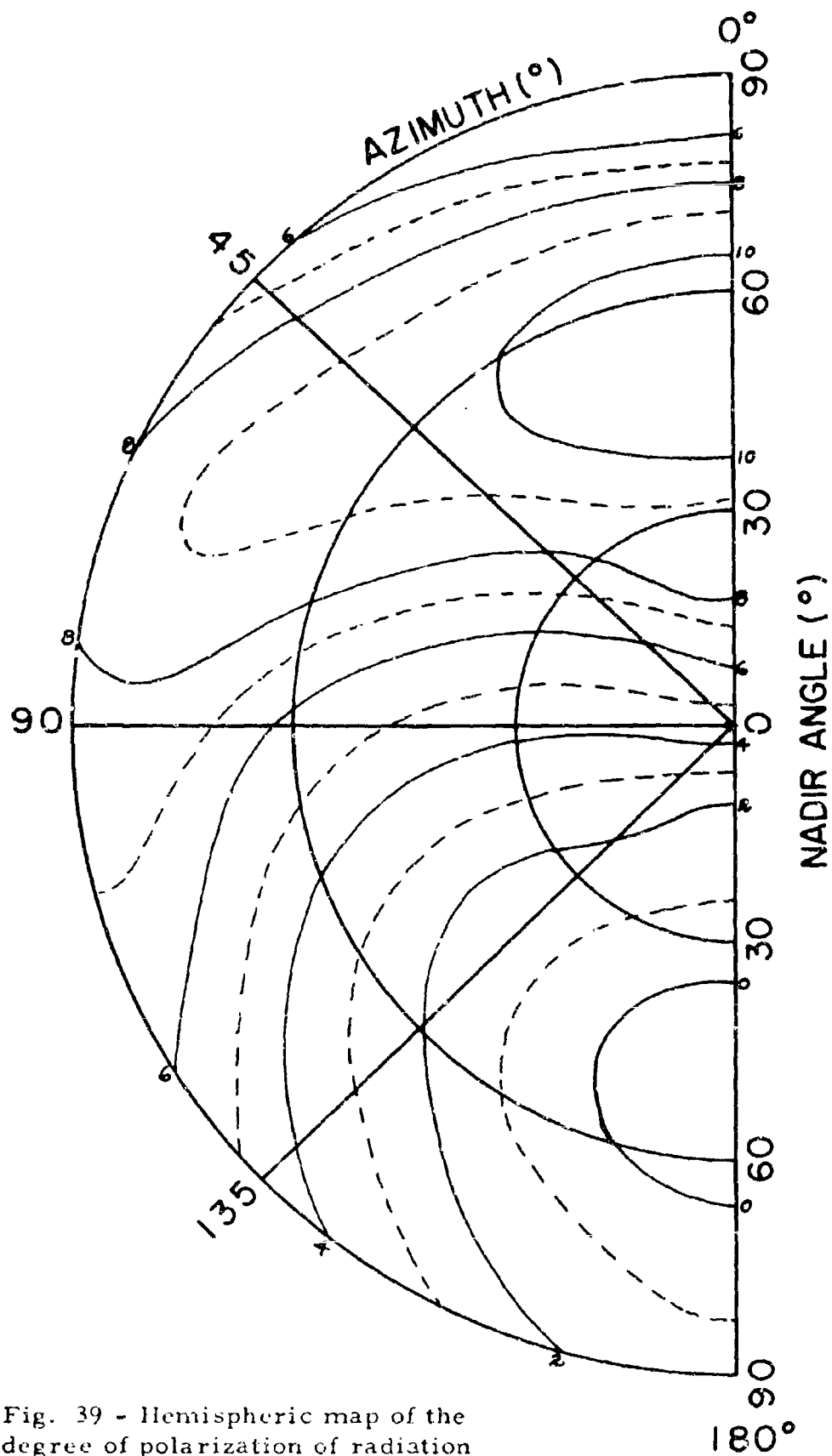


Fig. 39 - Hemispheric map of the degree of polarization of radiation reflected from dry grass ($\theta_0 = 53.1^\circ$, $\lambda = 6430\text{\AA}$)

5. Dead Leaves

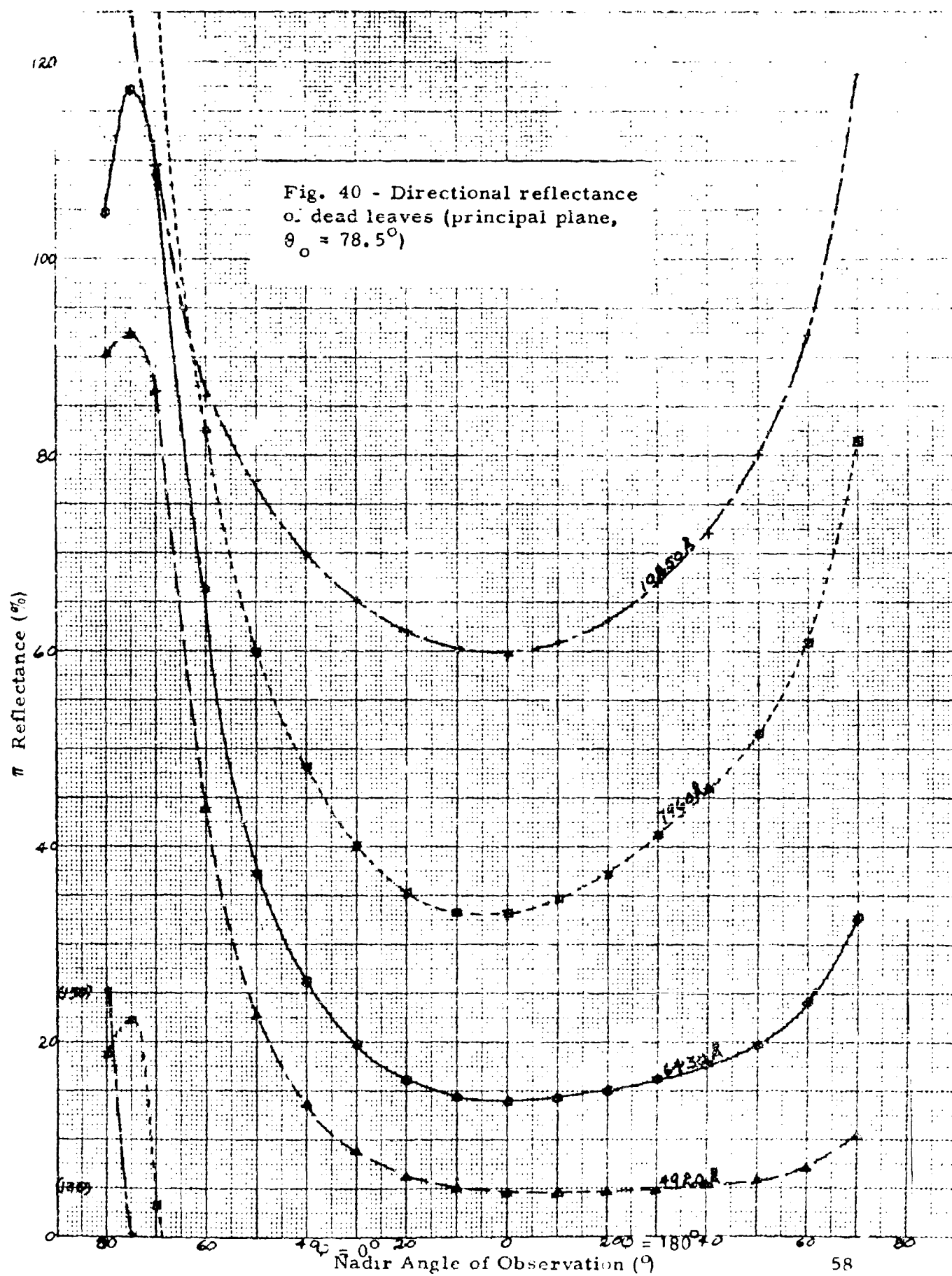
The leaves from which this sample was prepared were collected during the month of April from a wooded site in Valley Forge Park. They are leaves from the previous year's growth, and are mainly from oak trees. In order to make a reasonably uniform sample as seen with a field of view covering a small area, it was necessary to break the individual leaves up somewhat during the sample preparation. Otherwise the leaves were in their natural dry state during the measurements.

6. Broad-leafed Plants

This sample is composed of small individual plants of Japanese Spurge. The leaves are sufficiently dense so that no soil is visible through the canopy. The leaves themselves are of an average size of roughly two square inches, and do not appear either waxy or covered with fuzz. Their natural non-homogeneity when viewed with this small field instrument causes a considerable scatter in the measured data.

7. Crushed Limestone Gravel

This material is typical of the foundation often applied to roadbeds. It is graded as 3/4" size, although the individual particles vary in dimensions from roughly 1/2" to greater than 3/4". The particles are generally angular in shape as a result of the crushing process by which they are obtained from the massive limestone rock. This sample was obtained from the quarry located two miles northeast of Paoli, Pennsylvania.



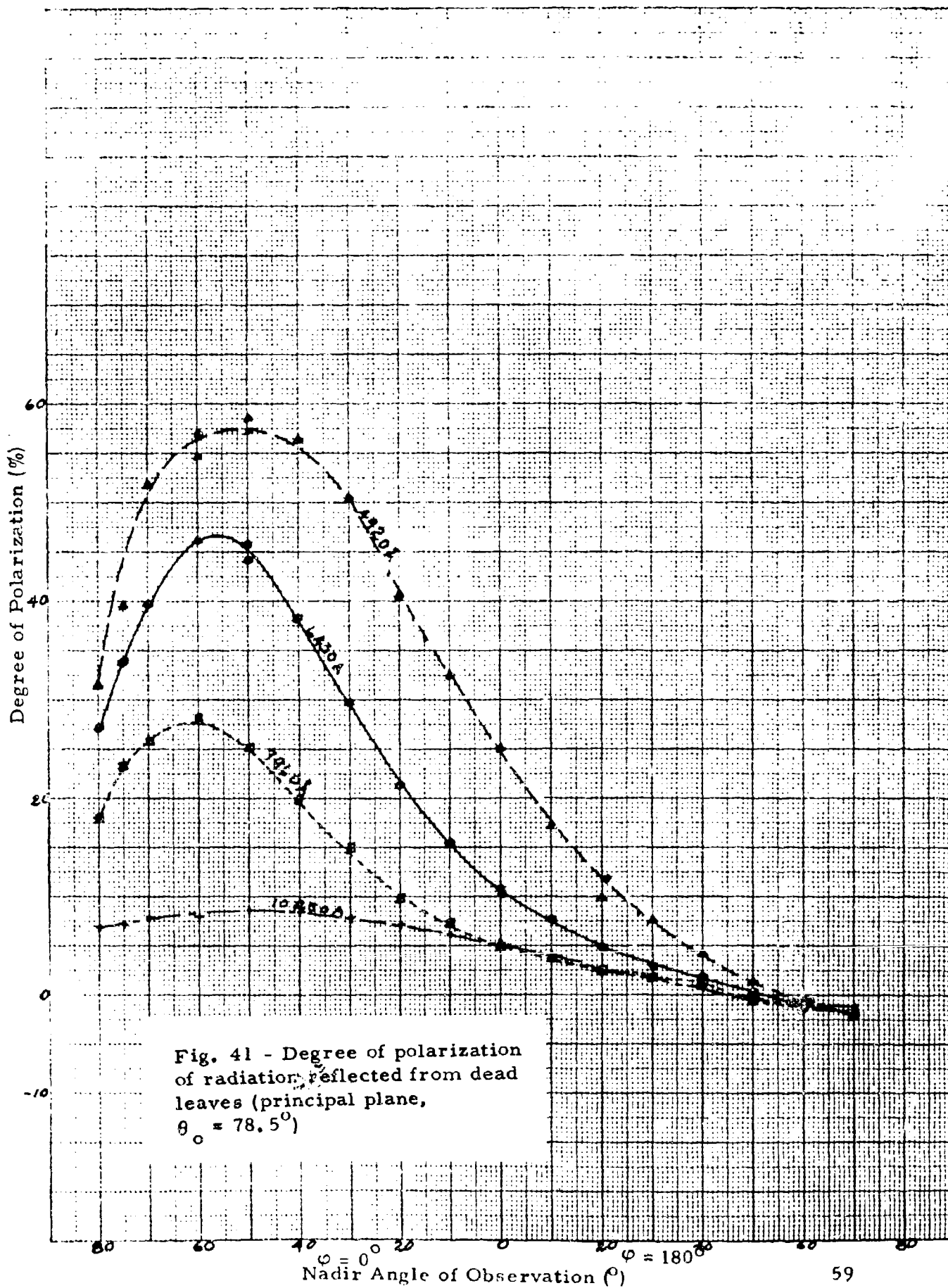
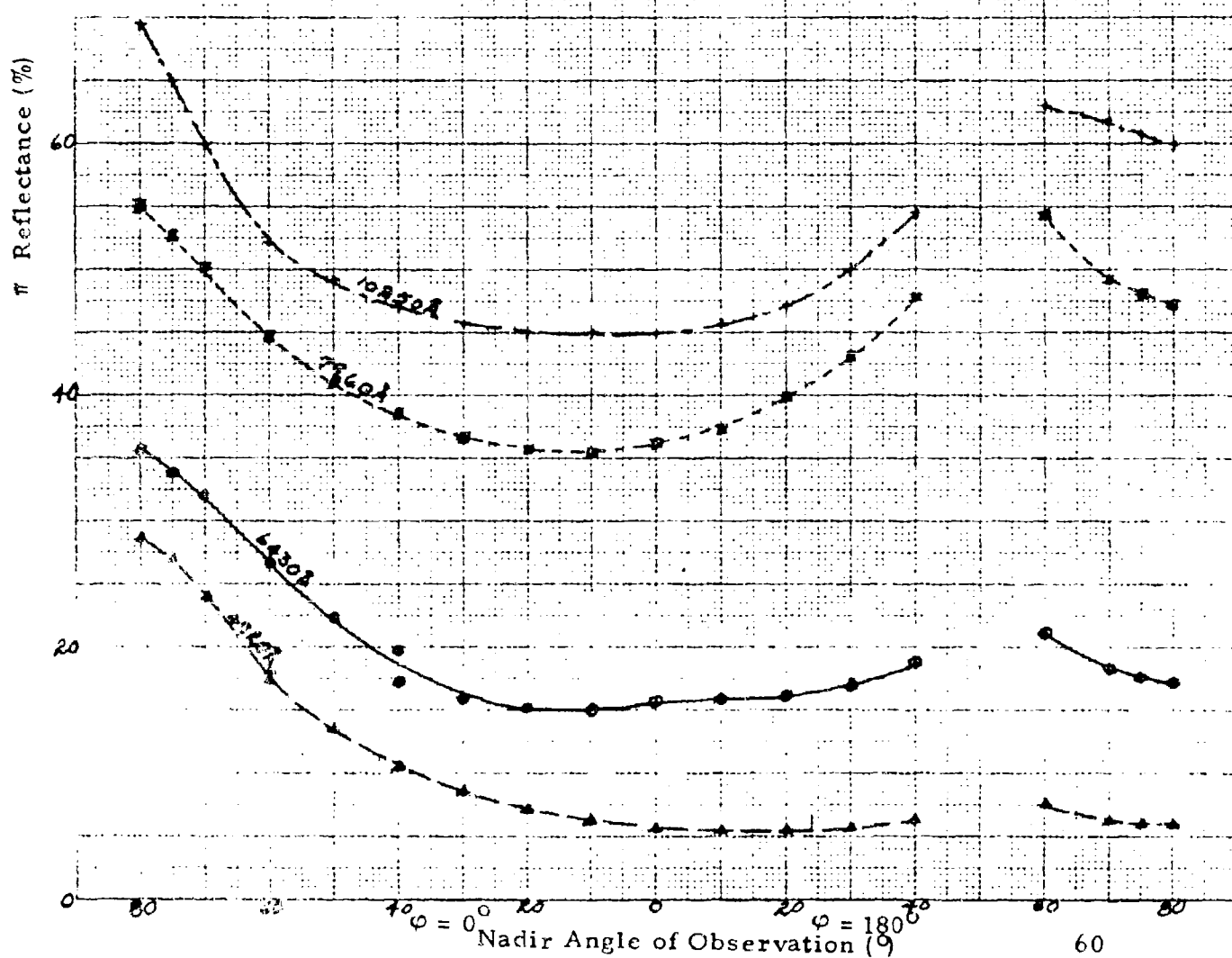


Fig. 42 - Directional reflectance
of dead leaves (principal plane,
 $\theta_0 = 53.1^\circ$)



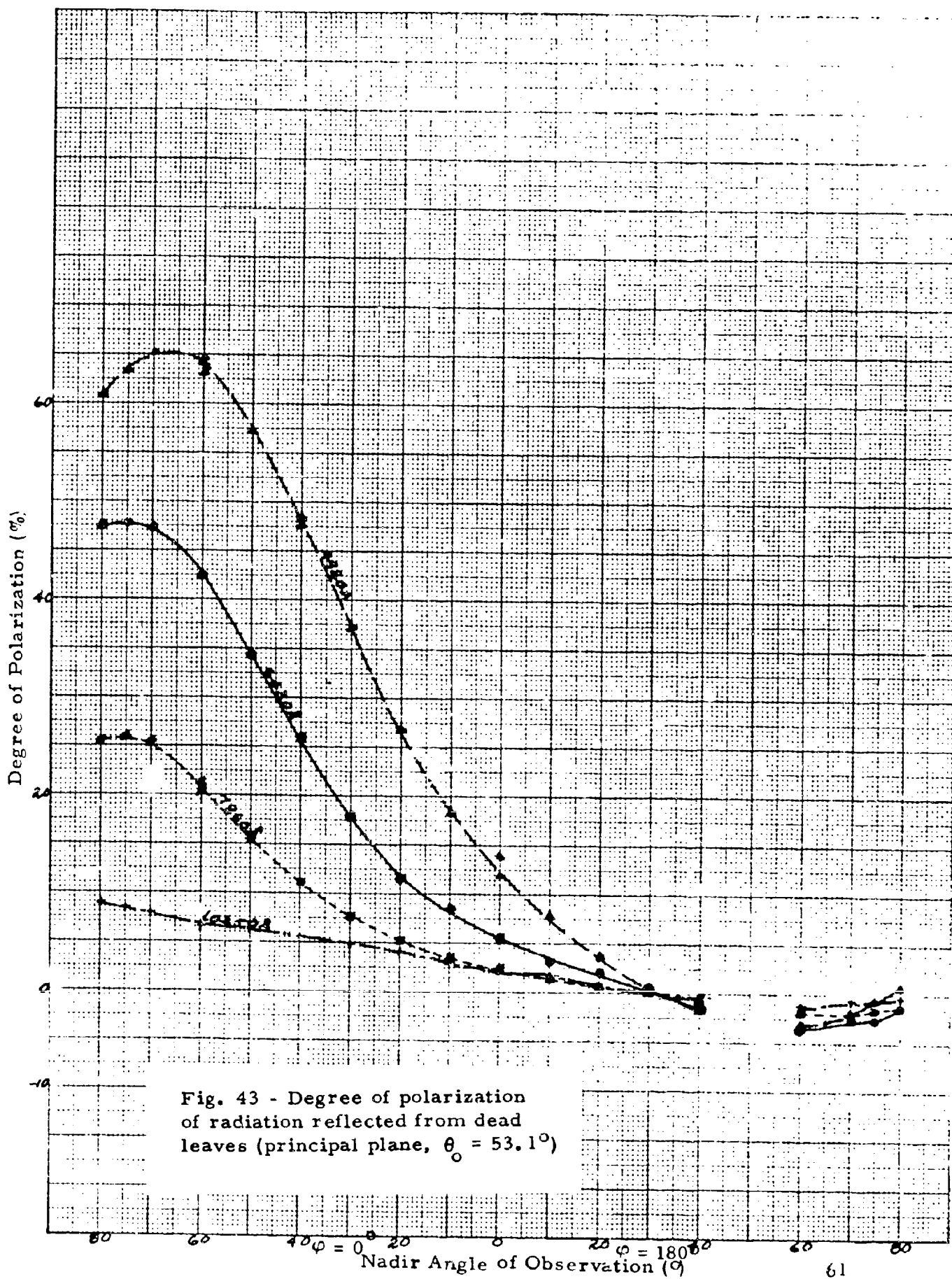
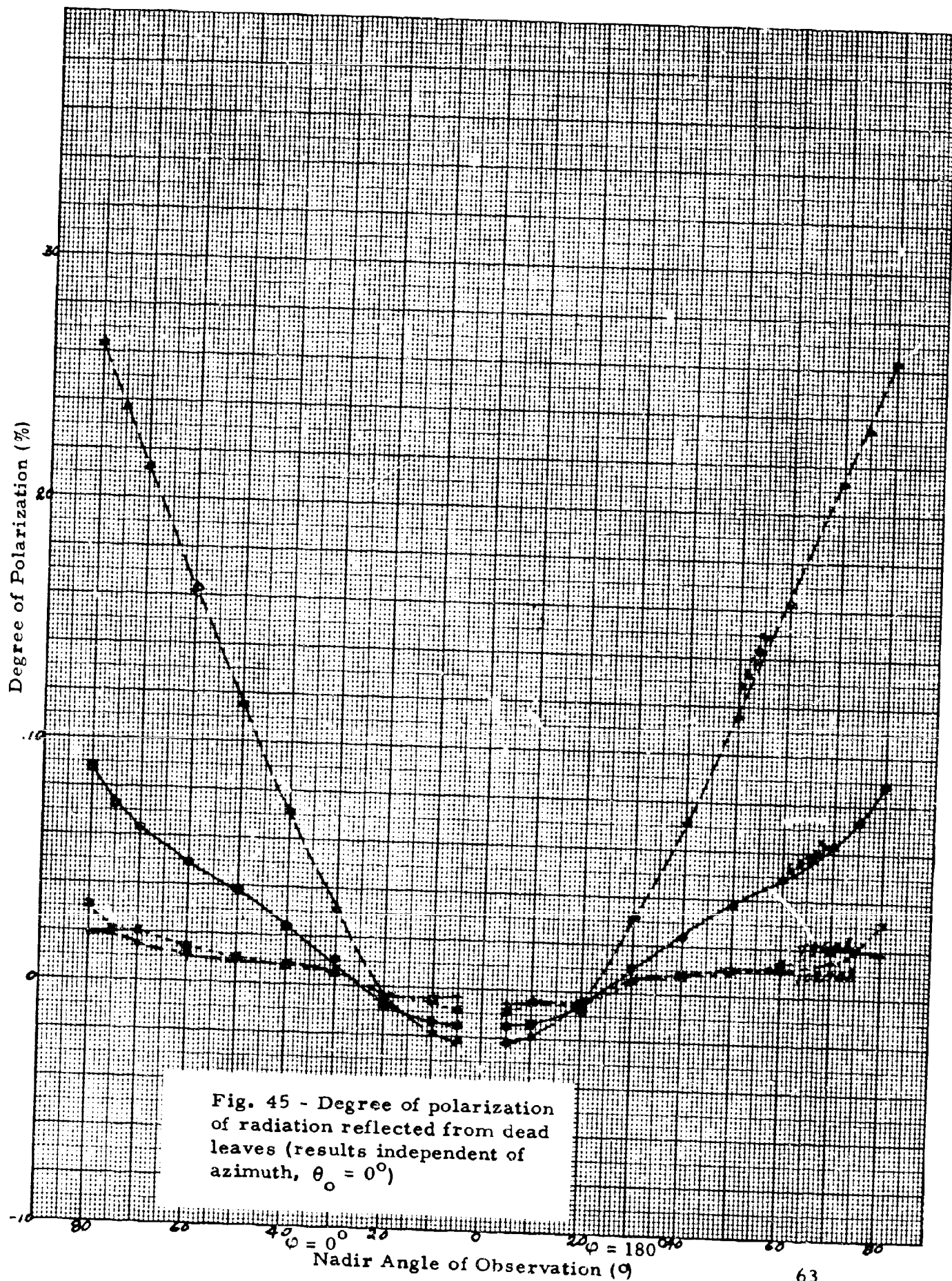


Fig. 43 - Degree of polarization of radiation reflected from dead leaves (principal plane, $\theta_0 = 53.1^\circ$)

Fig. 44 - Directional reflectance of dead leaves (results independent of azimuth, $\theta_0 = 0^\circ$)





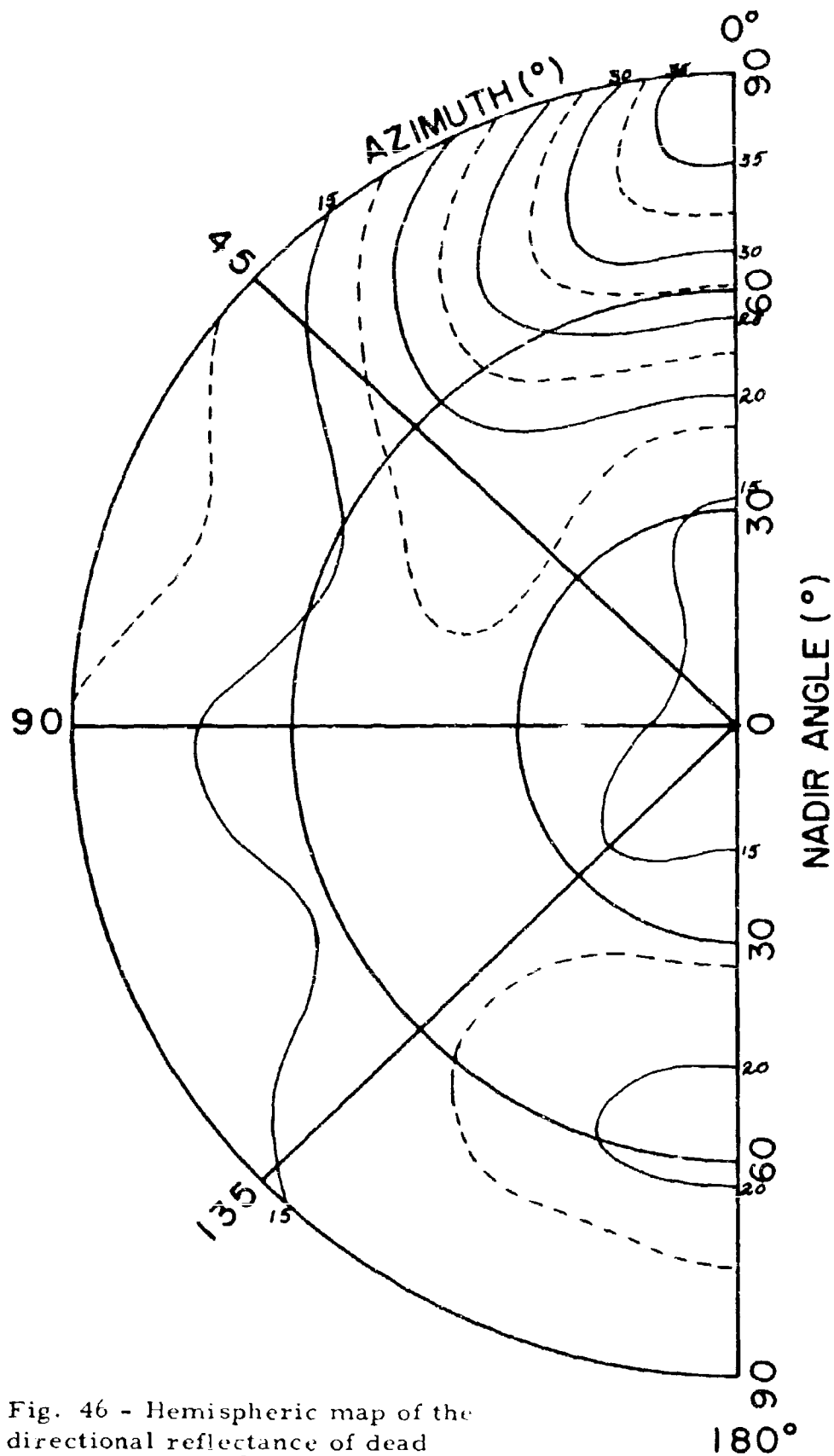


Fig. 46 - Hemispheric map of the directional reflectance of dead leaves ($\theta_0 = 53.1^\circ$, $\lambda = 6430\text{\AA}$)

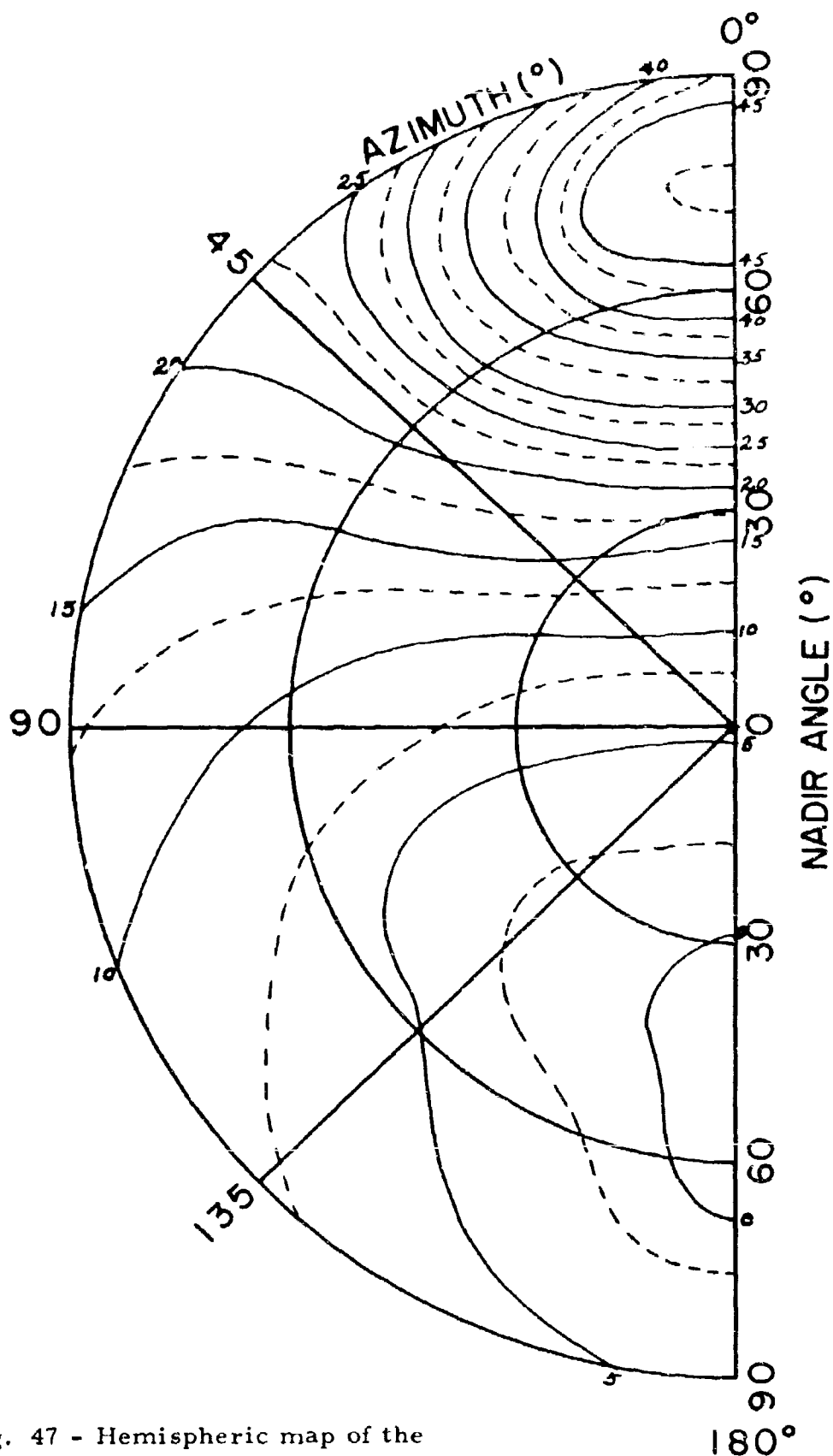
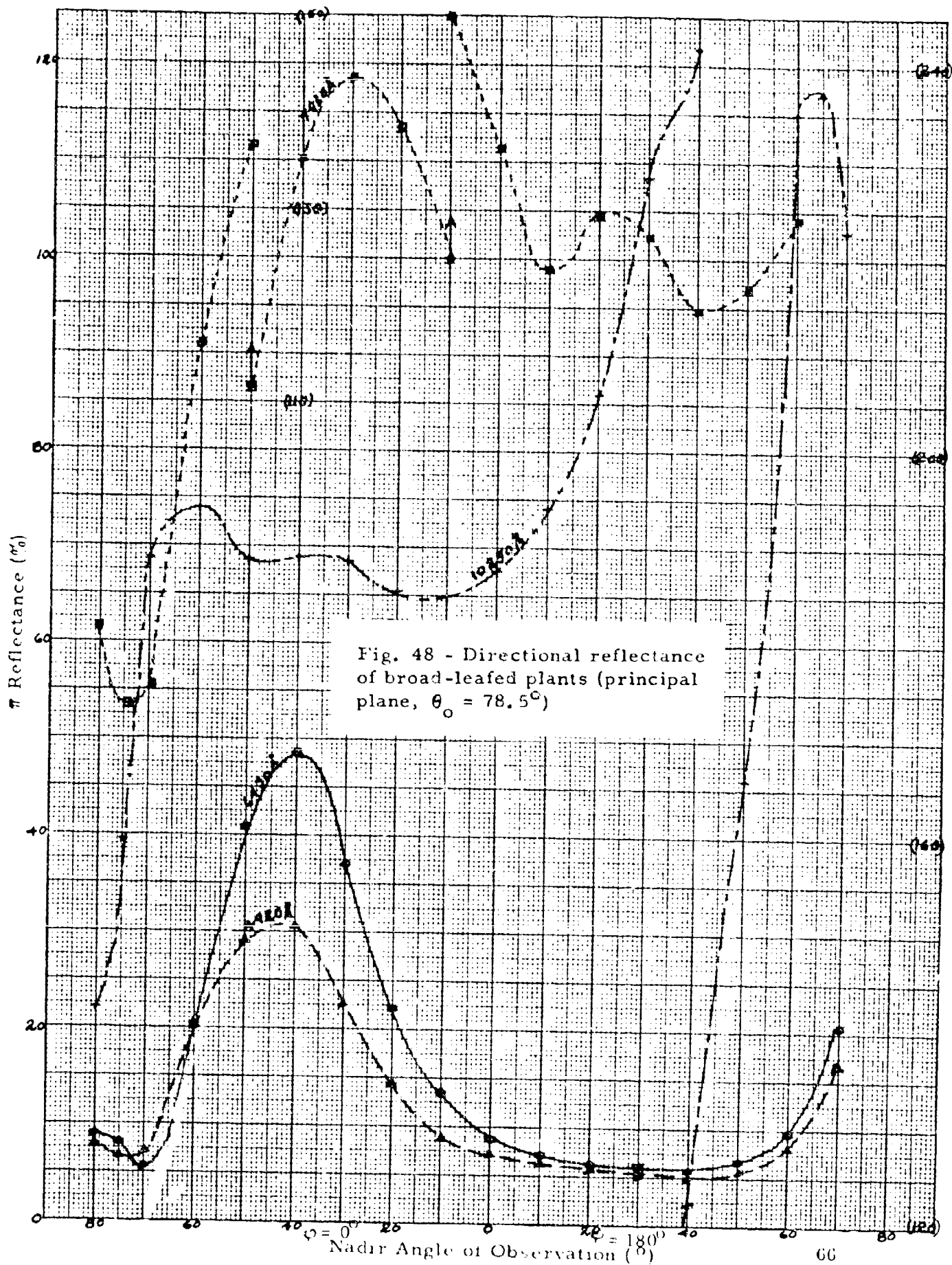


Fig. 47 - Hemispheric map of the degree of polarization of radiation reflected from dead leaves ($\theta_0 = 53.1^\circ$, $\lambda = 6430\text{\AA}$)



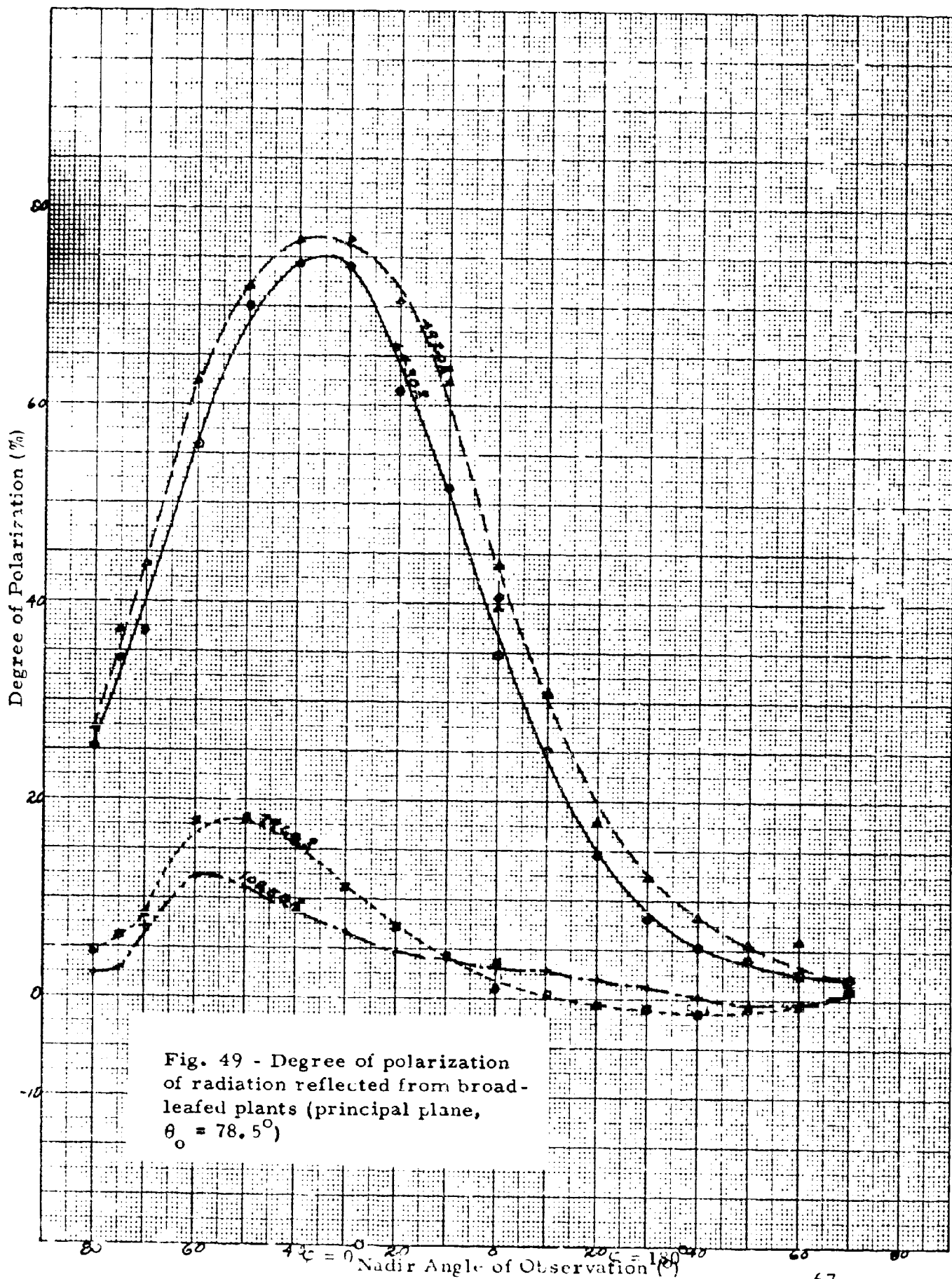


Fig. 50 - Directional reflectance of broad-leaved plants (principal plane, $\theta_0 = 53.1^\circ$)

Fig. 51 - Degree of polarization of radiation reflected from broad-leaved plants (principal plane, $\theta_0 = 53.1^\circ$)

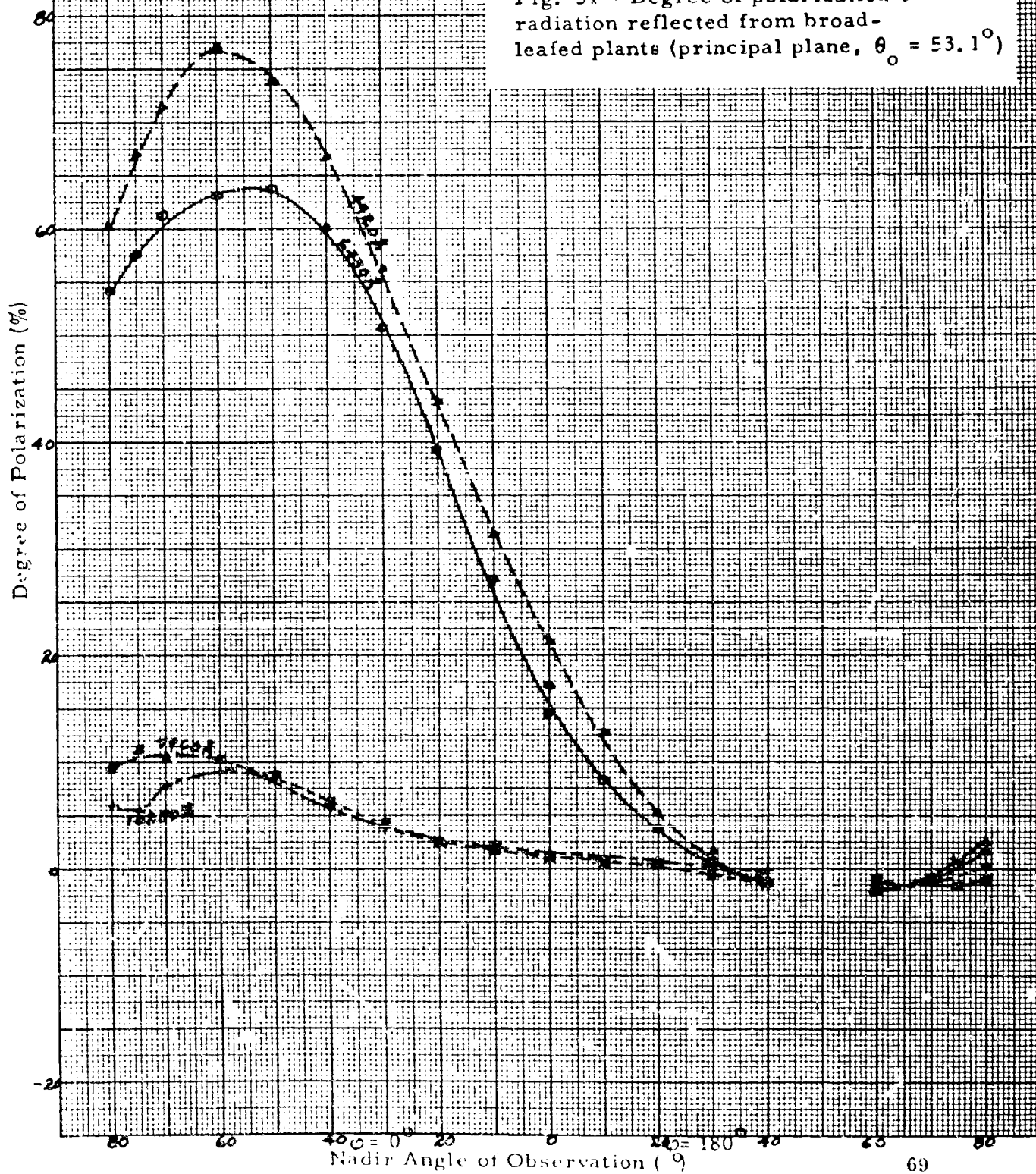
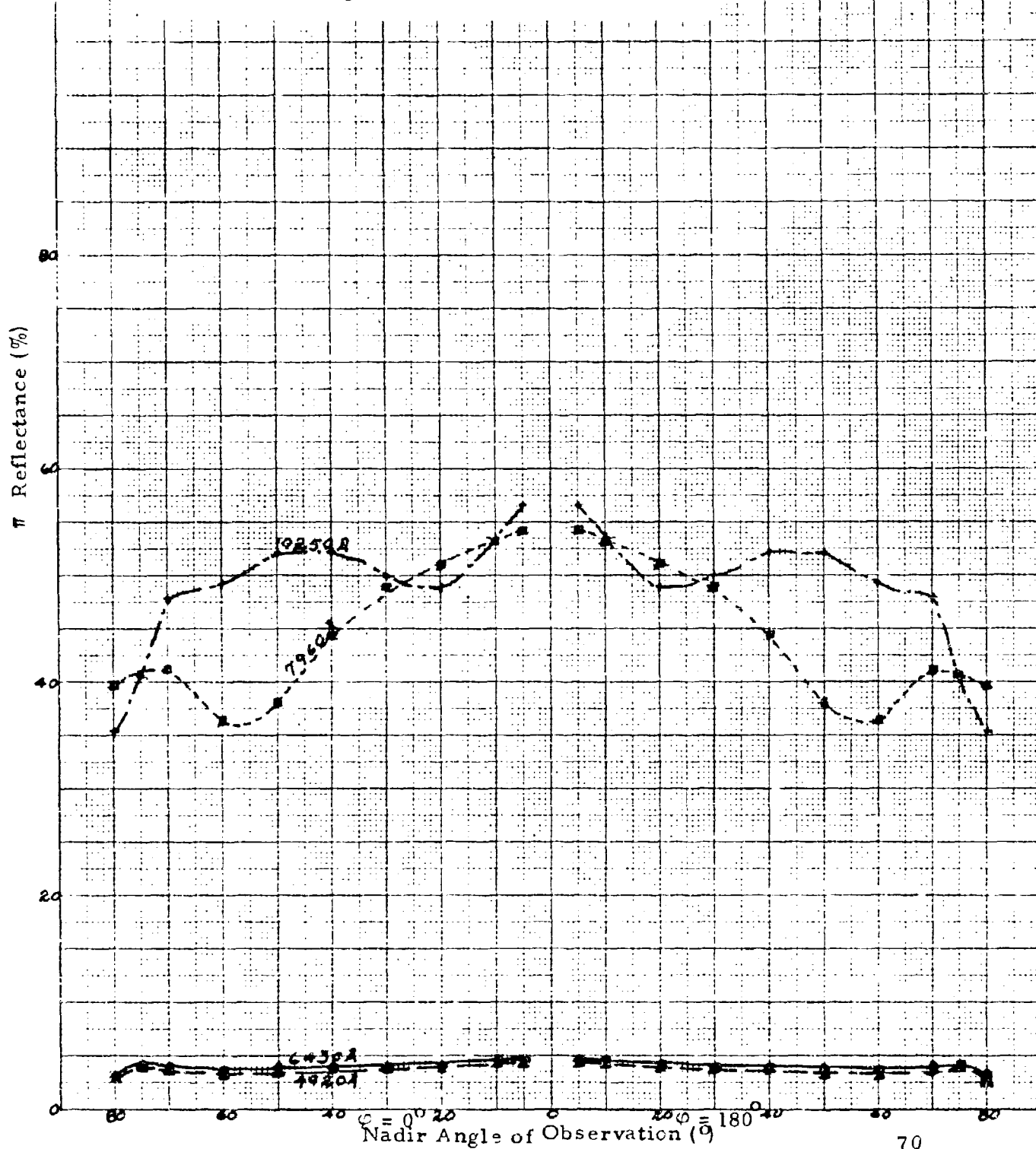


Fig. 52 - Directional reflectance
of broad-leaved plants (results independent
of azimuth, $\theta_0 = 0^\circ$)



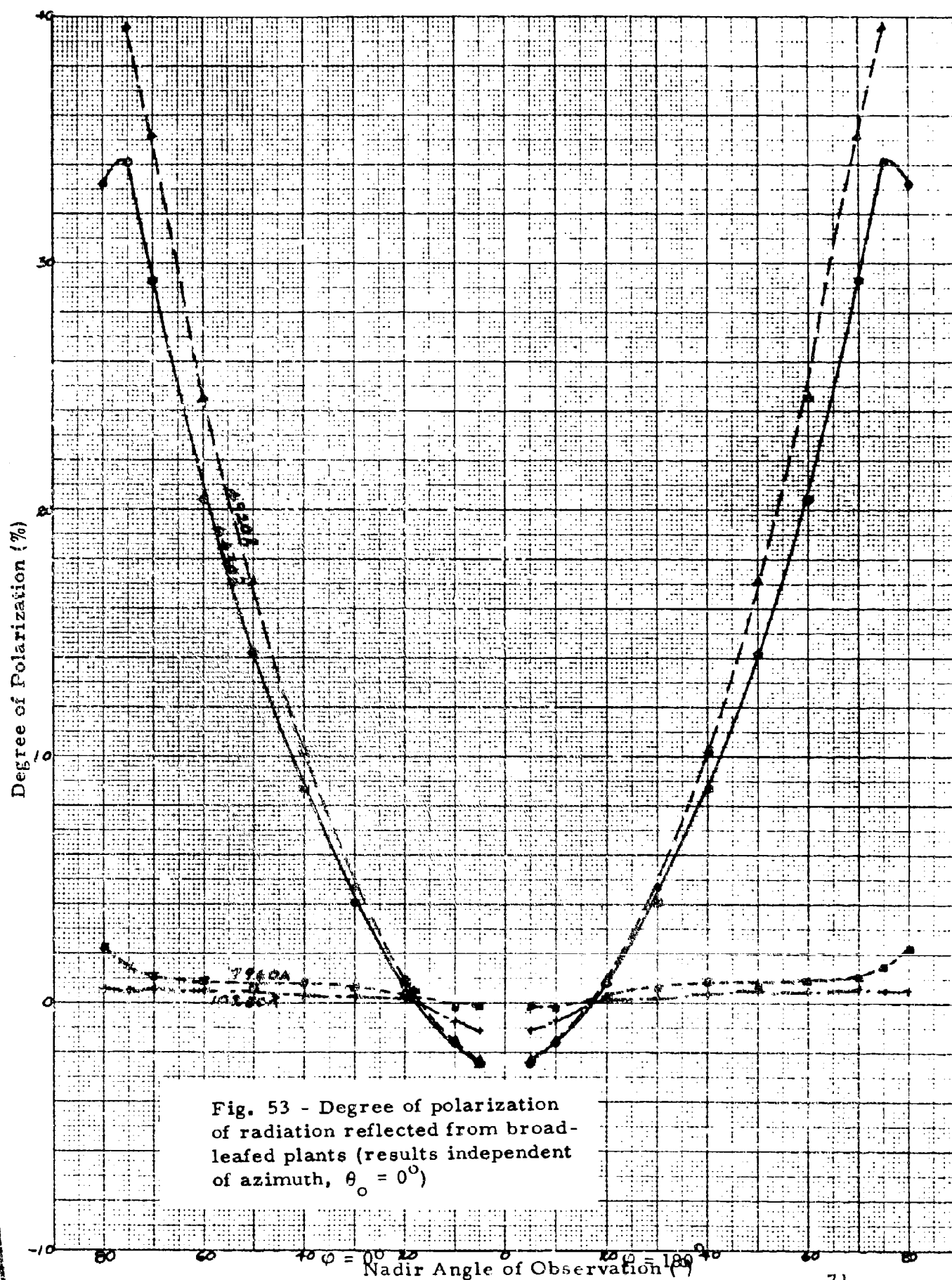


Fig. 53 - Degree of polarization of radiation reflected from broad-leaved plants (results independent of azimuth, $\theta_o = 0^\circ$)

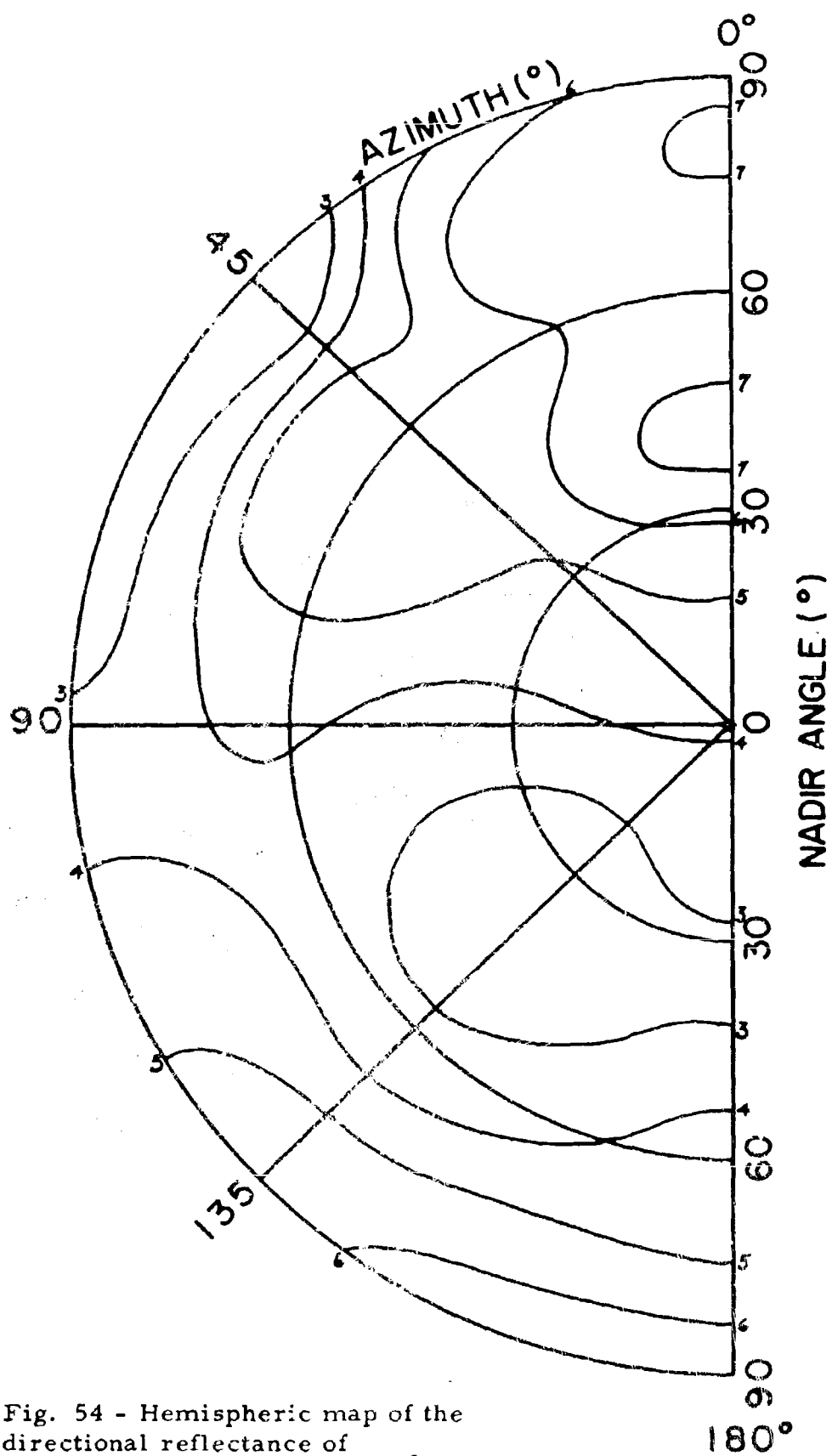


Fig. 54 - Hemispheric map of the directional reflectance of broad-leaved plants ($\theta_o = 53.1^\circ$, $\lambda = 6430\text{\AA}$)

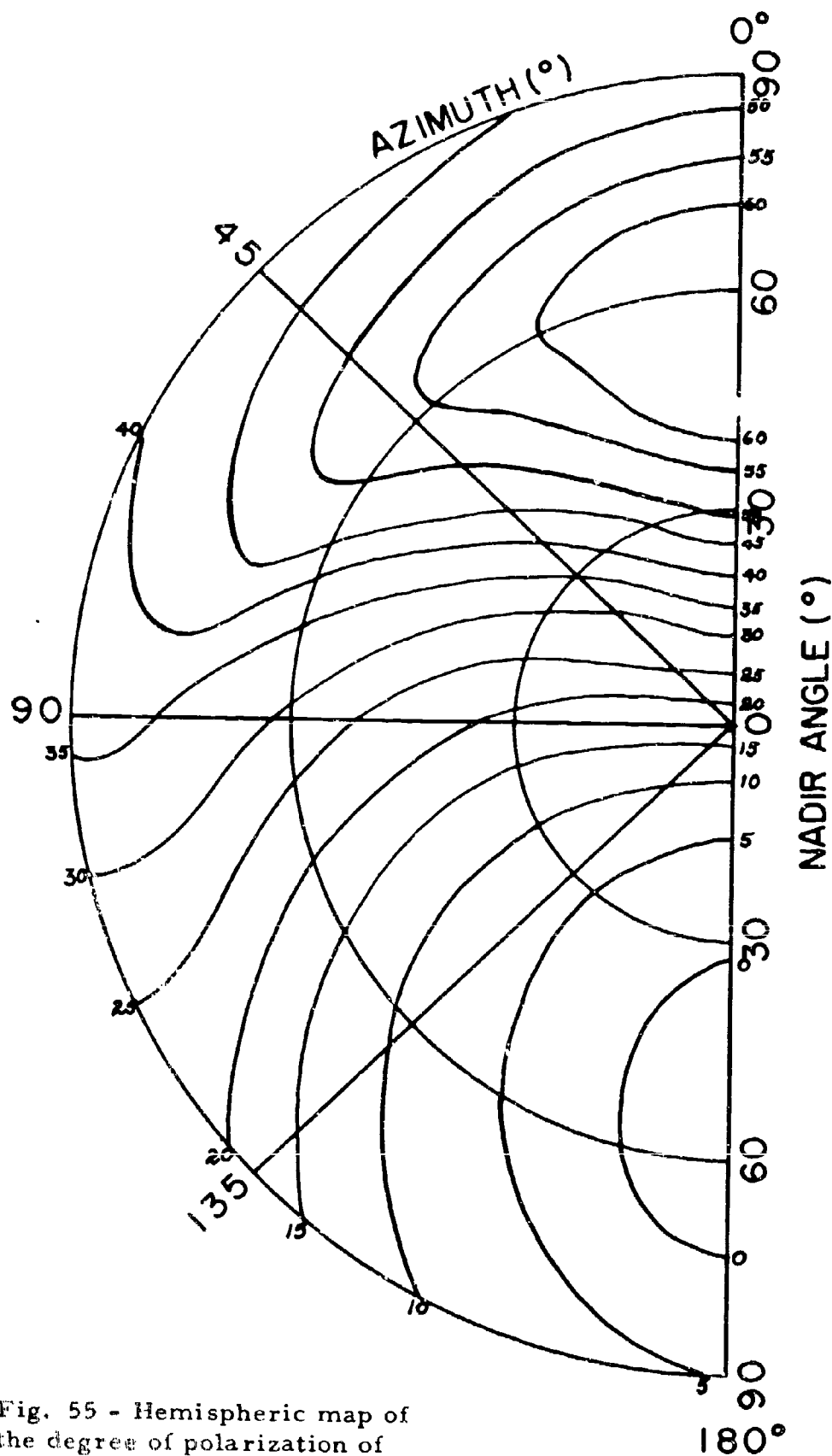


Fig. 55 - Hemispheric map of the degree of polarization of radiation reflected from broad-leaved plants \circ ($\theta_0 = 53.1^\circ$, $\lambda = 6430\text{\AA}$)

Fig. 56 - Directional reflectance
of crushed limestone (principal
plane, $\theta_0 = 78.5^\circ$)

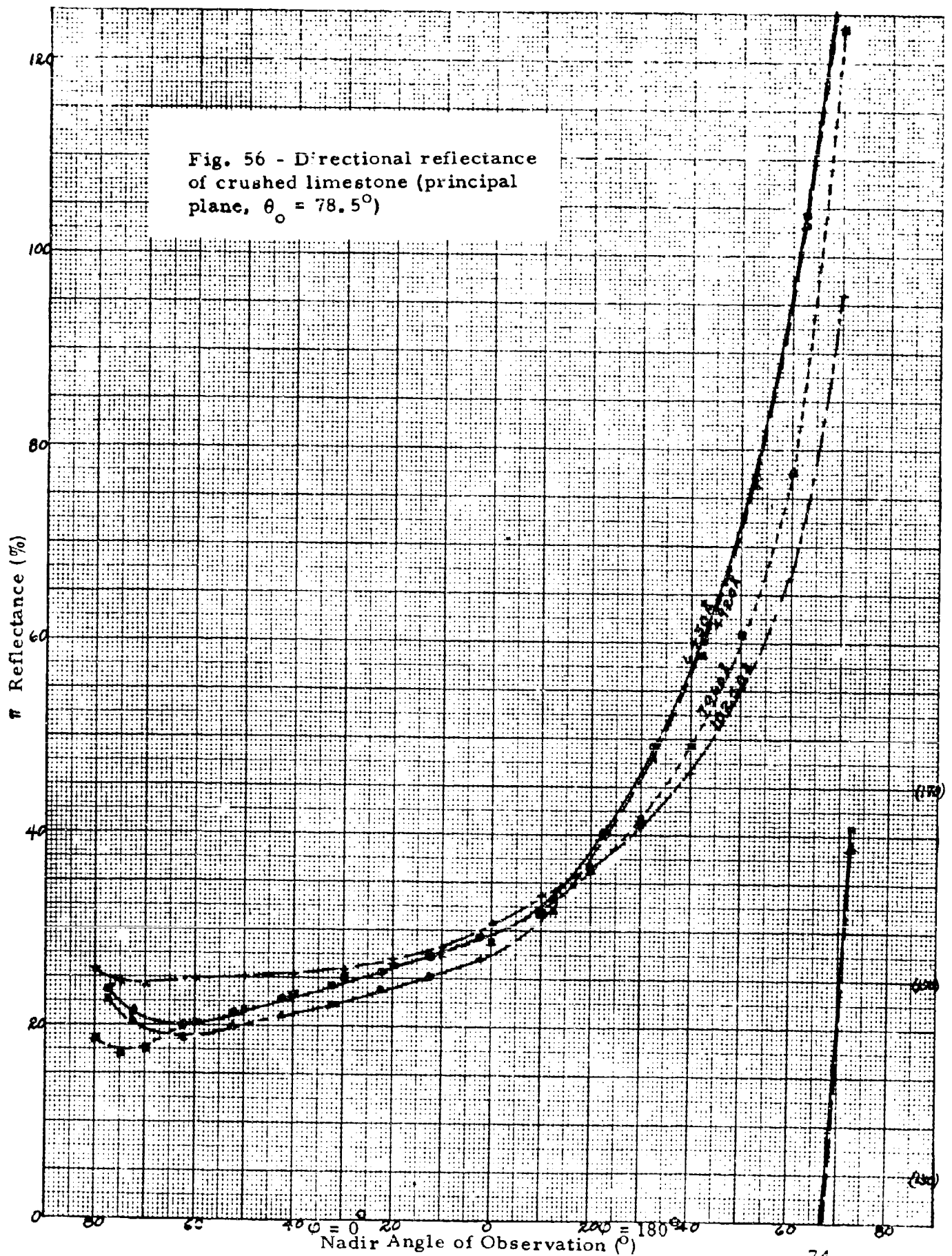


Fig. 57 - Degree of polarization of radiation reflected from crushed limestone (principal plane, $\theta_0 = 78.5^\circ$)

Degree of Polarization (%)

10

5

0

-5

Nadir Angle of Observation ($^\circ$)

75

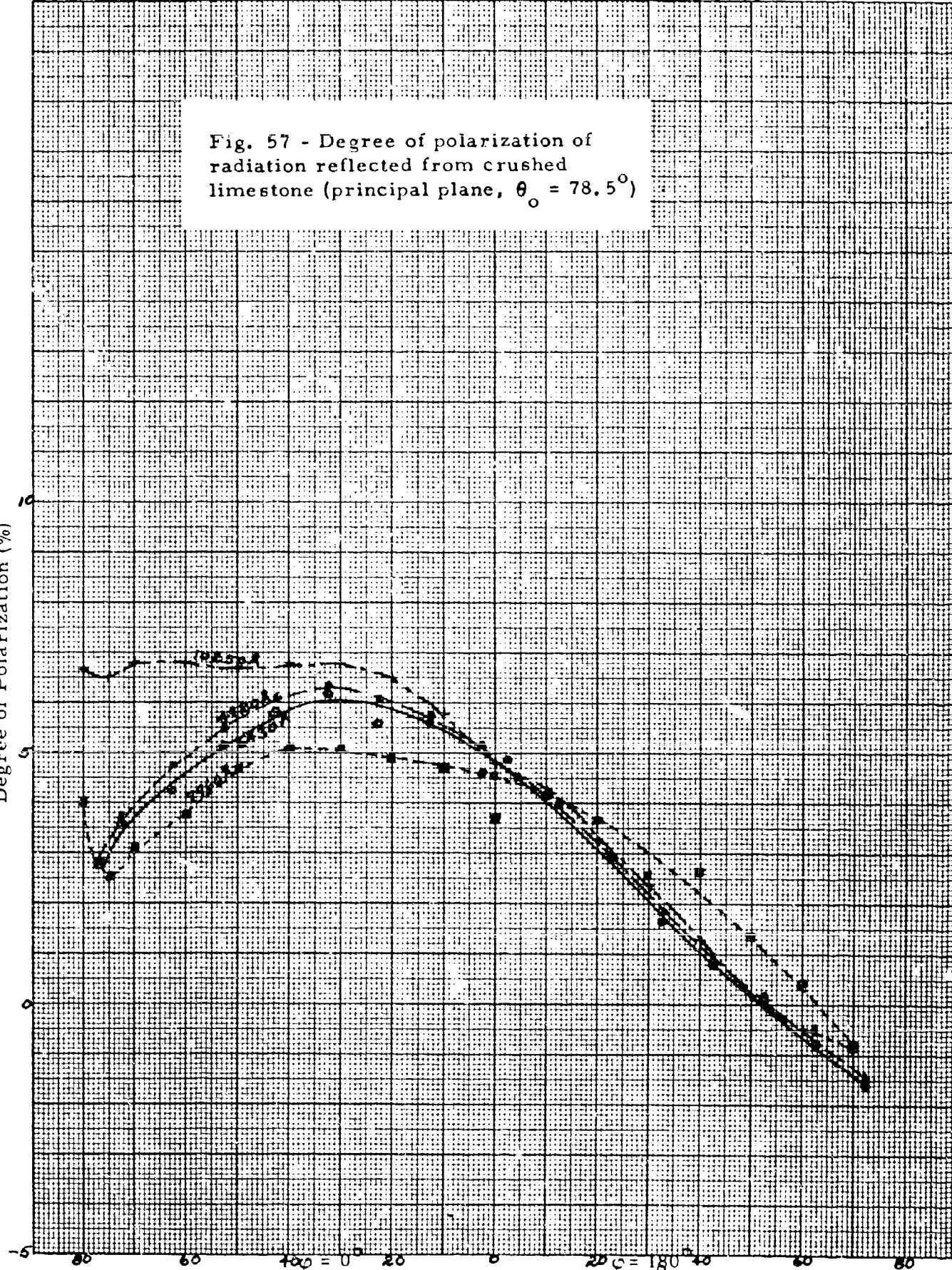


Fig. 58 - Directional reflectance
of crushed limestone (principal
plane, $\theta_o = 53.1^\circ$)

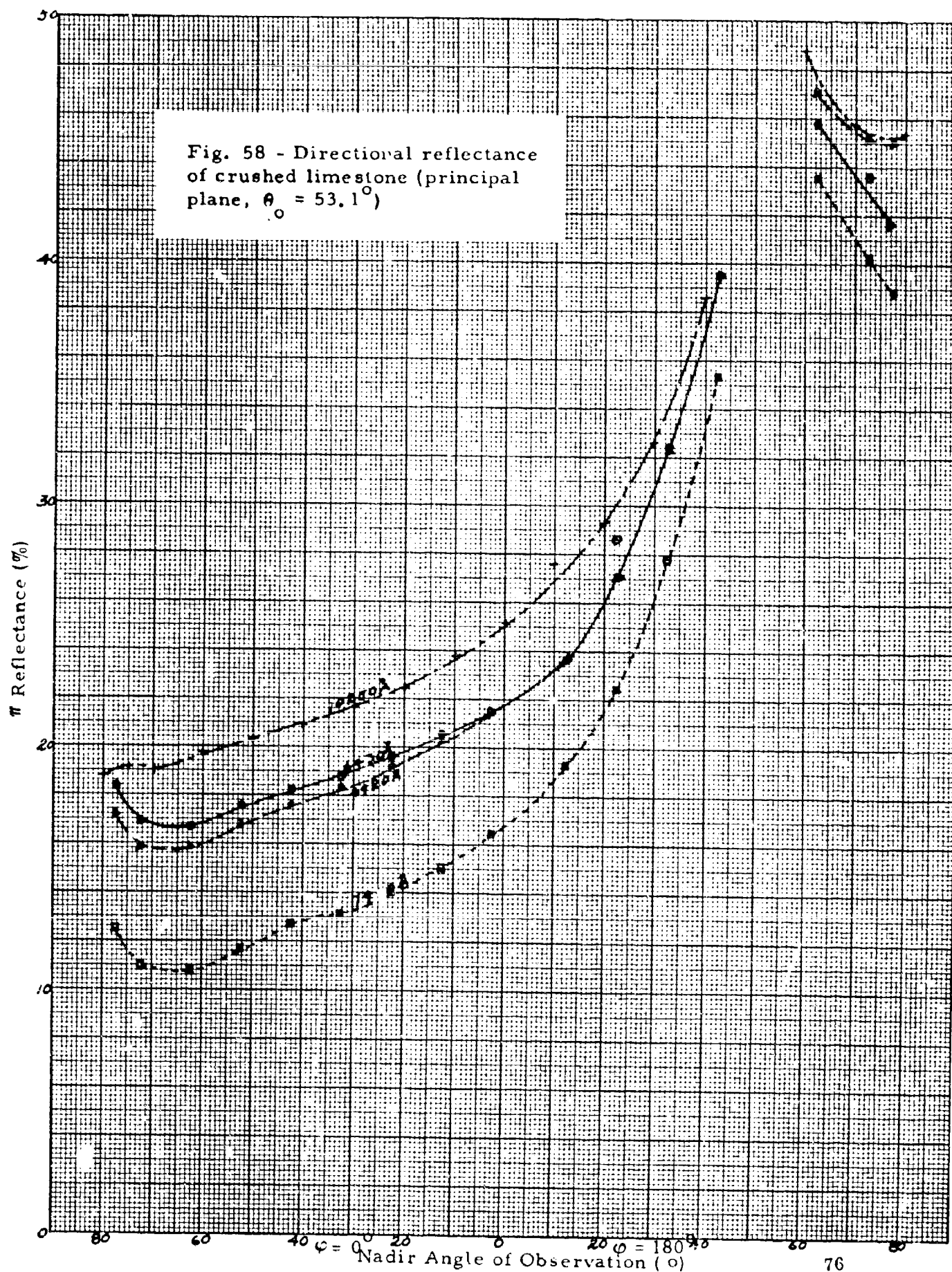
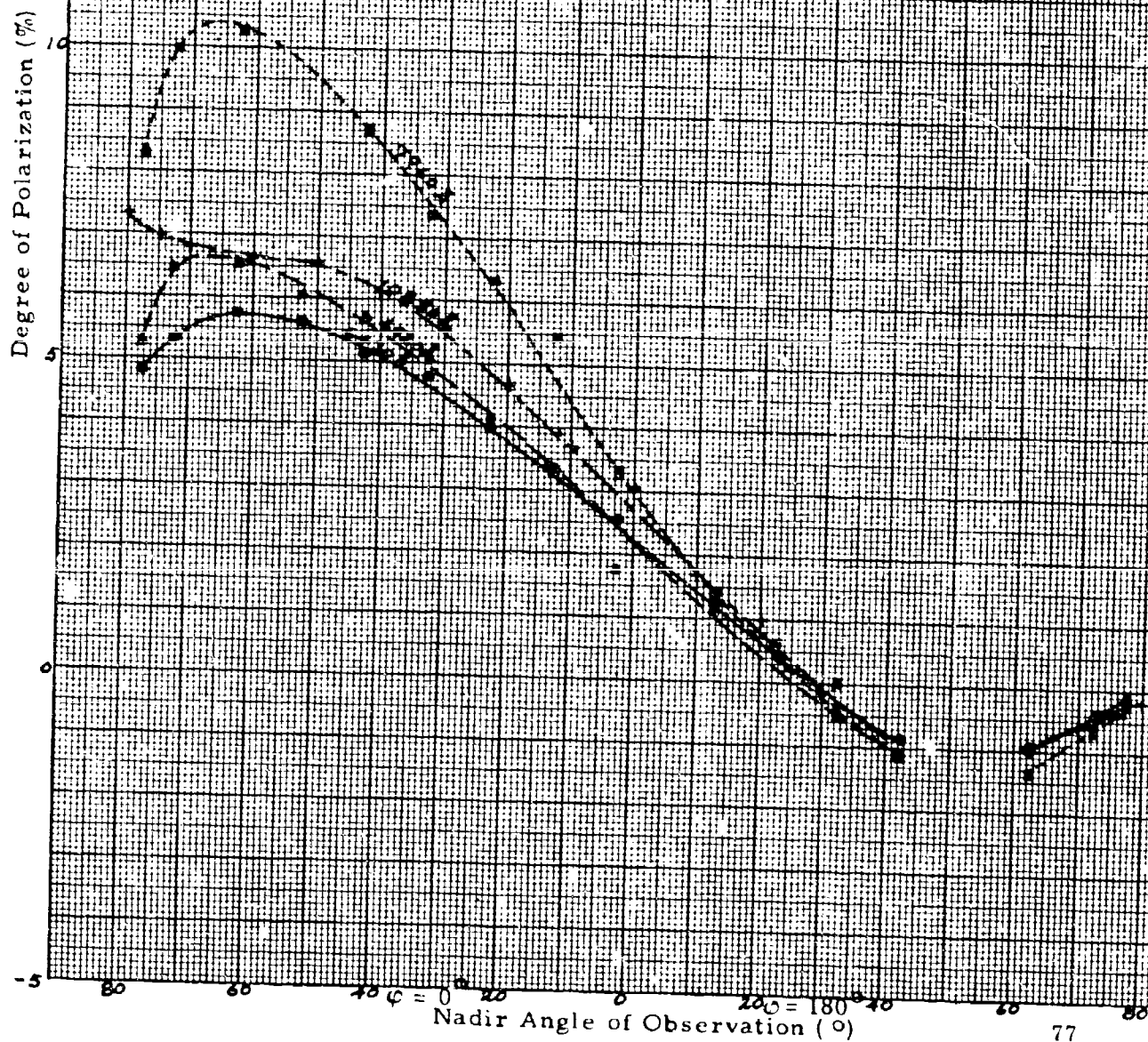


Fig. 59 - Degree of polarization
of radiation reflected from
crushed limestone (principal
plane $\theta_0 = 53.1^\circ$)



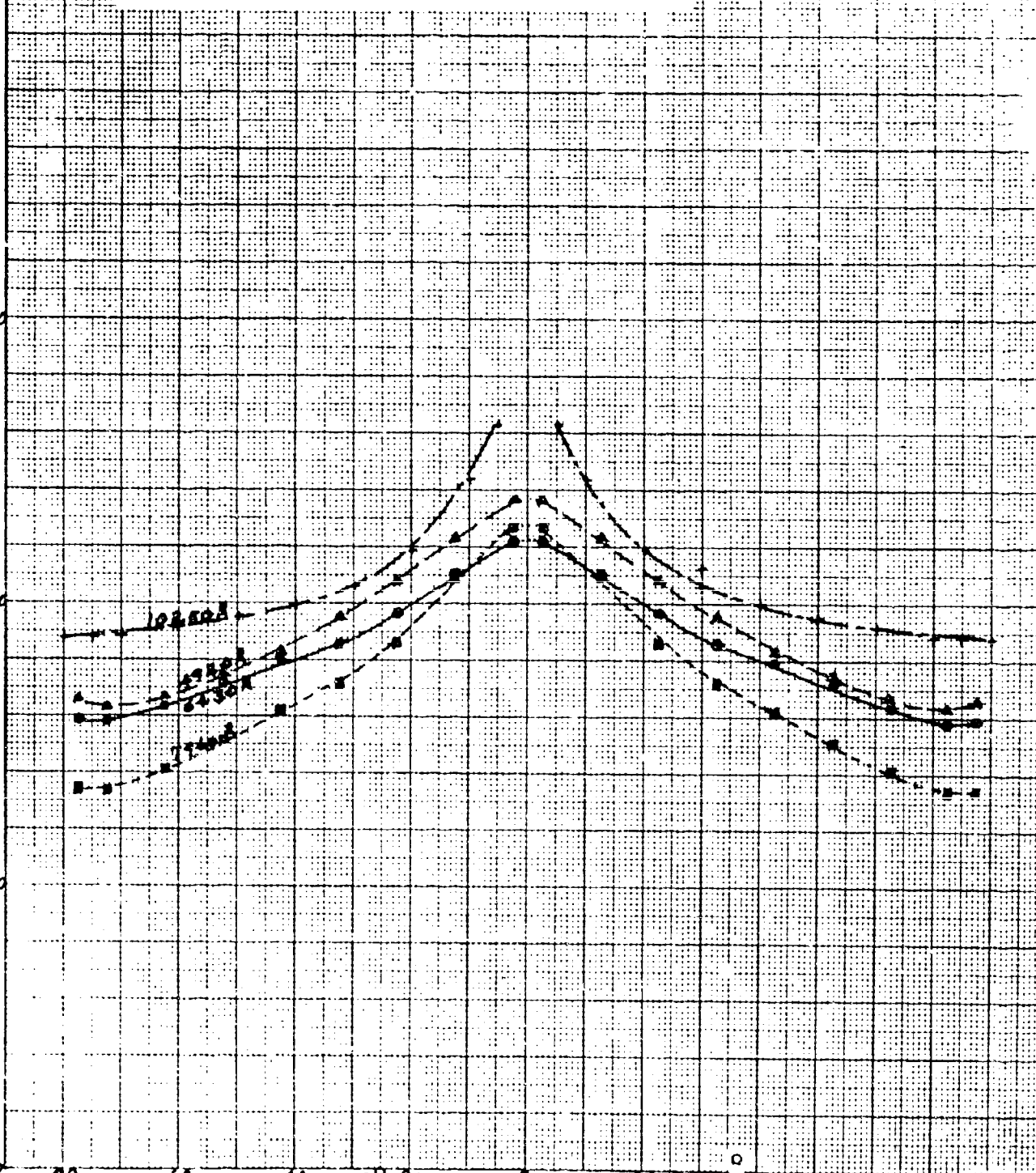
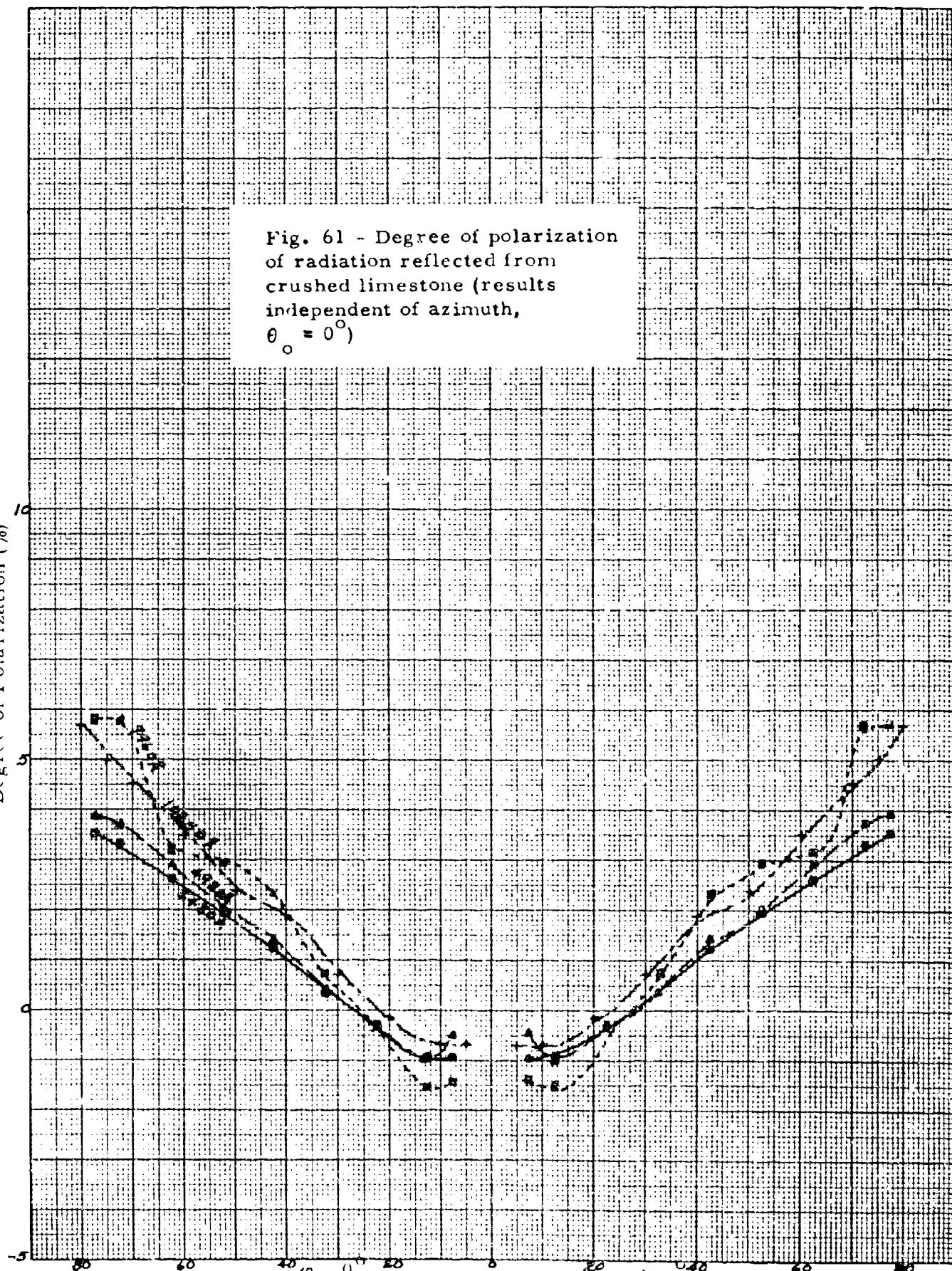
[illegible]

Fig. 61 - Degree of polarization
of radiation reflected from
crushed limestone (results
independent of azimuth,
 $\theta_o = 0^\circ$)

Degree of Polarization (%)

Nadir Angle of Observation ($^\circ$)



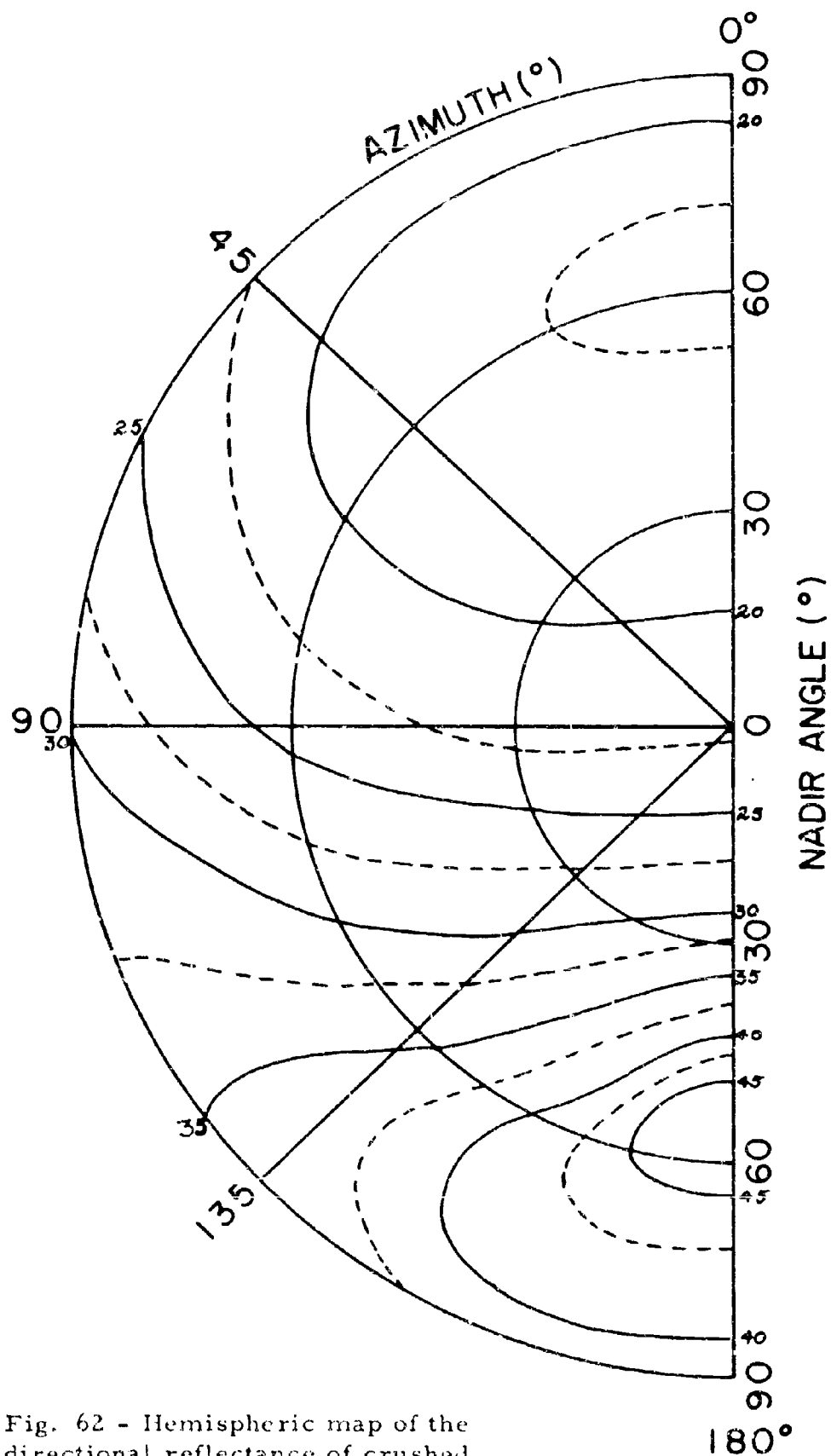


Fig. 62 - Hemispheric map of the directional reflectance of crushed limestone gravel ($\theta_0 = 53.1^\circ$, $\lambda = 6430\text{\AA}$)

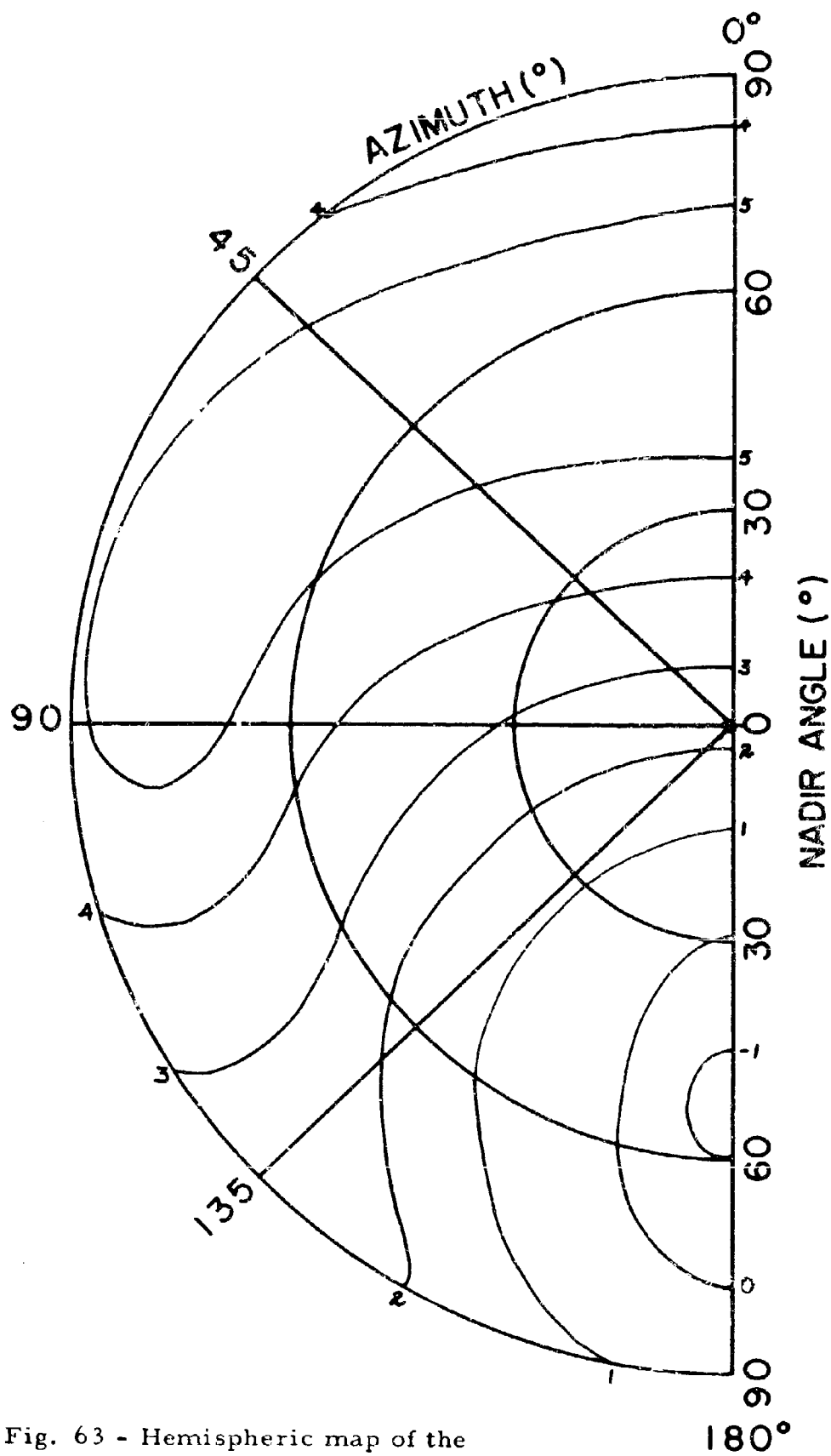


Fig. 63 - Hemispheric map of the degree of polarization of radiation reflected from crushed limestone gravel ($\theta_0 = 53.1^\circ$, $\lambda = 6430\text{\AA}$)

8. Blacktop (Asphalt) Road Surface

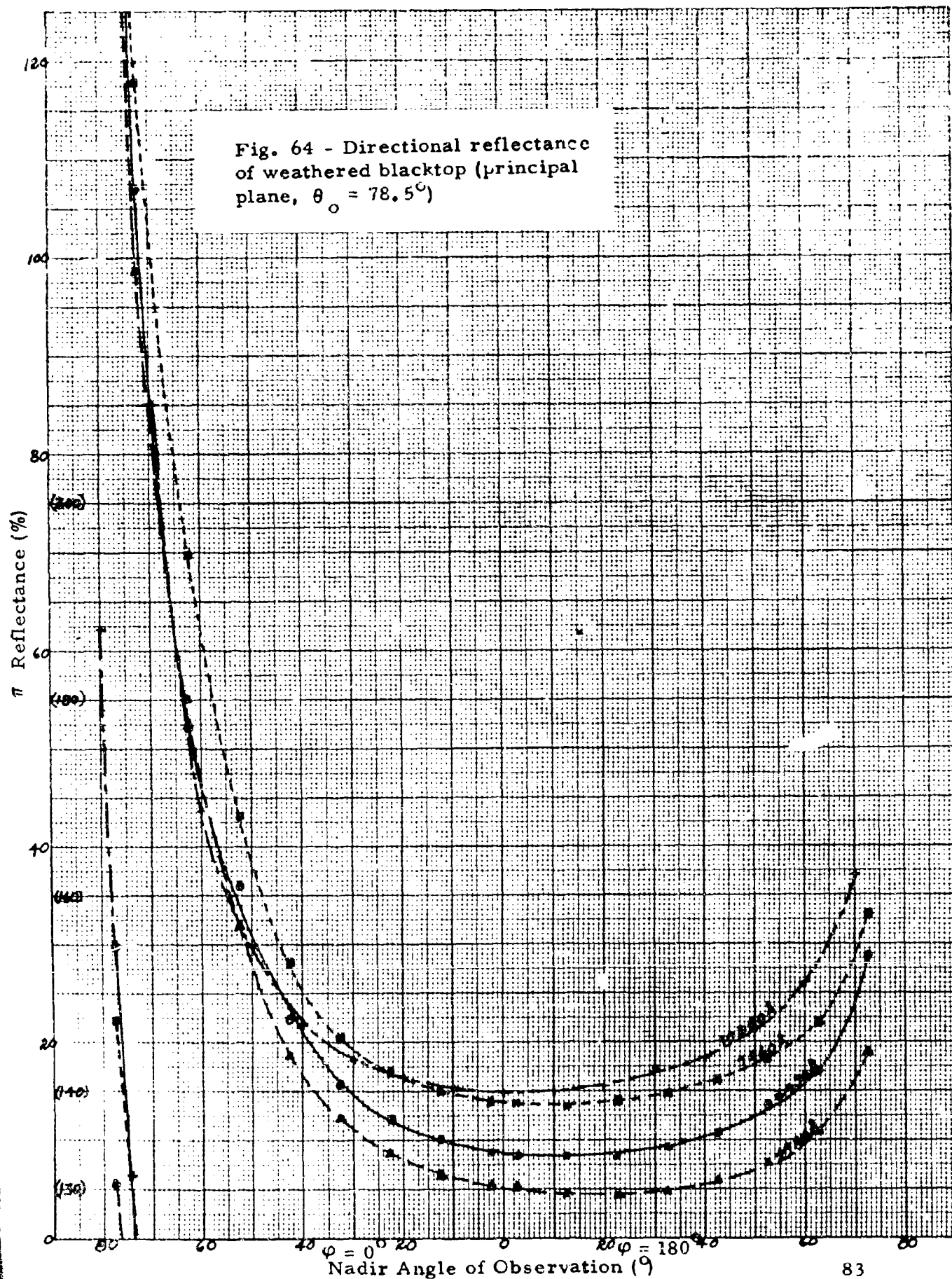
The sample of blacktop used for these measurements was obtained, through the cooperation of the Pennsylvania Highway Department, from a reconstruction operation on Paper Mill Road in Oreland, a suburb of Philadelphia. The road has fairly heavy traffic but since there was no painted centerline there were no preferred strips of tire wear along the roadway. The sample surface is not particularly smooth, asphalt covered pebbles protruding as much as one eighth to three sixteenths inches above the general level of the surface. There was no definite information available on the length of time the road surface had been in place, but it was "several years".

9. Concrete

The sample of concrete for which the measurements were made was obtained from Wayne, Pennsylvania. It is a section of well-weathered sidewalk. The general surface is relatively smooth as concrete surfaces run, and some small pebbles of the order of one eighth inch diameter are visible in the matrix.

10. Canvas

The sample of canvas used is that supplied by the Naval Ordnance Test Station, China Lake, California. It appears to be a weathered piece of a standard type of green-colored canvas.



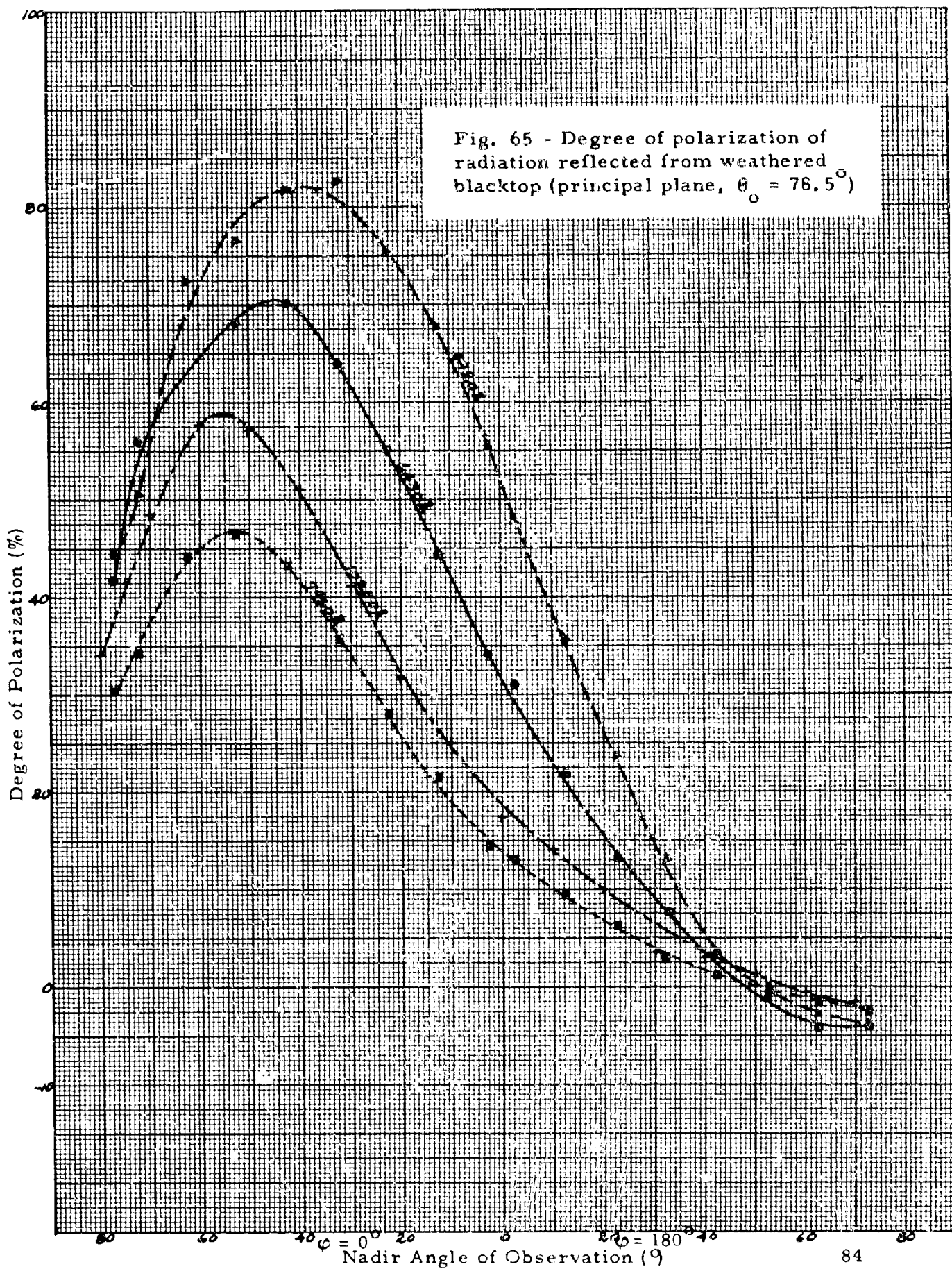
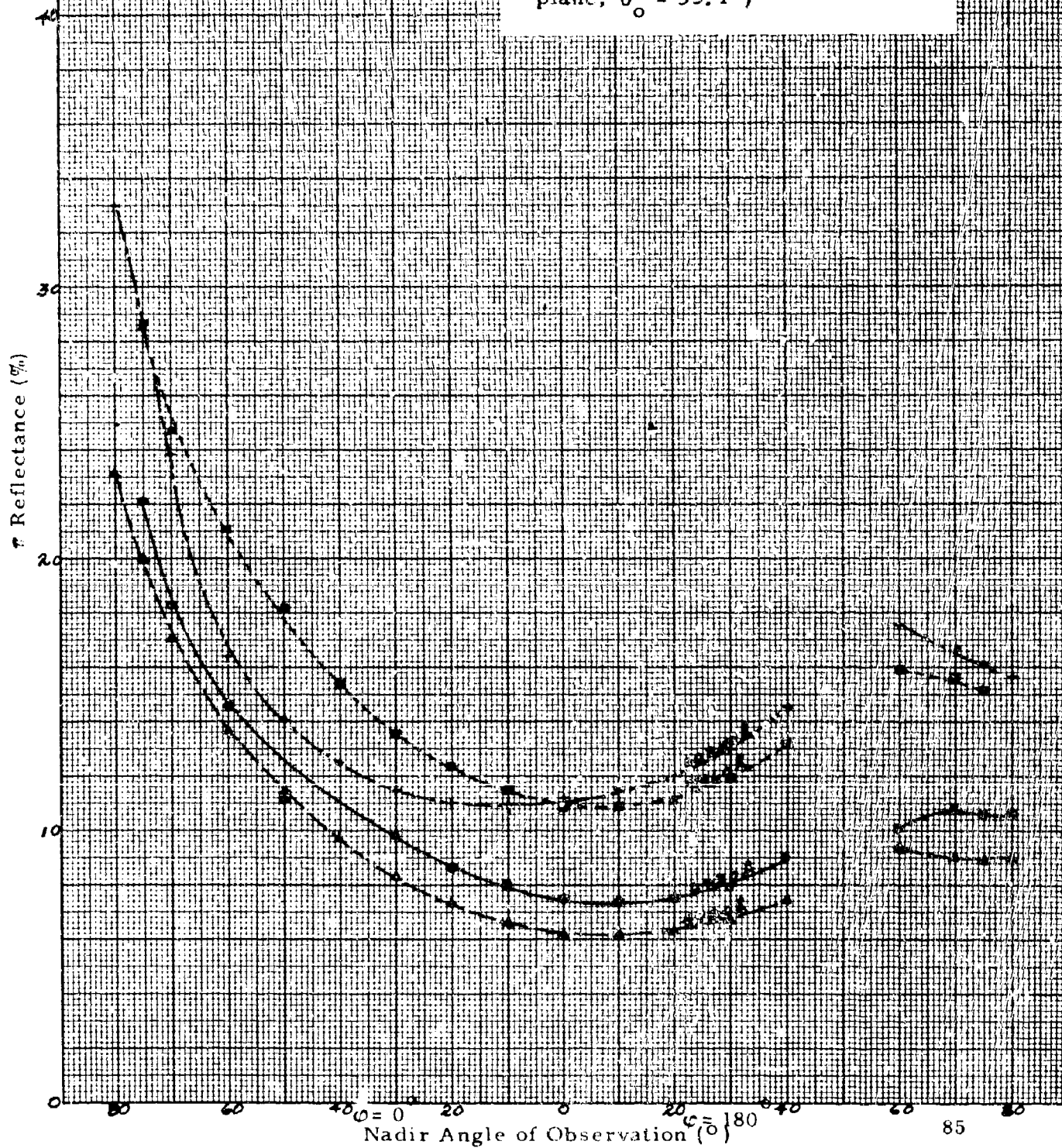


Fig. 66 - Directional reflectance of weathered blacktop (principal plane, $\theta_0 = 53.1^\circ$)



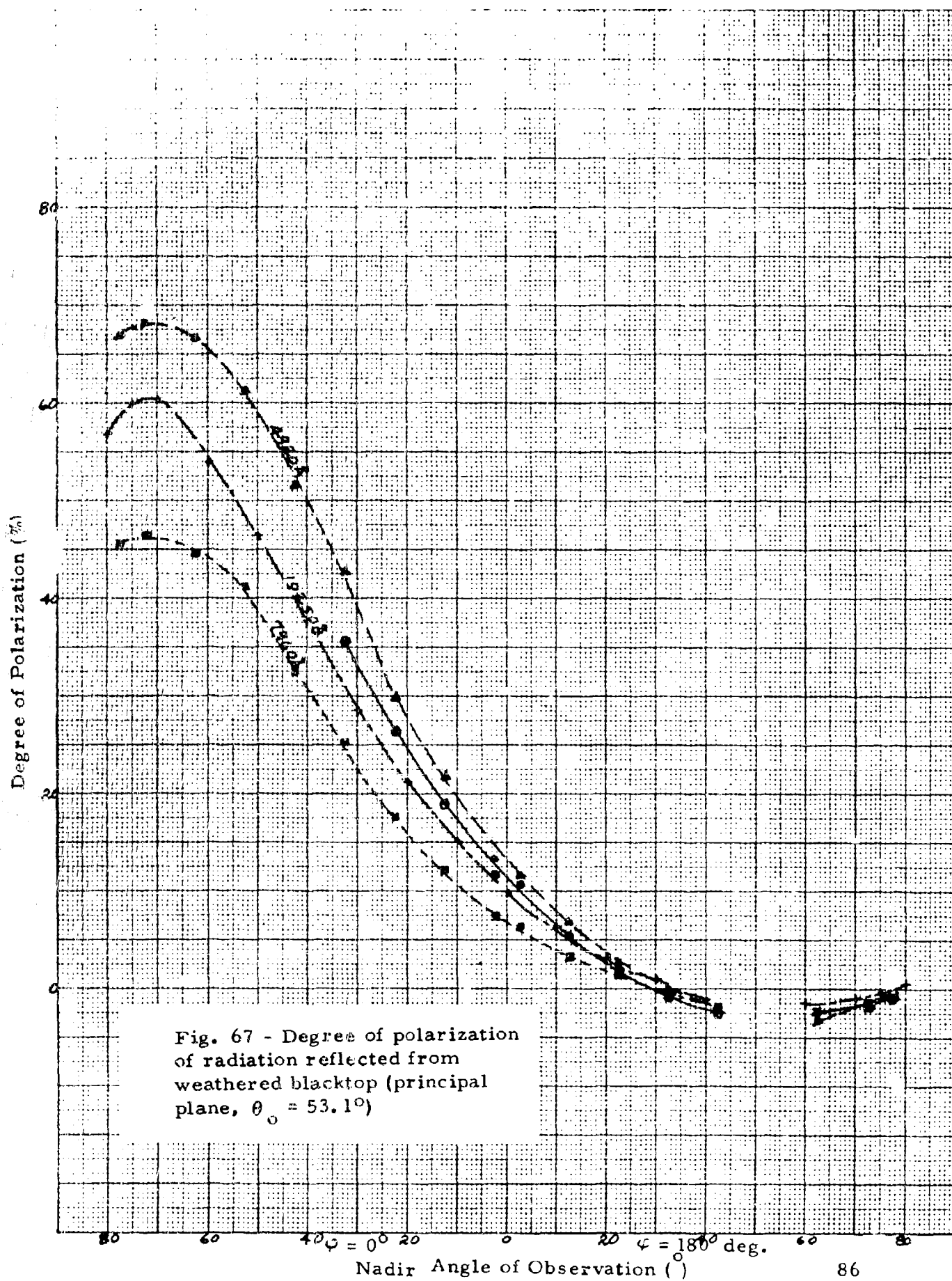


Fig. 67 - Degree of polarization of radiation reflected from weathered blacktop (principal plane, $\theta_0 = 53.1^\circ$)

Fig. 68 - Directional reflectance of weathered blacktop (results independent of azimuth, $\theta_o = 0^\circ$)

π Reflectance (%)

24

10

0

80

60

40

20

0

20

40

60

80

100

180

160

140

120

100

80

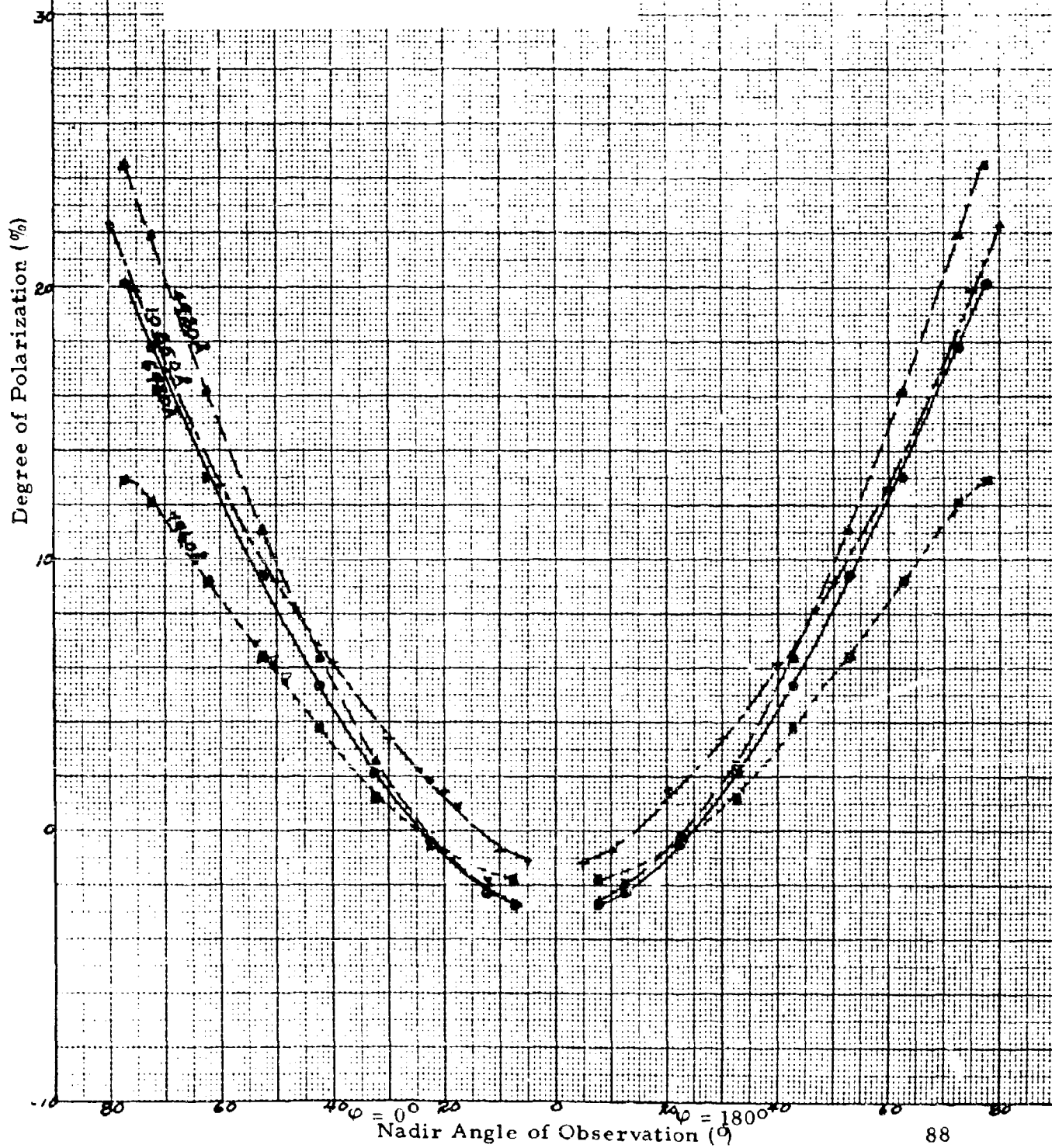
60

40

20

Nadir Angle of Observation ($^\circ$)

Fig. 69 - Degree of polarization
of radiation reflected from
weathered blacktop (results
independent of azimuth, $\theta_0 = 0^\circ$)



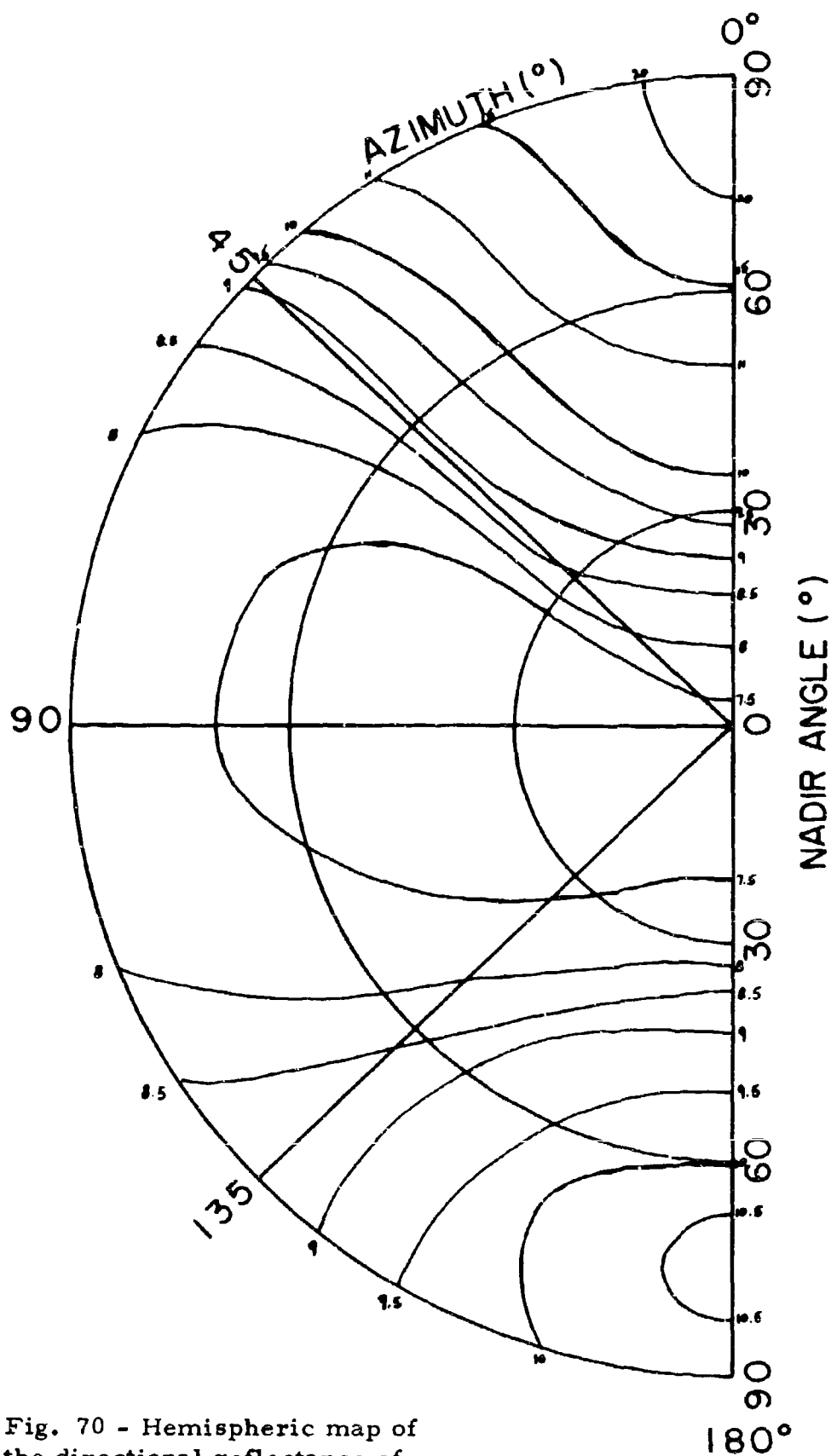


Fig. 70 - Hemispheric map of the directional reflectance of weathered blacktop ($\theta_0 = 53.1^\circ$, $\lambda = 6430\text{\AA}$)

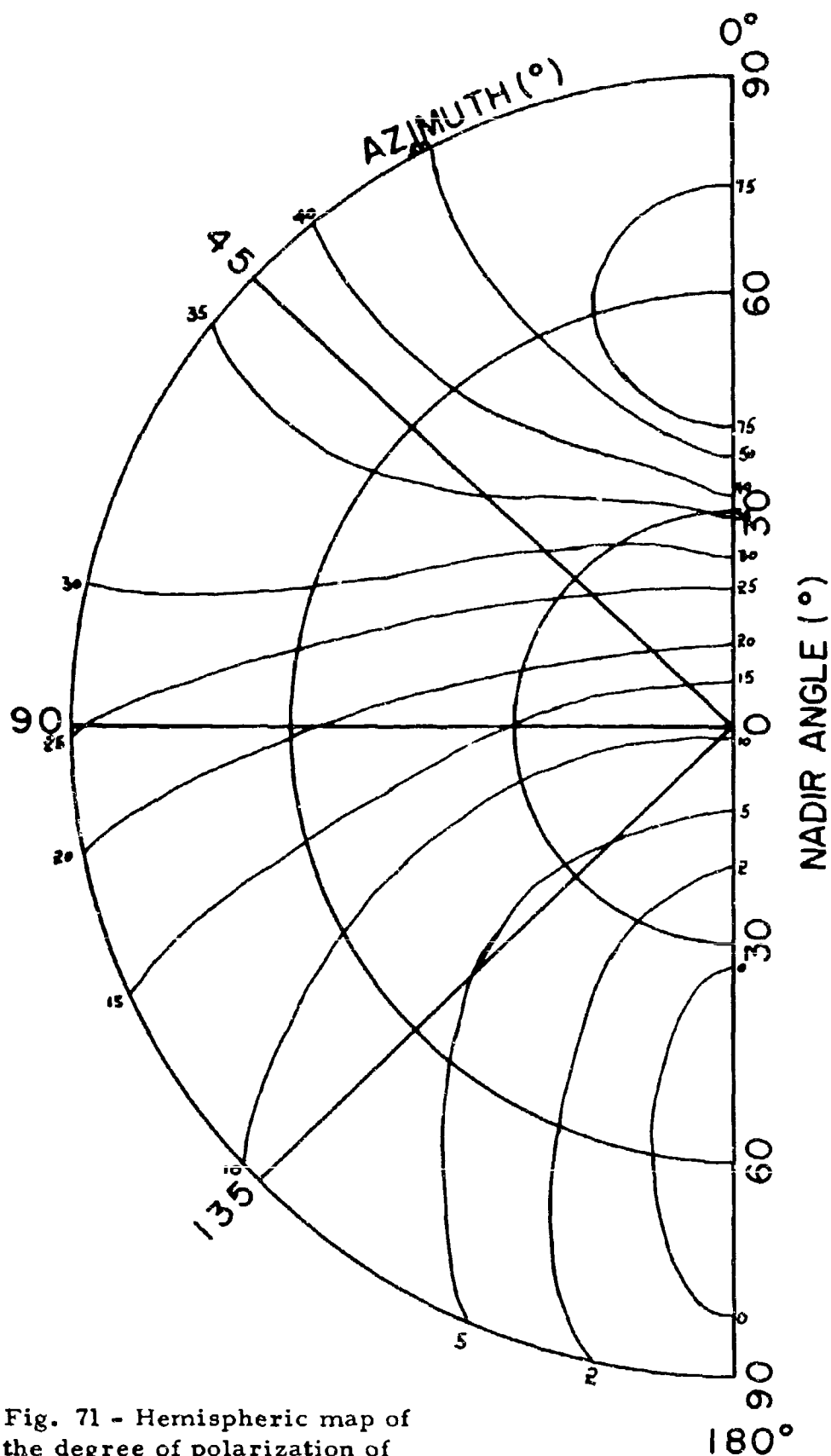


Fig. 71 - Hemispheric map of the degree of polarization of radiation reflected from weathered blacktop ($\theta_0 = 53.1^\circ$, $\lambda = 6430\text{\AA}$)

Fig. 72 - Directional reflectance of weathered concrete (principal plane, $\theta_0 = 78.5^\circ$)

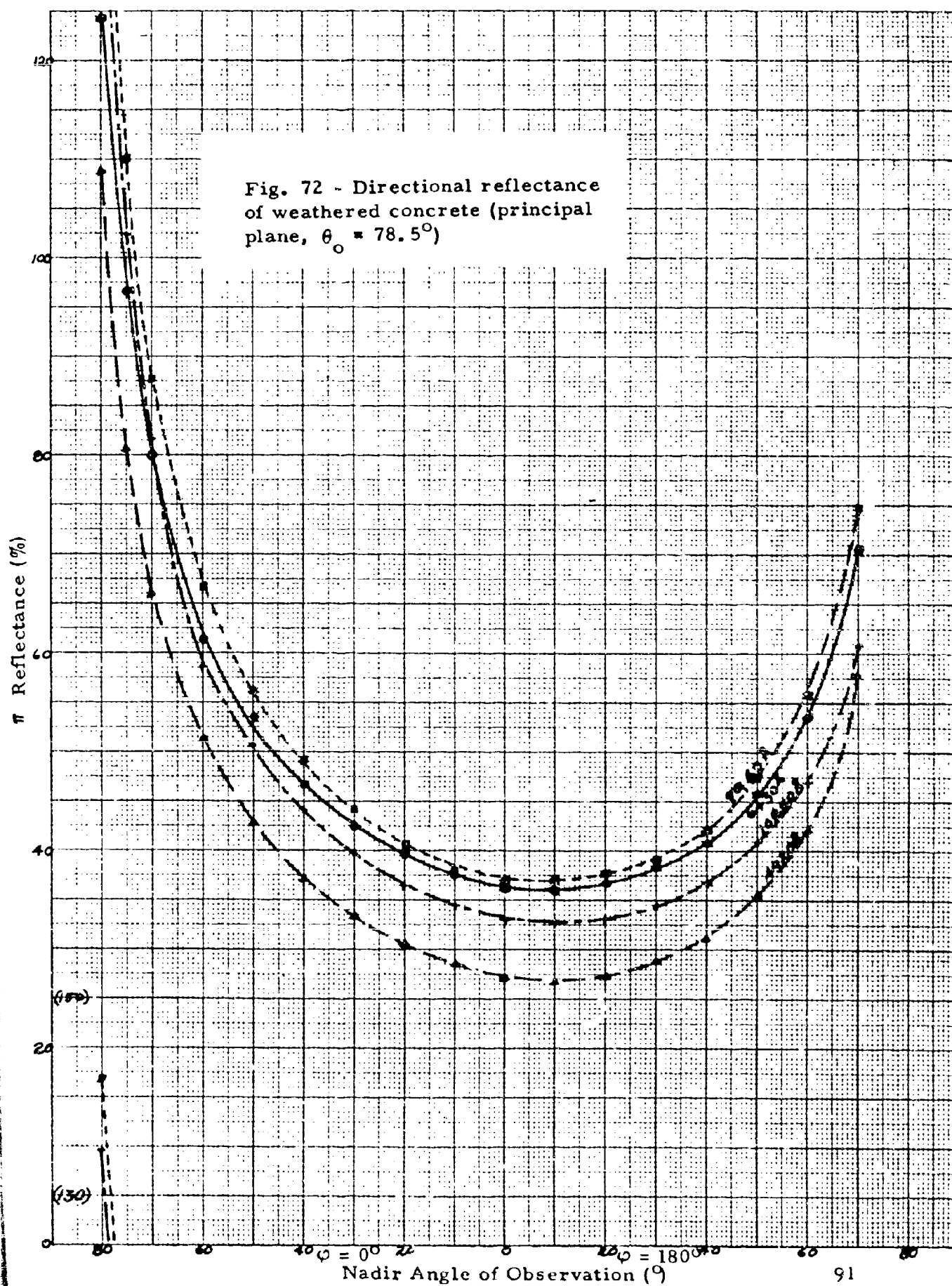


Fig. 73 - Degree of polarization of radiation reflected from weathered concrete (principal plane, $\theta_0 = 78.5^\circ$)

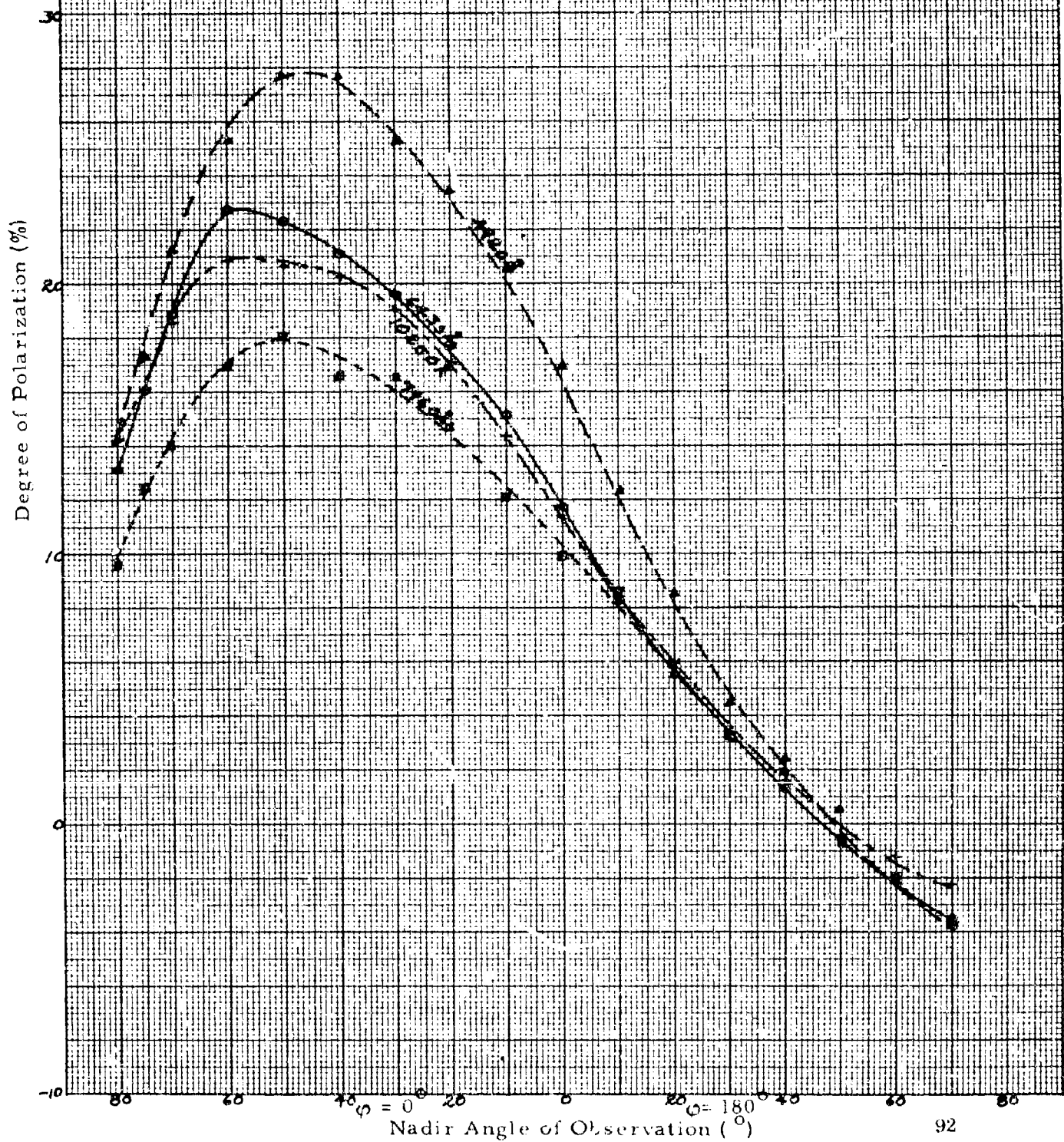


Fig. 74 - Directional reflectance of weathered concrete (principal plane, $\theta_o = 53.1^\circ$)

π Reflectance (%)

60

40

20

0

Nadir Angle of Observation ($^\circ$)

0

40

80

120

160

200

240

280

320

360

400

440

480

520

560

600

640

680

720

760

800

840

880

920

960

1000

1040

1080

1120

1160

1200

1240

1280

1320

1360

1400

1440

1480

1520

1560

1600

1640

1680

1720

1760

1800

1840

1880

1920

1960

2000

2040

2080

2120

2160

2200

2240

2280

2320

2360

2400

2440

2480

2520

2560

2600

2640

2680

2720

2760

2800

2840

2880

2920

2960

3000

3040

3080

3120

3160

3200

3240

3280

3320

3360

3400

3440

3480

3520

3560

3600

3640

3680

3720

3760

3800

3840

3880

3920

3960

4000

4040

4080

4120

4160

4200

4240

4280

4320

4360

4400

4440

4480

4520

4560

4600

4640

4680

4720

4760

4800

4840

4880

4920

4960

5000

5040

5080

5120

5160

5200

5240

5280

5320

5360

5400

5440

5480

5520

5560

5600

5640

5680

5720

5760

5800

5840

5880

5920

5960

6000

6040

6080

6120

6160

6200

6240

6280

6320

6360

6400

6440

6480

6520

6560

6600

6640

6680

6720

6760

6800

6840

6880

6920

6960

7000

7040

7080

7120

7160

7200

7240

7280

7320

7360

7400

7440

7480

7520

7560

7600

7640

7680

7720

7760

7800

7840

7880

7920

7960

8000

8040

8080

8120

8160

8200

8240

8280

8320

8360

8400

8440

8480

8520

8560

8600

8640

8680

8720

8760

8800

8840

8880

8920

8960

9000

9040

9080

9120

9160

9200

9240

9280

9320

9360

9400

9440

9480

9520

9560

9600

9640

9680

9720

9760

9800

9840

9880

9920

9960

10000

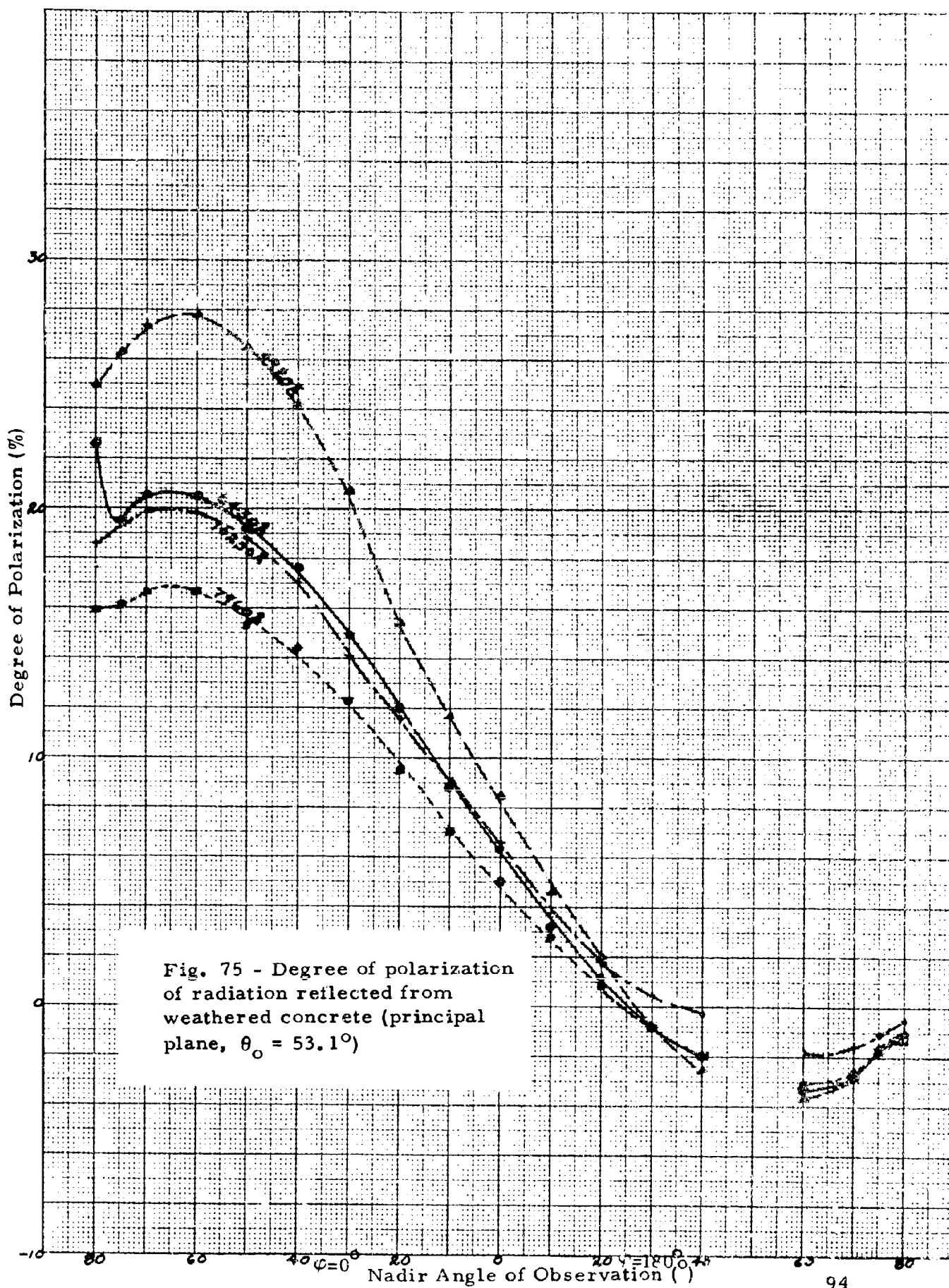


Fig. 76 - Directional reflectance
of weathered concrete (results
independent of azimuth, $\theta_o = 0^\circ$)

π Reflectance (%)

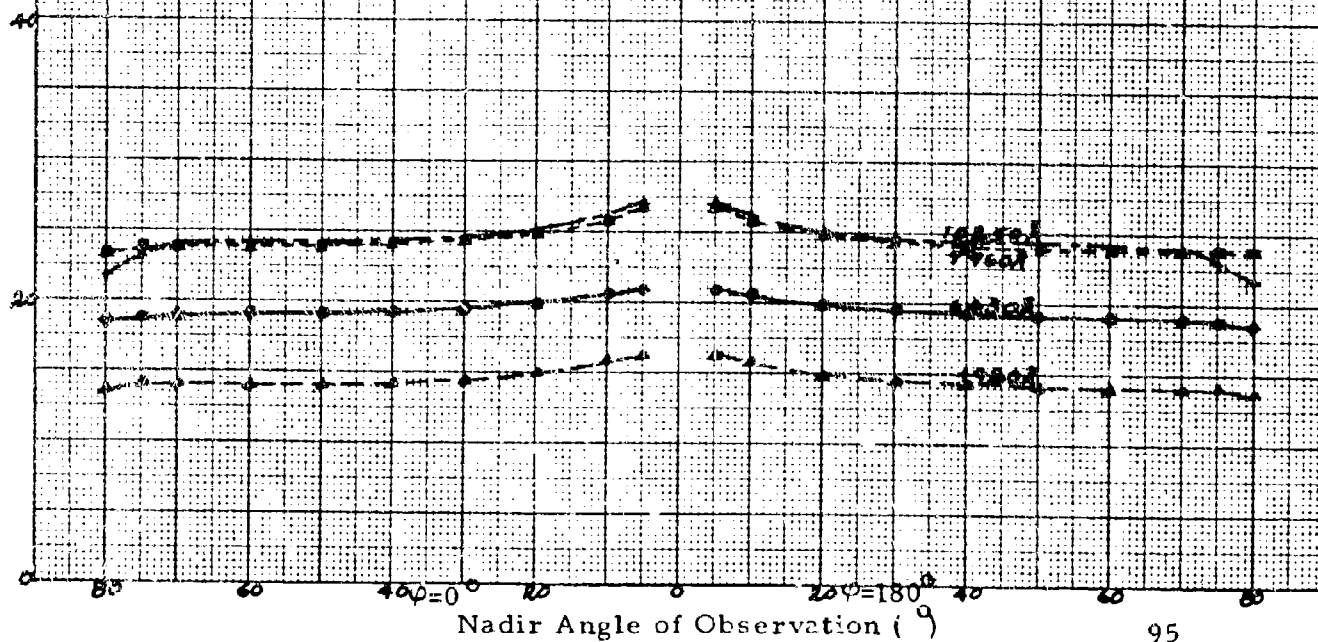
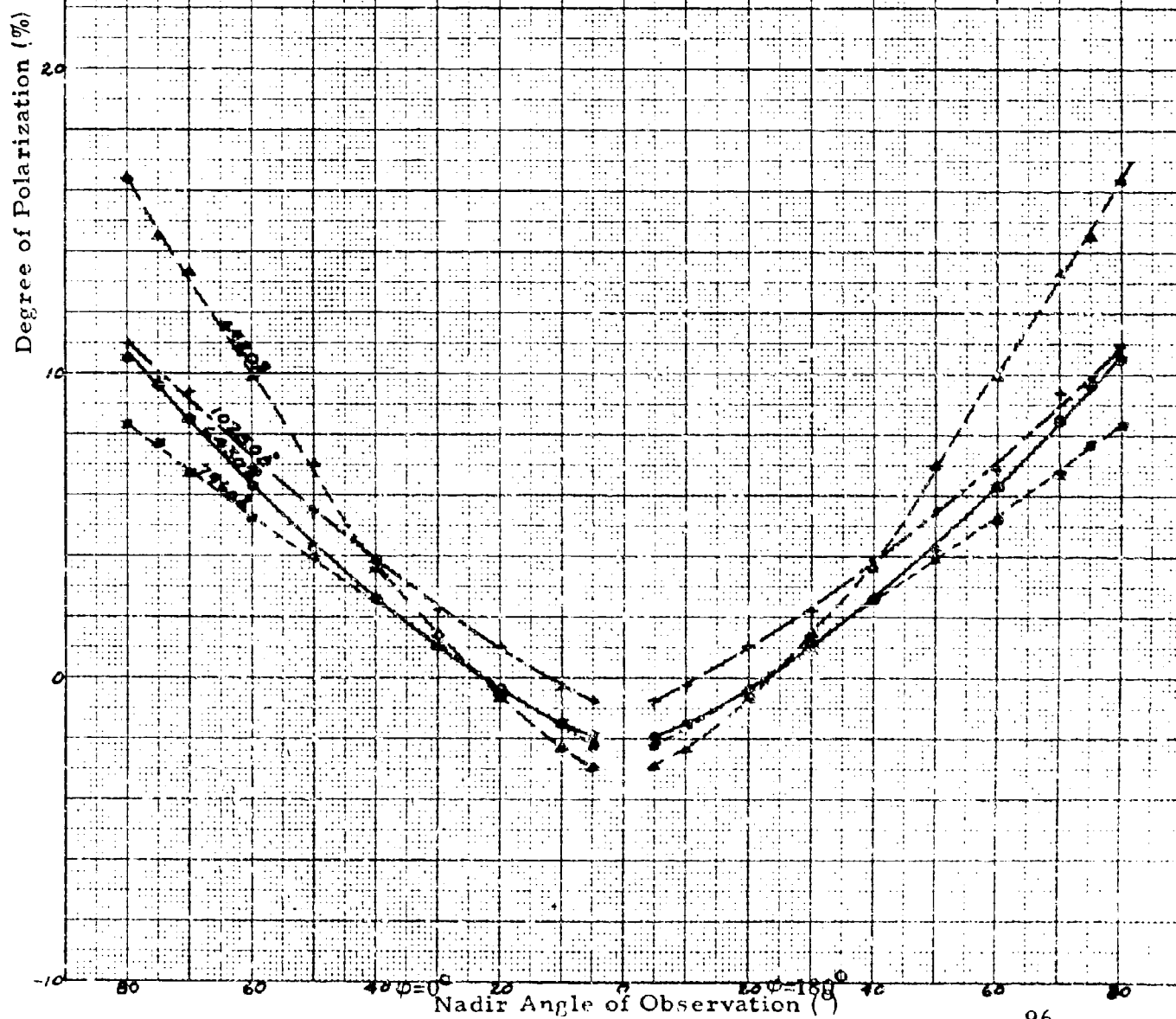


Fig. 77 - Degree of polarization
of radiation reflected from
weathered concrete (results
independent of azimuth, $\theta_0 = 0^\circ$)



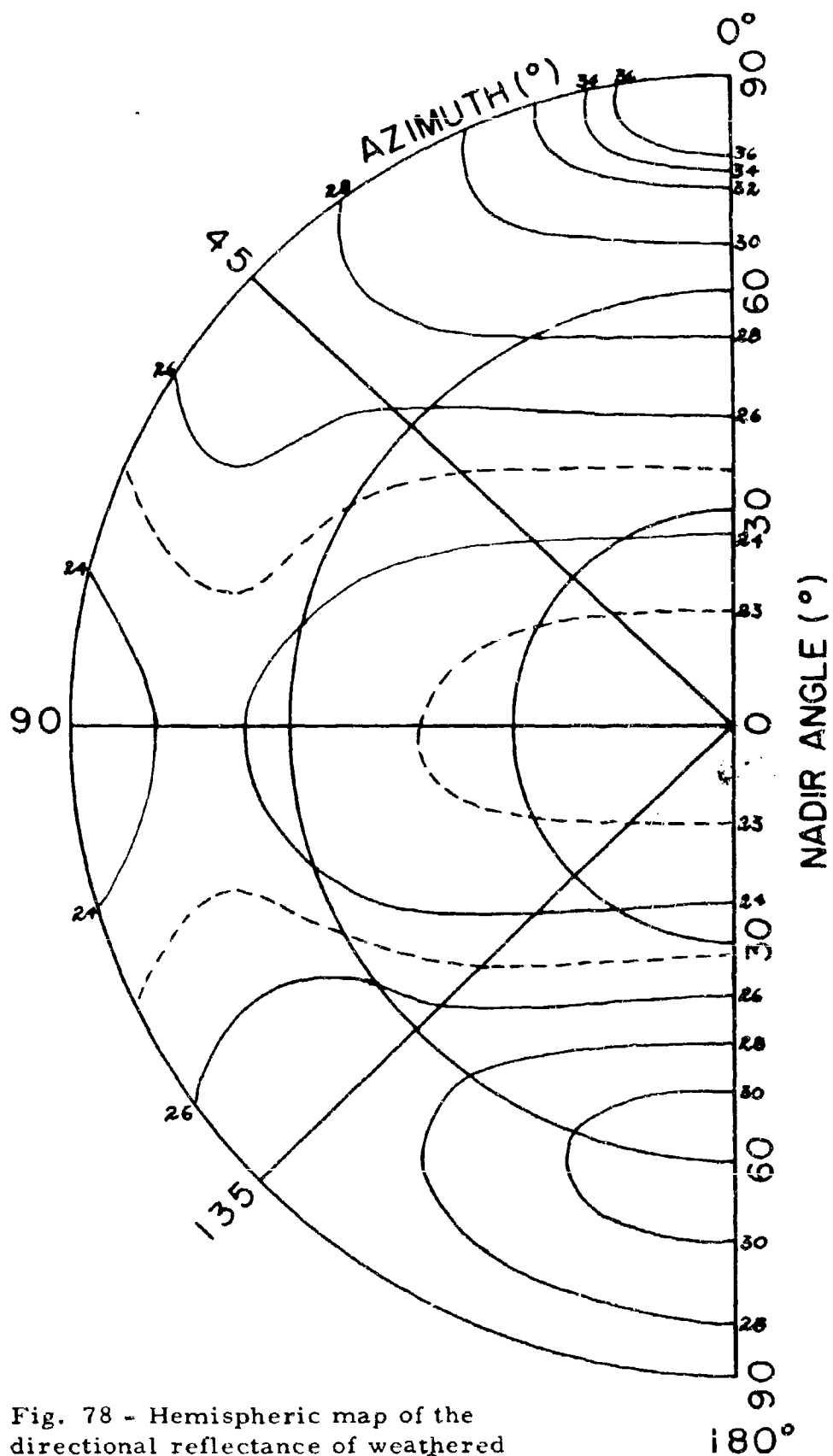


Fig. 78 - Hemispheric map of the directional reflectance of weathered concrete ($\theta_0 = 53.1^\circ$, $\lambda = 6430\text{\AA}$)

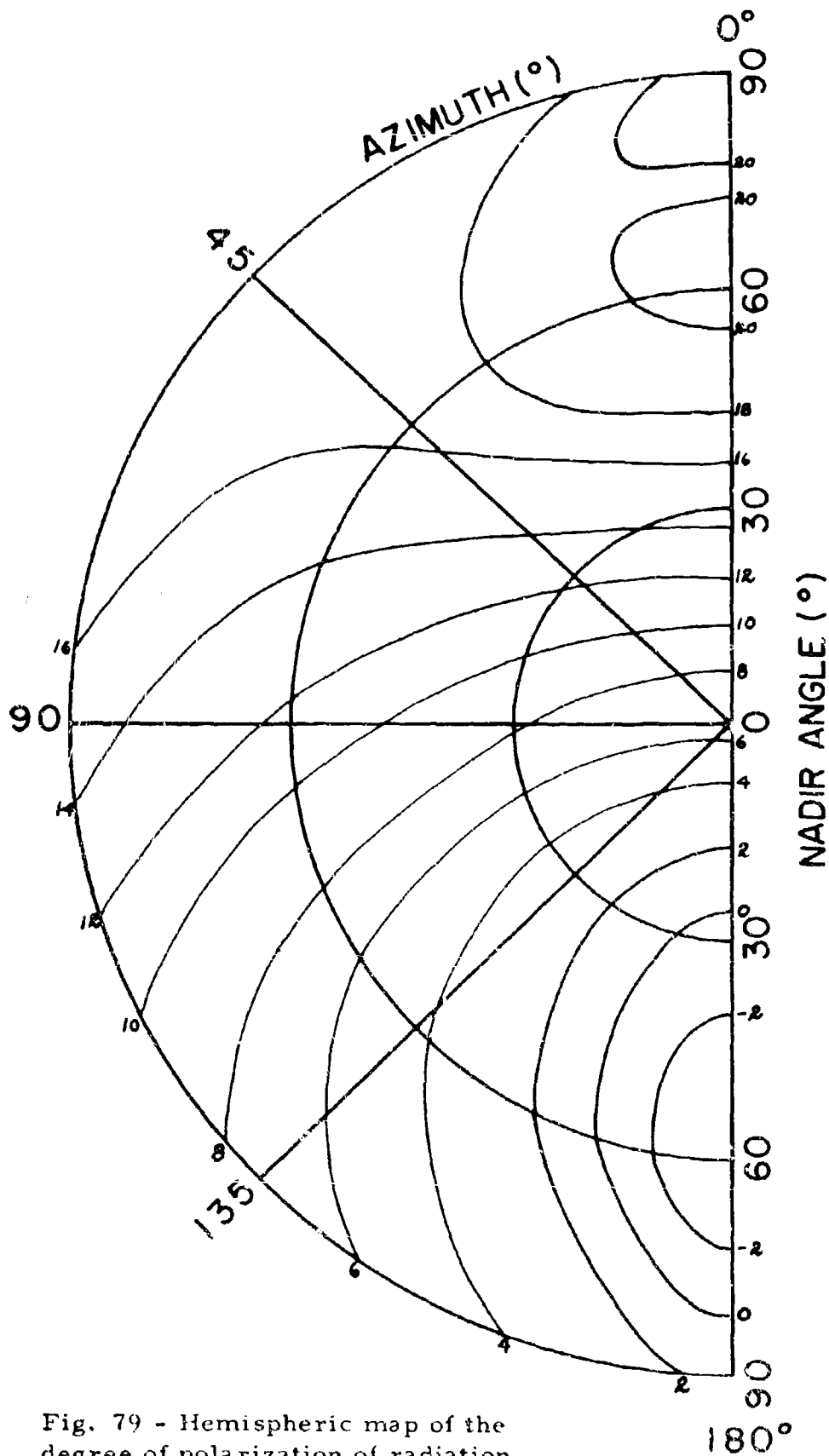
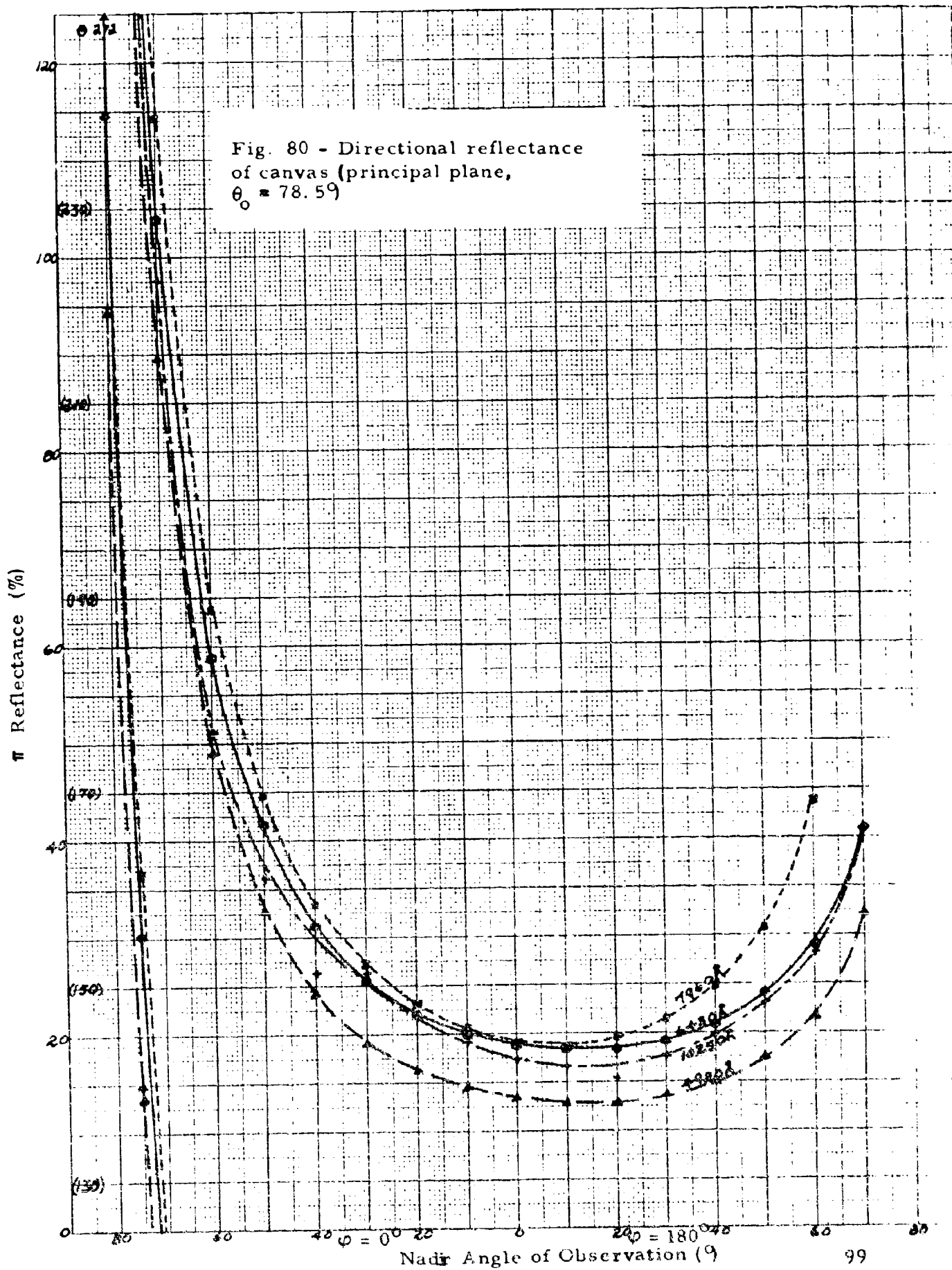


Fig. 79 - Hemispheric map of the degree of polarization of radiation reflected from weathered concrete. ($\theta_0 = 53.1^\circ$, $\lambda = 6430\text{\AA}$)



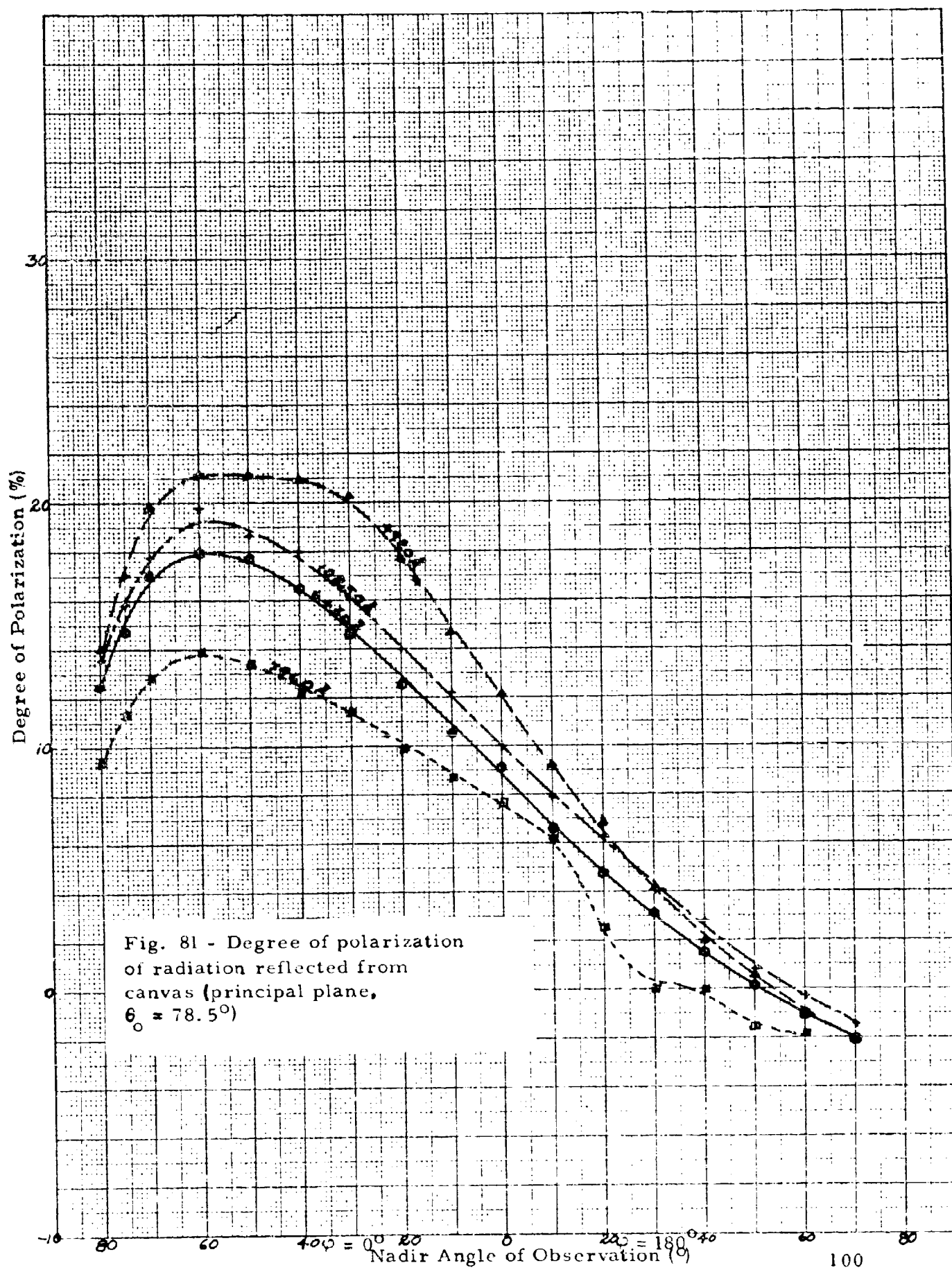


Fig. 82 - Directional reflectance of canvas (principal plane, $\theta_0 \approx 53.1^\circ$)

π Reflectance (%)

40

20

0

80

60

40

20

0

20

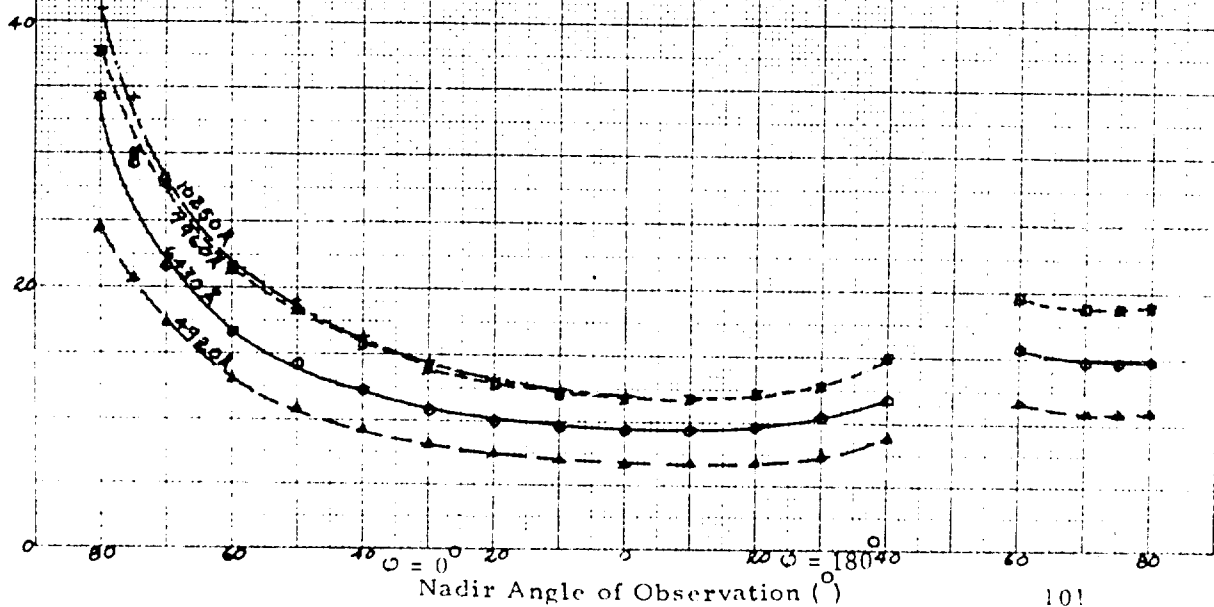
40

60

80

Nadir Angle of Observation ($^\circ$)

101



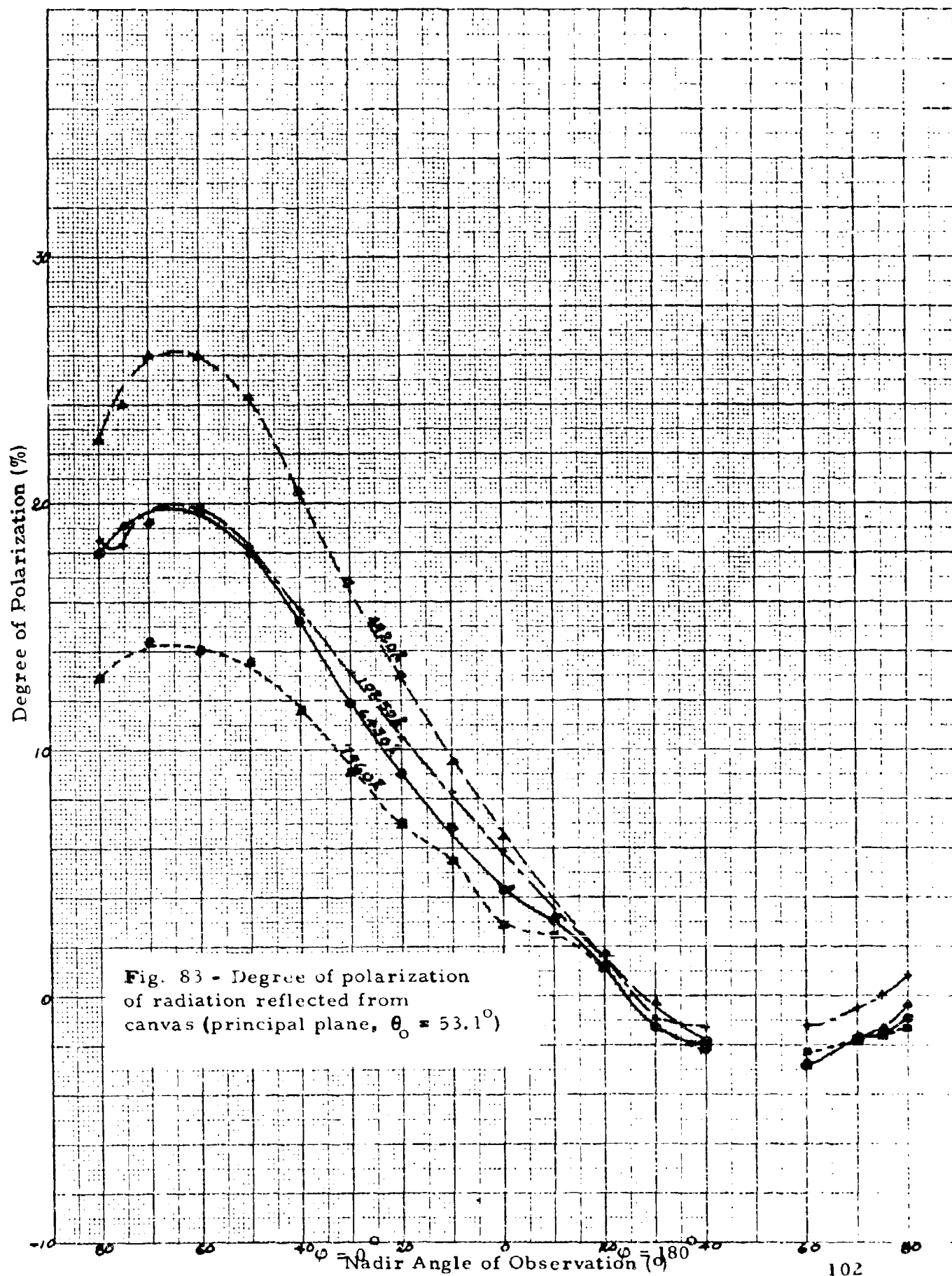


Fig. 84 - Directional reflectance of canvas (results independent of azimuth, $\theta_0 = 0^\circ$)

π Reflectance (%)

20

10

0

80

60

40

$\phi = 0^\circ$

20

0

20

$\phi = 180^\circ$

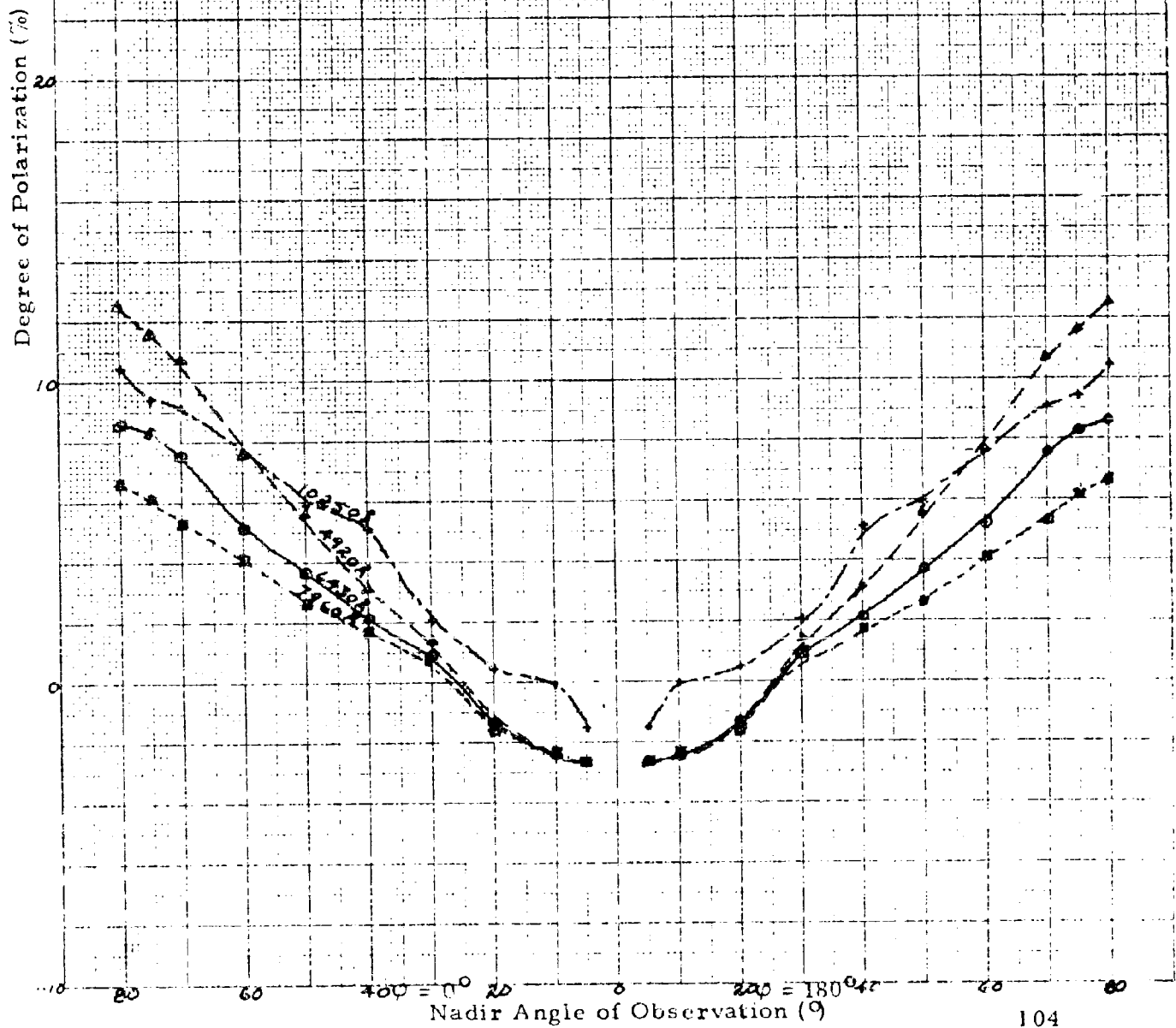
40

60

80

Nadir Angle of Observation (ϕ)

Fig. 85 - Degree of polarization
of radiation reflected from
canvas (results independent
of azimuth, $\theta_0 = 0^\circ$)



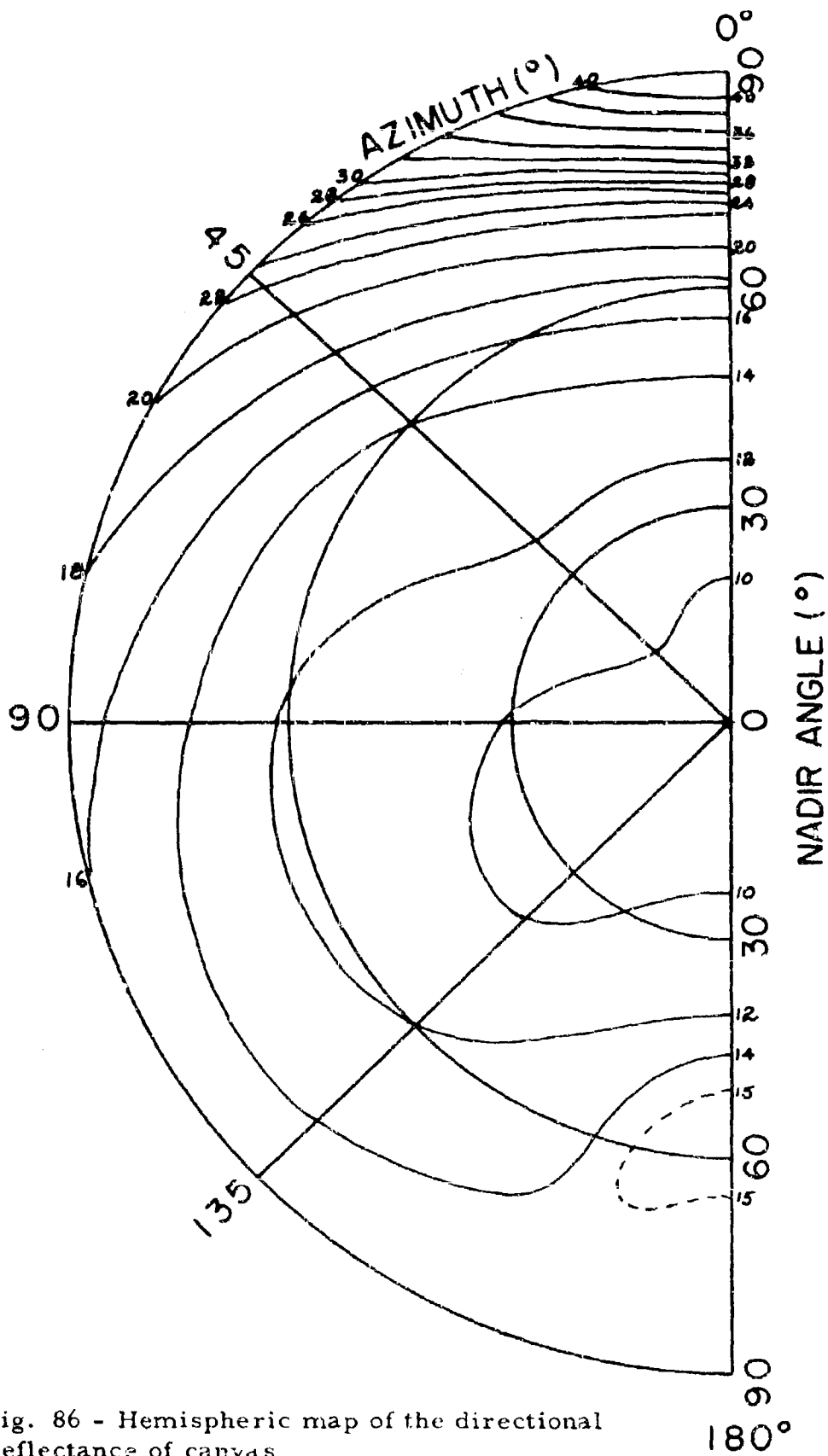


Fig. 86 - Hemispheric map of the directional reflectance of canvas.
 $(\theta_0 = 53.1^\circ, \lambda = 6430\text{\AA})$

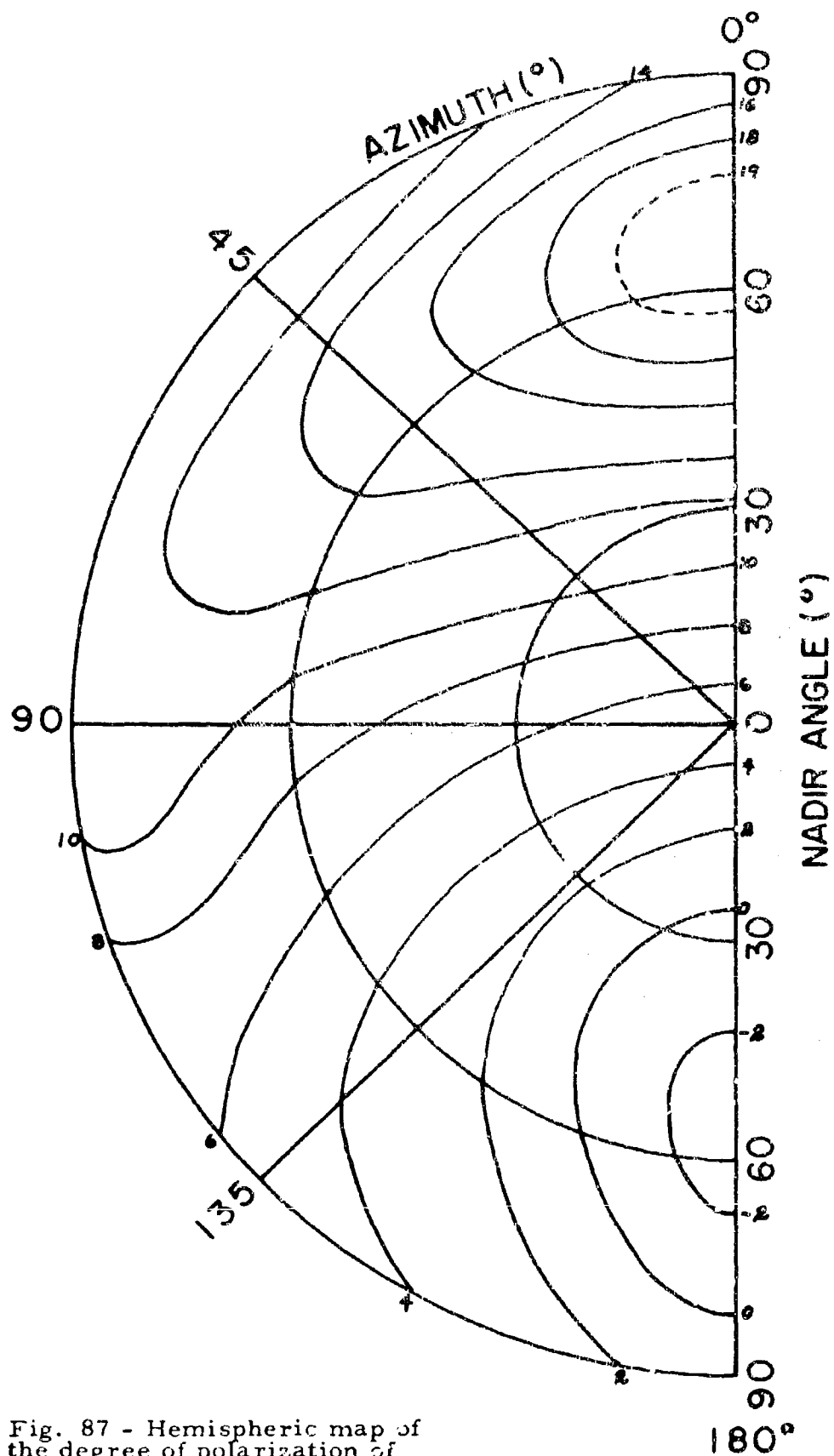


Fig. 87 - Hemispheric map of the degree of polarization of radiation reflected from canvas ($\theta_o = 53.1^\circ$, $\lambda = 6430\text{\AA}$)

IV. Theory

The aim of the following sections is to incorporate the laboratory measurements of the directional reflectance and degree of polarization of the reflected radiation for a given sample into the solution of the radiative transfer equation. This enables one, with reasonable approximation to compute the intensity and the degree of polarization of the radiation emerging from the top of the atmosphere. Finally, the effects of the atmosphere on the contrast inherent between an object and the surrounding background will be shown. Before proceeding, it seems wise to mention the assumptions underlying some of the above statements, and to review the work on contrasts due to R. Fraser (1964).

In the late 1940's, S. Chandrasekhar was able to formally solve the equation of radiative transfer, including the effects of polarization and multiple scattering. The solution appeared as a series of articles in the Astrophysical Journal which were collectively presented in his treatise of 1950 titled Radiative Transfer. The most important restrictive assumption to realize is that the solution obtained has relevance for a so-called Rayleigh atmosphere, i. e. one in which the scattering particles are very small compared to the wavelength of radiation. However, a "real" atmosphere contains larger particles, usually referred to as aerosols, and composed of dust, by-products of combustion processes, etc.. Attempts to include the presence of aerosols in the equation of radiative transfer have been made by several authors, in particular Z. Sekera (1956), R. Fraser (1959), and

D. Deirmendjian (1957). The problem is complicated by several practical considerations. In the first place, one must have good measurements of the size distribution of aerosol particles per unit volume. This immediately raises the question of whether this distribution remains invariant with altitude, as well as the nature of the vertical density profile of aerosol content. It was also found that the aerosol content of the atmosphere is dependent on geographical location, and even at the same locality may vary with time. The approximations usually resorted to, which will be followed in this report, assume that the density of aerosol particles decreases exponentially with altitude, and that the size distribution of aerosol particles per unit volume is constant. These assumptions simplify the transfer equation considerably once an aerosol model is chosen. We will elaborate on this later in the text.

Another important assumption introduced by Chandrasekhar in order to make the problem more tractable is that the atmosphere is idealized in that it is considered to be plane parallel. In other words, the atmosphere is considered to be bounded by two parallel planes of infinite extent such that the characteristics of the atmosphere depend only on the altitude. This idealization avoids the problem of sphericity of the atmosphere and Earth, and the assumption is valid as long as one is not interested in atmospheric effects near the horizon.

As an application of his solution to the molecular scattering problem, which was originally solved assuming that there was no ground present,

(that is, the atmosphere extended indefinitely downward), Chandrasekhar introduced the effects that the presence of a ground would have on the solution that he obtained. To be more specific, a Lambert surface was chosen for two reasons. First, since a Lambert surface is one which reflects incident radiation with the same intensity in all directions, and in addition, the reflected light is unpolarized, the resulting equations were very much simplified. Secondly, it was believed that the approximation of a real surface by a Lambert surface was sufficiently accurate for most practical purposes. It was shown that the presence of the ground created an additive correction to the so-called "standard" solution; that is the solution obtained without the presence of a ground. In 1960, extensive tables were published (Coulson, Dave, and Sekera) giving the numerical solution of the transfer problem with a Lambert surface according to the theory of Chandrasekhar. Fraser has used these tables in determining the atmospheric effects on contrasts. Our major innovation, of course, will be to introduce a non-Lambertian surface.

Before doing this, it seems appropriate at this time to present a statement of the problem, and to introduce the necessary notation.

In figure 88, we have a simplified representation of the physical aspects of the problem. A small target, resting on an infinite homogeneous background, both illuminated by sunlight, is viewed by an observer (or instrument) situated at the top of the atmosphere. The field of view is larger than the solid angle subtended by the target, and therefore a

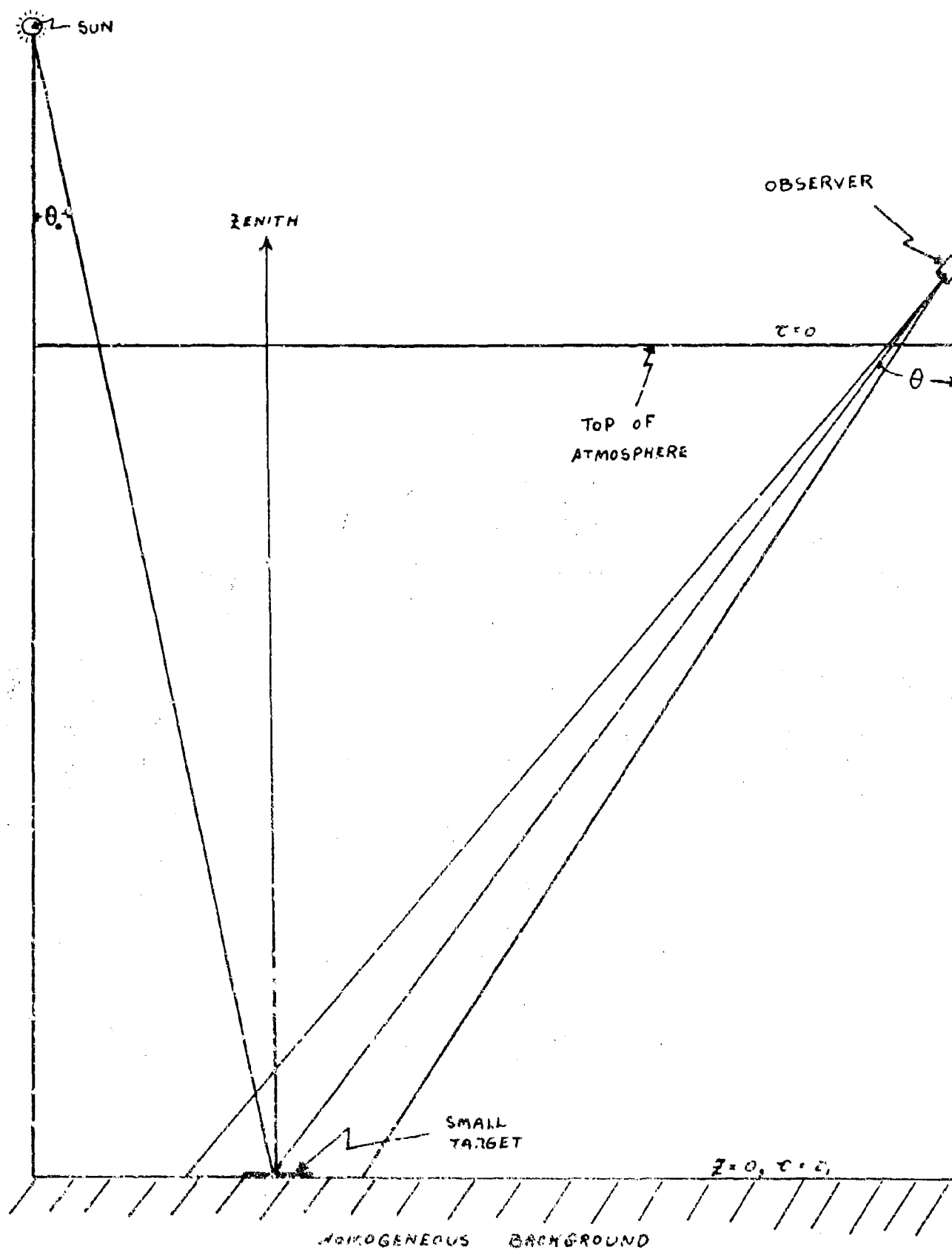


Figure 88 - A Simplified Representation of the Contrast Determination Problem

"contrast" between the target and the background is perceived. It is natural to call this an apparent contrast, and reserve the term intrinsic contrast for that contrast an observer would perceive at the bottom of the atmosphere. In other words, the intrinsic contrast is altered due to the presence of the atmosphere.

The notation to be employed in what follows is listed below. Detailed explanation of some of these items will be postponed until the need for their introduction arises.

- $\theta_0 \equiv$ the zenith angle of the sun (as seen from the target) or the nadir angle of the target as seen from the direction of the sun
- $\mu_0 \equiv \cos \theta_0$
- $\theta \equiv$ the zenith angle of the observer (as seen from the target) or the nadir angle of the target (as seen from the observer)
- $\mu \equiv \cos \theta$
- $\varphi \equiv$ the azimuth or horizontal angular measure of the observer relative to the sun (i. e. the sun is at azimuth $\varphi = 0^\circ$). In the figure, the observer is at $\varphi = 180^\circ$ looking in the direction $\varphi = 0^\circ$.
- $z \equiv$ altitude
- $\lambda \equiv$ wavelength of radiation
- $\beta^R(\lambda, z) \equiv$ the volume scattering coefficient for the Rayleigh or "molecular" part of the atmosphere. This is the rate at which incident energy is scattered per unit volume per unit path length. It depends on wavelength and density, which in turn implies an altitude dependence.
- $\beta^A \equiv$ the corresponding volume scattering coefficient for the aerosol content of the atmosphere.

τ^R \equiv the normal optical thickness of the molecular component of the atmosphere.

$$\text{By definition, } \tau^R = \int_0^{\infty} \beta^R(z) dz.$$

τ^A \equiv the normal optical thickness of the aerosol component of the atmosphere.

$$\tau^A = \int_0^{\infty} \beta^A(z) dz$$

τ_1 \equiv the total normal optical thickness of the atmosphere.

$$\tau_1 = \tau^R + \tau^A = \int_0^{\infty} \beta^R(z) dz + \int_0^{\infty} \beta^A(z) dz$$

$I_t(0; \mu, \varphi)$ \equiv the emergent intensity of the target-reflected radiation at the top of the atmosphere in the direction μ, φ .

$I_t(\tau_1; \mu, \varphi)$ \equiv the intensity of the target reflected radiation at the ground

$I_B(0; \mu, \varphi)$ $\left\{ \begin{array}{l} \equiv \text{the corresponding intensities for the homogeneous} \\ \text{background.} \end{array} \right.$
 $I_B(\tau_1; \mu, \varphi)$

The quantities $\rho(\mu, \varphi)$, $P(\mu, \varphi)$,

$$\begin{bmatrix} I_e \\ I_r \\ U \\ V \end{bmatrix} \quad \text{or} \quad \begin{bmatrix} I \\ Q \\ U \\ V \end{bmatrix}$$

have been introduced previously, and their complete description will not be repeated here. However, it

is important to remember that I_e and I_r are the intensity components parallel and perpendicular to the vertical plane passing through the zenith and the azimuth of the observer. Later on, we will have need for intensity components parallel and perpendicular to the plane of

polarization. The notation I_i and I_j will be reserved for this.

$\gamma \equiv$ the scattering angle. This is the angle formed by the incident and reflected beams. The plane determined by these beams is referred to as the scattering plane.

$\hat{L}_{11}(\gamma) \equiv$ These are normalized matrix elements describing the scattering properties of a particular aerosol model.
 $\hat{L}_{12}(\gamma)$

$C(0; \mu, \varphi) \equiv$ apparent contrast at the top of the atmosphere, and in the direction μ, φ .

$C(\tau_1; \mu, \varphi) \equiv$ intrinsic contrast at the bottom in the direction μ, φ .

$y(\tau_1; \mu, \varphi) \equiv$ the contrast attenuation coefficient, which holds in the absence of an analyzer in the observer's optical system.

$y_e(\tau_1, \mu, \varphi) \equiv$ the contrast attenuation coefficient which holds if the transmission plane of an analyzer in the observer's system is oriented perpendicular to the plane of polarization.

$y_r(\tau_1; \mu, \varphi) \equiv$ the corresponding contrast attenuation coefficient which holds if the transmission plane of an analyzer is oriented parallel to the plane of polarization.

Having introduced the notations for contrast and the contrast attenuation coefficient, it remains to define these terms and point out the great utility of the concept of the contrast attenuation coefficient. The following discussion of these parameters is patterned after that of Fraser (1964). The contrast at any altitude z corresponding to a normal optical depth τ , and in the direction μ, φ , is defined as:

$$C(\tau; \mu, \varphi) \equiv \frac{I_t(\tau; \mu, \varphi) - I_B(\tau; \mu, \varphi)}{I_B(\tau; \mu, \varphi)}$$

In particular, the intrinsic contrast is:

$$C(\tau_1; \mu, \varphi) = \frac{I_t(\tau_1; \mu, \varphi) - I_B(\tau_1; \mu, \varphi)}{I_B(\tau_1; \mu, \varphi)}$$

The apparent contrast as perceived at the top of the atmosphere is:

$$C(0; \mu, \varphi) = \frac{I_t(0; \mu, \varphi) - I_B(0; \mu, \varphi)}{I_B(0; \mu, \varphi)}$$

The emergent intensity $I(0; \mu, \varphi)$ is related to the intensity reflected from the ground, $I(\tau_1; \mu, \varphi)$, by integrating the transfer equation. The result may formally be written:

$$(1) \quad I(0; \mu, \varphi) = I(\tau_1; \mu, \varphi) e^{-\tau_1/\mu} + \int_0^{\tau_1} J(t; \mu, \varphi) e^{-t/\mu} \frac{dt}{\mu}$$

The quantity J is usually referred to as the source function, and the integral term is responsible for multiple scattering effects. The assumption of very small target size implies that the contribution of the target to multiple scattering effects is minimal. Hence if one assumes that the multiple scattering effects above the target are the same as above the surrounding background, then the integral terms for both the target and background will be the same. Therefore, substituting equation (1) into the definition of apparent contrast at the top of the atmosphere, we have:

$$(2) \quad C(0; \mu, \varphi) = \frac{\{ I_t(\tau_1; \mu, \varphi) - I_B(\tau_1; \mu, \varphi) \} e^{-\tau_1/\mu}}{I_B(\tau_1; \mu, \varphi) e^{-\tau_1/\mu} + \int_0^{\tau_1} J(t; \mu, \varphi) e^{-t/\mu} \frac{dt}{\mu}}$$

The contrast attenuation coefficient, $y(\tau_1; \mu, \varphi)$ is now defined such that:

$$(3) \quad C(0; \mu, \varphi) = y(\tau_1; \mu, \varphi) C(\tau_1; \mu, \varphi)$$

In other words, the apparent contrast is the product of the intrinsic contrast and the contrast attenuation coefficient. Hence $y(\tau_1; \mu, \varphi)$ is a measure of the reduction of contrast due to atmospheric effects. Since

$$C(\tau_1; \mu, \varphi) = \frac{I_t(\tau_1; \mu, \varphi) - I_B(\tau_1; \mu, \varphi)}{I_B(\tau_1; \mu, \varphi)}, \text{ we have by substitution,}$$

$$y(\tau_1; \mu, \varphi) = \frac{C(0; \mu, \varphi)}{C(\tau_1; \mu, \varphi)} = \frac{I_B(\tau_1; \mu, \varphi) e^{-\tau_1/\mu}}{I_B(\tau_1; \mu, \varphi) e^{-\tau_1/\mu} + \int_0^{\tau_1} J(t; \mu, \varphi) e^{-t/\mu} \frac{dt}{\mu}}.$$

The utility of $y(\tau_1; \mu, \varphi)$ can be seen from the fact that the resulting expression is independent of the target, and depends only on the background. The characteristics of the target are, of course, introduced in the calculation of the intrinsic contrast.

It is further seen from the expression for the contrast attenuation coefficient that $0 \leq y(\tau_1; \mu, \varphi) \leq 1$. If the atmosphere is optically thick so that τ_1 is relatively large, then $I_B(\tau_1; \mu, \varphi) e^{-\tau_1/\mu}$ will be small, while $\int_0^{\tau_1} J(t; \mu, \varphi) e^{-t/\mu} \frac{dt}{\mu}$ may become quite large, giving rise to a small contrast attenuation coefficient. In this case, the intrinsic contrast

is greatly reduced as the light traverses its path through the atmosphere.

On the other hand, if the atmosphere is optically thin, so that τ_1 is relatively small, then $I_B(\tau_1; \mu, \varphi) e^{-\tau_1/\mu}$ will be large compared to $\int_0^{\tau_1} J(t; \mu, \varphi) e^{-t/\mu} \frac{dt}{\mu}$, and in this case, we have a large contrast

attenuation coefficient. Hence the intrinsic contrast is not greatly reduced as the light passes out through the atmosphere. Of course, these qualitative descriptions are what one would intuitively expect in an optically thick or optically thin atmosphere.

At this point, it is useful to distinguish between intensity of radiation which is directly transmitted and that which is diffusely transmitted. A convenient notation for this purpose is described as follows: In general, the emergent intensity may be considered to be composed of five separate components. The word "component" here is used synonymously with "contribution", and should not be confused with the previous reference to vector components of intensity.

$I_s \equiv$ the solution to the radiative transfer problem in the absence of a "ground". This is the so-called standard solution alluded to previously.

$I_{DD} \equiv$ that contribution to the emergent radiation which consists of light which was transmitted directly downward through the atmosphere, reflected, and transmitted directly outward through the atmosphere.

$I_{dD} \equiv$ that contribution to the emergent radiation which consists of light which was transmitted diffusely downward through the atmosphere, and transmitted directly outward through the atmosphere.

$I_{Dd} \equiv$ that contribution to the emergent radiation which consists of light which was transmitted directly downward through the atmosphere

and transmitted diffusely outward through the atmosphere.

I_{dd} \equiv that contribution to the emergent radiation which consists of light which was transmitted diffusely downward through the atmosphere, and transmitted diffusely outward through the atmosphere.

Before discussing these components in detail, and presenting the expressions which will be used for each, it is worthwhile to note that the contrast attenuation coefficient can now be written as:

$$y(\tau_1; \mu, \varphi) = \frac{I_{DD}(\mu, \varphi) + I_{dD}(\mu, \varphi)}{I_s(\mu, \varphi) + I_{DD}(\mu, \varphi) + I_{dD}(\mu, \varphi) + I_{Dd}(\mu, \varphi) + I_{dd}(\mu, \varphi)}$$

(For $y_e(\tau_1; \mu, \varphi)$ and $y_r(\tau_1; \mu, \varphi)$, we need compute the i and j components of each of the above five "contributions".)

As a first step in computing these intensities, it is necessary to determine the normal optical thickness which applies. For the molecular component of the atmosphere, the following table is taken from

Deirmendjian (1955):

Table II: The normal optical thickness, τ , as a function of wavelength, λ .

τ	1.00	0.50	0.25	0.15	0.10	0.05	0.02
λ (\AA)	3120	3715	4365	4950	5460	6440	8090

In order to illustrate the computation of $y(\tau_1; \mu, \varphi)$, we have chosen a particular sample. More specifically, we shall introduce the surface reflection and polarization characteristics of desert soil for the wavelength $\lambda = 6430\text{\AA}$, and a zenith sun angle of $\theta_0 = 53.1^\circ$ ($\mu_0 = .60$). Hence,

for this wavelength, the required molecular normal optical depth is

$$\tau^R = .05.$$

In determining τ^A , the normal optical depth of the aerosol content, one must choose a model for the size distribution of aerosols per unit volume. We have chosen a "continental" model aerosol from among several considered by Fraser (1959) as being most representative for our purposes. It is characterized by the following size distribution:

Interval of radius, a (micron)		Number of particles per cm ³ of air per micron of radius	Number of particles per cm ³
Lower	Upper		
.03	0.1	2.251×10^4	1575.7
0.1	20.0	$2.251 \times a^{-4}$	$\frac{753.3}{2329.0}$

As mentioned previously, this surface value will be assumed to decrease exponentially. For this model, Fraser computed the volume scattering coefficients at the surface for three different wavelengths. His result for $\lambda = 6250\text{\AA}$ is $\beta^A = 1.06 \times 10^{-6} \text{ cm}^{-1}$. By interpolating according to an inverse wavelength dependence, we have for $\lambda = 6430\text{\AA}$, that $\beta^A(0) = 1.03 \times 10^{-6} \text{ cm}^{-1}$. Finally, utilizing the assumption of an exponential density decrease with altitude, we have that $\beta^A(z) = \beta^A(0) e^{-z/H}$. The parameter H is called the scale height. Physically, it is that altitude at which the volume scattering coefficient assumes $1/e$ of its surface value. The value $H = .98$ kilometers is given by Penndorf (1954).

By definition, $\tau^A = \int_0^\infty \beta^A(z) dz = \int_0^\infty \beta^A(0) e^{-z/H} dz = \beta^A(0) H =$

$1.03 \times 10^{-6} \text{ cm}^{-1} \times .98 \times 10^5 \text{ cm} = .101$. Therefore, for $\lambda = 6430 \text{ \AA}$, the total normal optical thickness, $\tau_1^R = \tau^R + \tau^A$ is approximately equal to .15.

We shall now discuss briefly each of the five components, beginning with $I_s(0; \mu, \phi)$. Our aim is to determine the I_e and I_r components for each of the five. To reiterate, the subscript s is for "standard", the reference being to the solution of the radiative transfer equation in the absence of a "ground". In the present problem, I_s consists of contributions from both molecular scattering and aerosol scattering. We have made the simplifying assumption that these scattering processes act independently, so that I_s can be written as $I_s^R + I_s^A$, separating the molecular and aerosol contributions. Hence we desire the solution for I_s^R with a normal optical thickness of $\tau = .05$, and the solution for I_s^A with a normal optical thickness of $\tau = .10$. Values of $I_s^R(0; \mu, \phi)$ for $\tau = .05$ are given in the tables of Coulson, Dave, and Sekera (1960).

Actually the Stokes parameters I and Q, are given which make a determination of I_e and I_r for I_s^R trivial. It is to be noted that this solution includes the effects of multiple scattering. In compiling these tables for I_s^R , an assumption was made that the flux of parallel radiation incident on the top of the atmosphere is set at πF_0 ($F_0 = 1$) units, per unit area oriented normal to the direction of propagation, which, of course,

makes an angle of θ_0 with the zenith. This assumption will be followed in the present report.

In computing I_s^A , we follow the usual approximation of neglecting the effects of multiple scattering, since their inclusion renders the problem intractable. The transfer equation, including primary scattering may be written:

$$\mu \frac{d\vec{I}}{d\tau} = \vec{I} - 1/4 e^{-\tau/\mu_0} \vec{P}^A \vec{F}$$

where:

$$\vec{I} = \begin{bmatrix} I \\ Q \end{bmatrix} = \begin{bmatrix} I_i + I_j \\ I_i - I_j \end{bmatrix}$$

$$\vec{P}^A = \begin{bmatrix} \hat{L}_{11}(\gamma) & \hat{L}_{12}(\gamma) \\ \hat{L}_{12}(\gamma) & \hat{L}_{11}(\gamma) \end{bmatrix}$$

$$\vec{F} = \begin{bmatrix} 1 \\ 0 \end{bmatrix}$$

The scattering matrix \vec{P}^A describes the aerosol scattering of incident radiation, and enables one to compute the intensity components I_i and I_j parallel and perpendicular to the scattering plane, which is normal to the plane of polarization. The elements $\hat{L}_{11}(\gamma)$ and $\hat{L}_{12}(\gamma)$ are the normalized matrix elements introduced previously. Fraser (1959) has computed these elements for the "continental" aerosol model, and for a wavelength $\lambda = 6250 \text{ \AA}$. Since they do not change rapidly with wavelength, these values are also appropriate for $\lambda = 6430 \text{ \AA}$.

An important fact, pointed out by Deirmendjian (1959), is that the assumption of exponential density decrease of aerosol content ensures that $\frac{\partial \hat{L}_{ij}(\gamma)}{\partial \tau} = 0$.

This means that in solving the transfer equation above, these elements can be brought out from under an integral with respect to τ . In fact since,

$$\underline{\vec{P}}^A \vec{F} = \begin{bmatrix} \hat{L}_{11}(\gamma) & \hat{L}_{12}(\gamma) \\ \hat{L}_{12}(\gamma) & \hat{L}_{11}(\gamma) \end{bmatrix} \begin{bmatrix} 1 \\ 0 \end{bmatrix} = \begin{bmatrix} \hat{L}_{11}(\gamma) \\ \hat{L}_{12}(\gamma) \end{bmatrix}.$$

The transfer equation assumes the form:

$$\mu \frac{d}{d\tau} \begin{bmatrix} I \\ Q \end{bmatrix} = \begin{bmatrix} I \\ Q \end{bmatrix} - 1/4 e^{-\tau/\mu_0} \begin{bmatrix} \hat{L}_{11}(\gamma) \\ \hat{L}_{12}(\gamma) \end{bmatrix},$$

or

$$(5a) \quad \mu \frac{dI}{d\tau} = I - 1/4 \hat{L}_{11}(\gamma) e^{-\tau/\mu_0}$$

$$(5b) \quad \mu \frac{dQ}{d\tau} = Q - 1/4 \hat{L}_{12}(\gamma) e^{-\tau/\mu_0}$$

The solutions to these linear differential equations may be written, remembering that the boundary conditions are such that there is no radiation reflected from a "ground", as:

$$(6a) \quad I = I_i + I_j = \frac{1}{4\mu} \hat{L}_{11}(\gamma) \frac{\mu\mu_0}{\mu + \mu_0} \left\{ 1 - e^{-\tau} \left\{ \frac{1}{\mu} + \frac{1}{\mu_0} \right\} \right\}$$

$$(6b) \quad Q = I_i - I_j = \frac{1}{4\mu} \hat{L}_{12}(\gamma) \frac{\mu\mu_0}{\mu + \mu_0} \left\{ 1 - e^{-\tau} \left\{ \frac{1}{\mu} + \frac{1}{\mu_0} \right\} \right\}$$

or

$$I_i = \frac{1}{8\mu} \frac{\mu\mu_0}{\mu + \mu_0} \left\{ 1 - e^{-\tau^A} \left\{ \frac{1}{\mu} + \frac{1}{\mu_0} \right\} \right\} \left\{ \hat{L}_{11}(\gamma) + \hat{L}_{12}(\gamma) \right\}$$

$$I_j = \frac{1}{8\mu} \frac{\mu\mu_0}{\mu + \mu_0} \left\{ 1 - e^{-\tau^A} \left\{ \frac{1}{\mu} + \frac{1}{\mu_0} \right\} \right\} \left\{ \hat{L}_{11}(\gamma) - \hat{L}_{12}(\gamma) \right\}$$

These components are parallel and perpendicular to the scattering plane. To transform these components to components parallel and perpendicular to the vertical plane through the observer's azimuth, we need subject them to the matrix transformation $\begin{bmatrix} \sin^2 \chi & \cos^2 \chi \\ \cos^2 \chi & \sin^2 \chi \end{bmatrix}$. Hence we have,

$$\begin{bmatrix} I_e \\ I_r \end{bmatrix} = \begin{bmatrix} \sin^2 \chi & \cos^2 \chi \\ \cos^2 \chi & \sin^2 \chi \end{bmatrix} \begin{bmatrix} I_i \\ I_j \end{bmatrix} = \begin{bmatrix} I_i \sin^2 \chi + I_j \cos^2 \chi \\ I_i \cos^2 \chi + I_j \sin^2 \chi \end{bmatrix}.$$

In the computation of $I_{DD}(0; \mu, \varphi)$ we must introduce our laboratory measurements, $\rho(\mu, \varphi)$ and $P(\mu, \varphi)$. If πF_0 units of flux per unit area normal to the direction of propagation are incident on the top of the atmosphere at an angle θ_0 relative to the zenith, then the directly transmitted radiant flux reaching the ground per unit horizontal area is $\pi F_0 \mu_0 e^{-\tau_1/\mu_0}$. The intensity of the radiation reflected into a unit solid angle in the μ, φ direction would be $I^{\text{ref}}(\mu, \varphi) = \rho(\mu, \varphi) \pi F_0 \mu_0 e^{-\tau_1/\mu_0}$. We now make use of the definitions of the Stokes parameters:

$$I = I_e + I_r$$

$$Q = I_e - I_r$$

$$U = (I_e - I_r) \tan 2\chi,$$

$$\text{and } P = \frac{(Q^2 + U^2)^{1/2}}{I}$$

It will be remembered that χ is the angle between the plane of polarization and the vertical plane through the observer's azimuth. The assumption that the plane of polarization is normal to the scattering plane enables one to compute χ by spherical trigonometry. Hence the values of μ_0 , μ , and φ determine the angles χ (and γ) directly. We then have the following relationships:

$$\begin{aligned} P(\mu, \varphi) &= \frac{\{Q^2(\mu, \varphi) + U^2(\mu, \varphi)\}^{1/2}}{I(\mu, \varphi)} = \\ &= \left[\frac{\{I_e(\mu, \varphi) - I_r(\mu, \varphi)\}^2 + \{I_e(\mu, \varphi) - I_r(\mu, \varphi)\}^2 \tan^2 2\chi}{I(\mu, \varphi)} \right]^{1/2} \\ &= \frac{\{I_e(\mu, \varphi) - I_r(\mu, \varphi)\} \sec 2\chi}{I(\mu, \varphi)} \end{aligned}$$

$$\begin{aligned} \text{and } P(\mu, \varphi) I(\mu, \varphi) \cos 2\chi &= I_e - I_r = (I - I_r) - I_r \\ &= I - 2I_r \end{aligned}$$

$$\text{or } 2I_r = I \left\{ 1 - P \cos 2\chi \right\}.$$

Therefore, it follows that

$$\begin{aligned} I_e^{(\text{ref})}(\mu, \varphi) &= 1/2 I^{(\text{ref})}(\mu, \varphi) \left\{ 1 + P(\mu, \varphi) \cos 2\chi \right\} \\ I_r^{(\text{ref})}(\mu, \varphi) &= 1/2 I^{(\text{ref})}(\mu, \varphi) \left\{ 1 - P(\mu, \varphi) \cos 2\chi \right\}. \end{aligned}$$

Each of these components is attenuated by the factor $e^{-\tau_1/\mu}$ in its outward passage through the atmosphere. Substituting the expression for $I^{(\text{ref})}(\mu, \varphi)$, we have the final expressions:

$$(7a) \quad \left[I_e(\mu, \varphi) \right]_{DD} = 1/2 \rho(\mu, \varphi) \pi F_0 \mu_0 e^{-\tau_1/\mu_0} e^{\tau_1/\mu} \left\{ 1 + P(\mu, \varphi) \cos 2\lambda \right\}$$

$$(7b) \quad \left[I_r(\mu, \varphi) \right]_{DD} = 1/2 \rho(\mu, \varphi) \pi F_0 \mu_0 e^{-\tau_1/\mu_0} e^{-\tau_1/\mu} \left\{ 1 - P(\mu, \varphi) \cos 2\lambda \right\}.$$

In considering the remaining three components, we have made the assumption that the scattering processes for these components obey the Rayleigh or molecular scattering law. This approximation is probably not a bad one for two reasons. First, the importance of these components diminishes with decreasing optical thickness, and secondly, the aerosol scattering matrix approaches the Rayleigh scattering matrix as the particle size approaches zero. The effect of the aerosol content is to increase the optical depth to $\tau_1 = .15$. The expression for $I_{Dd}(0; \mu, \varphi)$ is

$$(8) \quad \vec{I}_{Dd}(0; \mu, \varphi) = \frac{1}{4\pi\mu} \int_0^1 \int_0^{2\pi} \underline{T}(\tau; \mu, \varphi; \mu', \varphi') \vec{I}^{(ref)}(\mu', \varphi') d\mu' d\varphi'$$

There is little need in describing the computational schemes involved in this integral, as the details are available in an appendix to General Electric Technical Information Series R64SD74 (1964). The important thing to realize is that the term $\vec{I}^{(ref)}$ contains the measured values of ρ and P , which are introduced into the intensity components in the manner described in the section on $I_{DD}(\mu, \varphi)$.

For the remaining two components, I_{dD} and I_{dd} , one further assumption was imposed. Because of the difficulty in evaluating the downward diffusely transmitted light in the presence of a non-Lambertian surface, it was decided to idealize the surface to a Lambert surface reflecting with an albedo of $\bar{R} = \int_0^1 \int_0^\pi \rho(\mu, \varphi) \mu d\mu d\varphi$. This approximation is a good one

for two reasons. First, as noted before, these components are in general, small. Secondly, a computation of the downward diffusely transmitted light would involve an integration over the whole hemisphere, thus originating a tendency toward averaging. Actually, the problem is much more difficult than it appears, since an exact solution would require the solution of certain integral equations. In summary then, the components I_{dD} and I_{dd} will be approximated by introducing a Lambert surface with albedo \bar{R} . These intensities can readily be written in terms of the function γ_e , γ_r , and \bar{s} introduced by Chandrasekhar in the solution of the Lambert surface. For the sake of completeness, these expressions are given as follows:

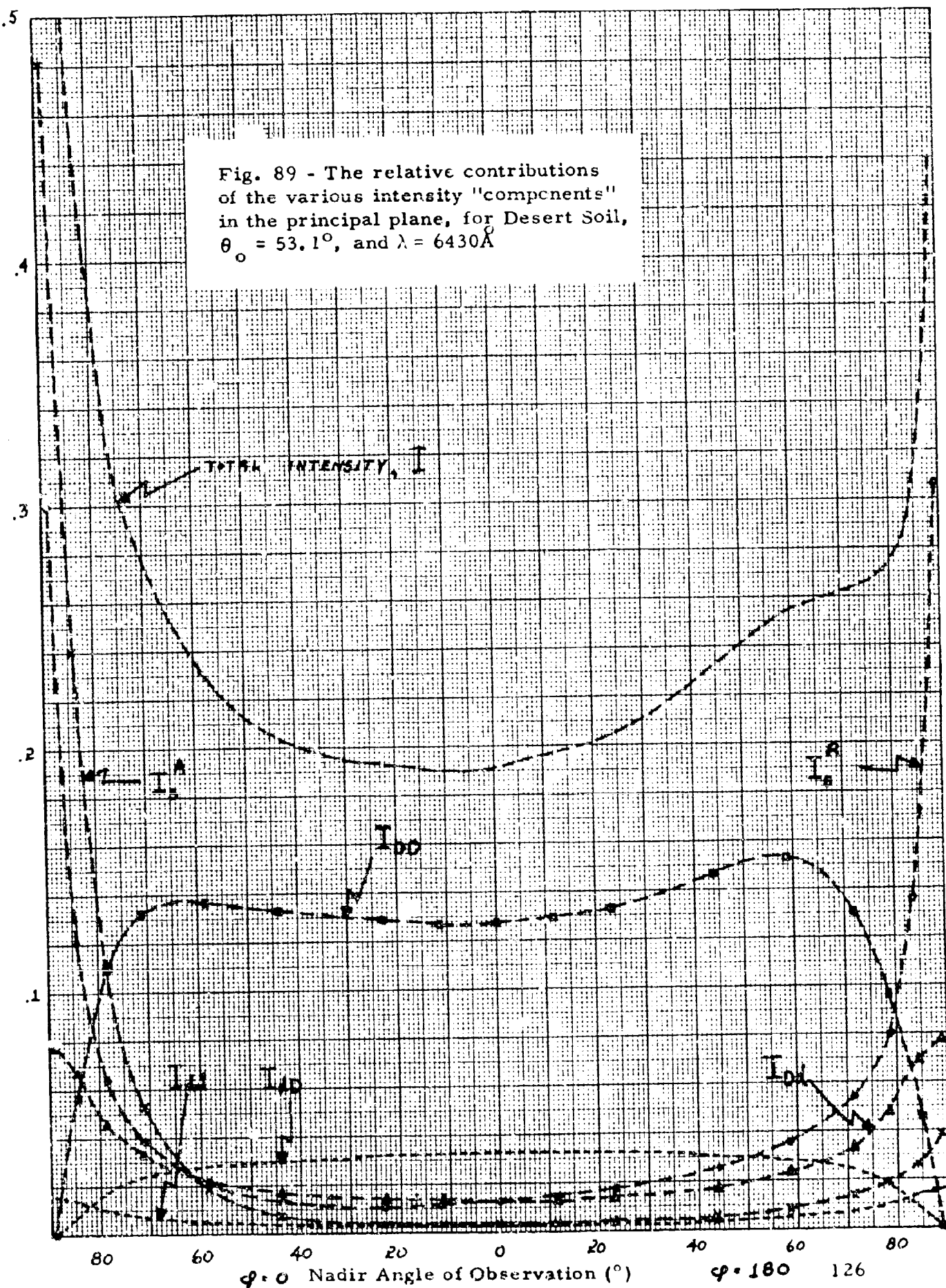
$$(9) \quad I_{dD}(\mu) = \mu_0 \pi F_0 \left\{ \frac{\gamma_e(\mu_0) + \gamma_r(\mu_0)}{2(1 - \frac{\bar{R}}{\bar{s}})} - e^{-\tau_1/\mu_0} \right\} \frac{\bar{R}}{\bar{\pi}} e^{-\tau_1/\mu}$$

$$(10) \quad I_{dd}(\mu) = \frac{\bar{R}}{2\pi} \mu_0 \pi F_0 \left\{ \frac{\gamma_e(\mu_0) + \gamma_r(\mu_0)}{2(1 - \frac{\bar{R}}{\bar{s}})} - e^{-\tau_1/\mu_0} \right\} \left\{ \gamma_e(\mu) + \gamma_r(\mu) - 2e^{-\tau_1/\mu} \right\}$$

The functions γ_e , γ_r , and \bar{s} have been tabulated by Sekera and collaborators (1952) for $\tau = .15$. Two things are noteworthy about the above expressions. First, they are azimuth independent. Secondly, their polarization is almost negligible so that the I_e and I_r components of each can both be taken equal to one half the value of the intensity.

This concludes a brief description of the various components considered in the calculation of the emergent intensity. As a matter of interest, the relative contribution of these various components in the sun's vertical is presented as figure 89. With these data, one can now compute the contrast

Fig. 89 - The relative contributions of the various intensity "components" in the principal plane, for Desert Soil, $\theta_0 = 53.1^\circ$, and $\lambda = 6430\text{\AA}$



attenuation coefficient, as previously described.

One further consideration remains, namely the computation of y_e and y_r at other azimuths. The intensity components I_e and I_r have been computed relative to the vertical plane through the observer's azimuth. What we now require are the intensity components parallel and normal to the plane of polarization. If the observer is situated in the sun's vertical plane, as is the case in the preceding figure, then there is no complication, since the sun's vertical coincides with the scattering plane and is normal to the plane of polarization. If this is not the case, then, in terms of angle χ , we have

$$(11a) \quad I_j = I_r^{(s)} = \frac{I_e \cos^2 \chi - I_r \sin^2 \chi}{\cos^2 \chi - \sin^2 \chi}$$

$$(11b) \quad I_i = I_e^{(s)} = \frac{I_r \cos^2 \chi - I_e \sin^2 \chi}{\cos^2 \chi - \sin^2 \chi}$$

V. Results of Computations

The results of the computations for the contrast attenuation coefficients are displayed in figures 90-94. As mentioned previously, these computations are for the "Desert Soil" sample, for a wavelength $\lambda = 6430\text{\AA}$, and for a sun zenith angle $\mu_0 = .60$ ($\theta_0 = 53.1^\circ$). Figure 90 shows the values of y_e , y , and y_r in the principal plane (i. e. the vertical plane containing the sun and the zenith). A point of interest is the fact that maximum values for both y_e and y are achieved on the solar side of the nadir. Figures 91, 92,

1.0

Fig. 90 - The constant attenuation coefficients as a function of Nadir angle in the principal plane, for $\theta_0 = 53.1^\circ$, and $\lambda = 6430\text{\AA}$

0.9

0.8

0.7

0.6

0.5

0.4

0.3

0.2

0.1

0

80

60

40

20

0

20

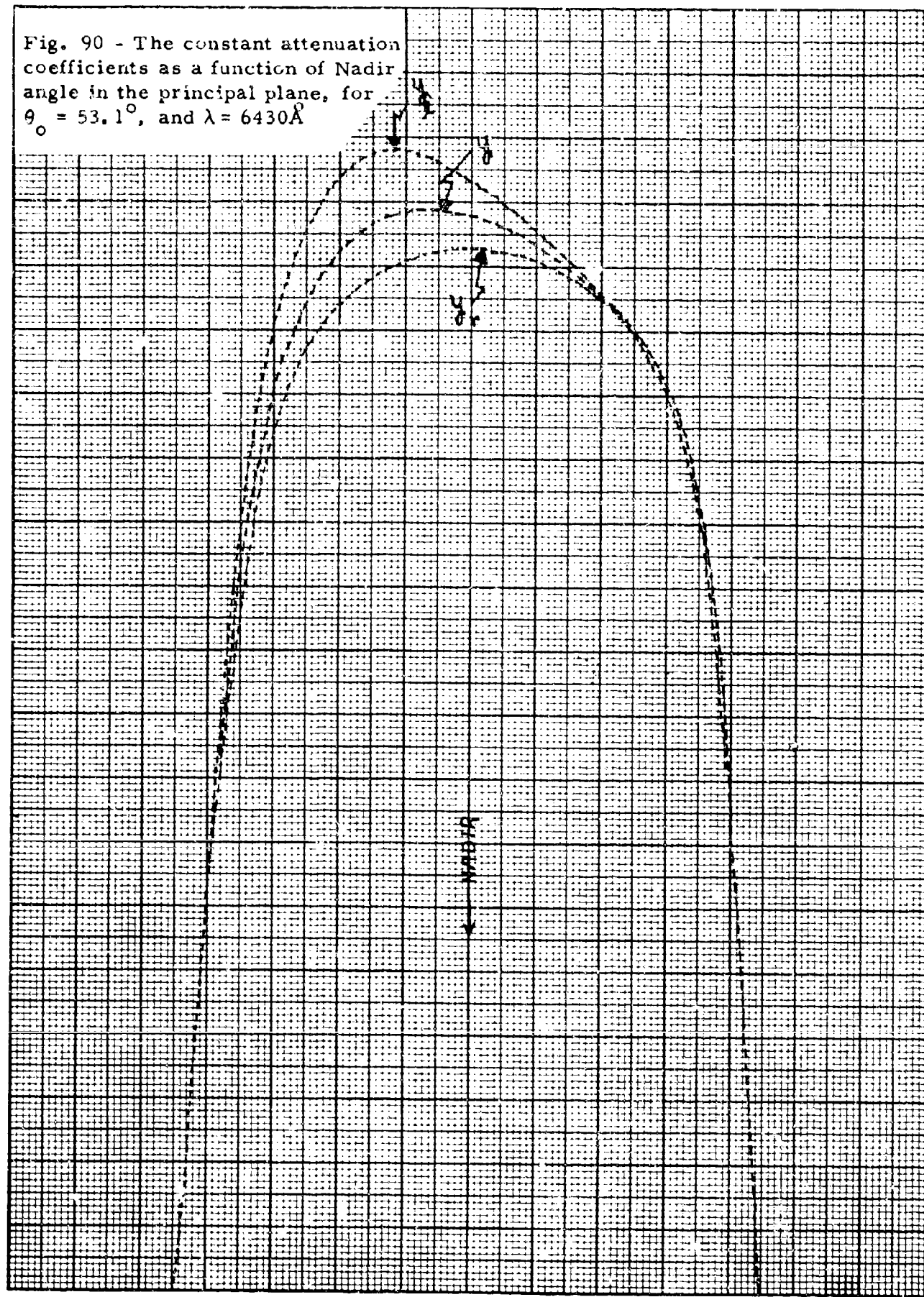
40

60

80

 $\phi = 0$ $\phi = 180$

128



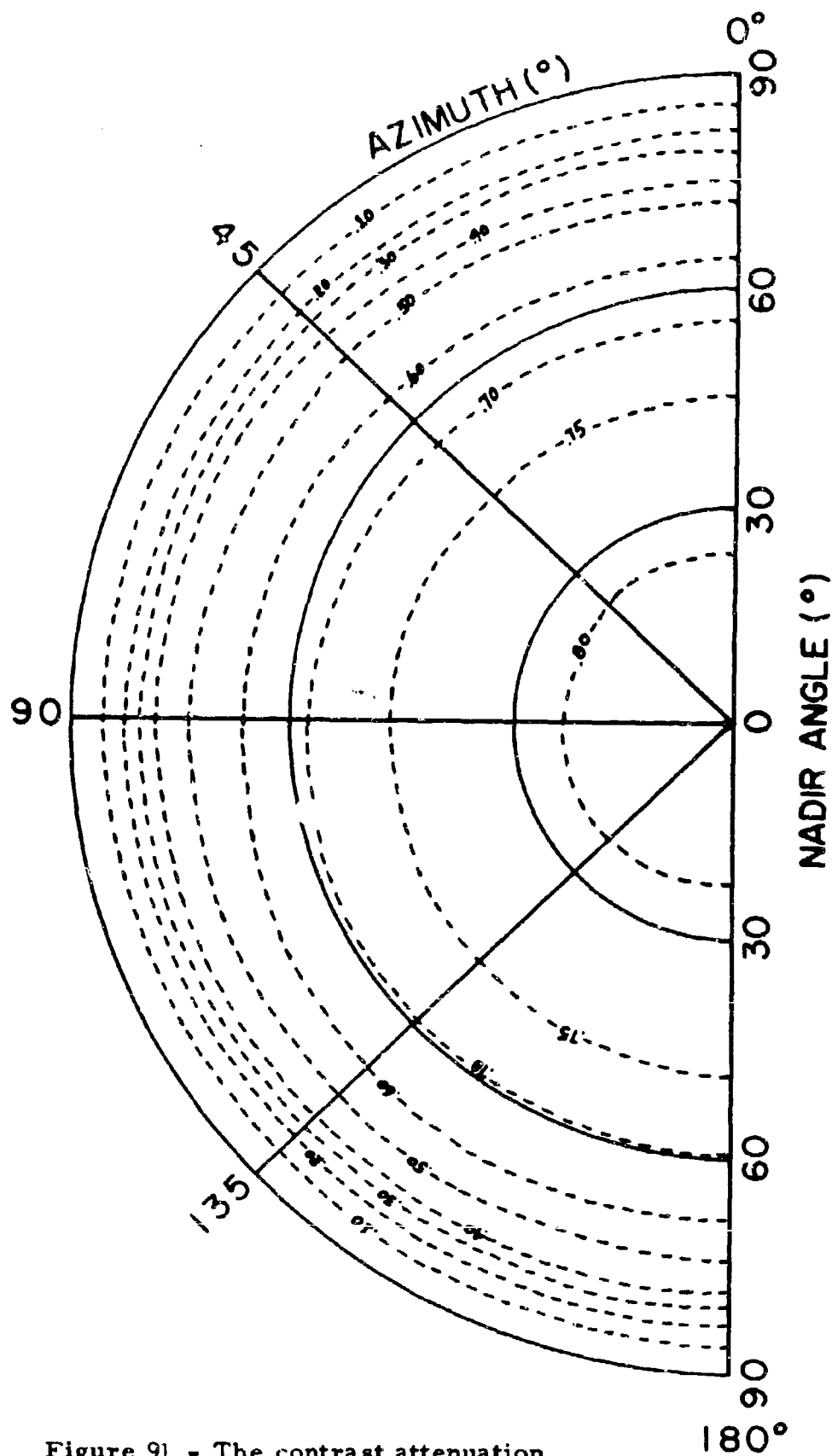


Figure 91 - The contrast attenuation coefficient y_r as a function of azimuth, θ_o for Desert Soil, $\theta_o = 53.1^\circ$, and $\lambda = 6430\text{\AA}$.

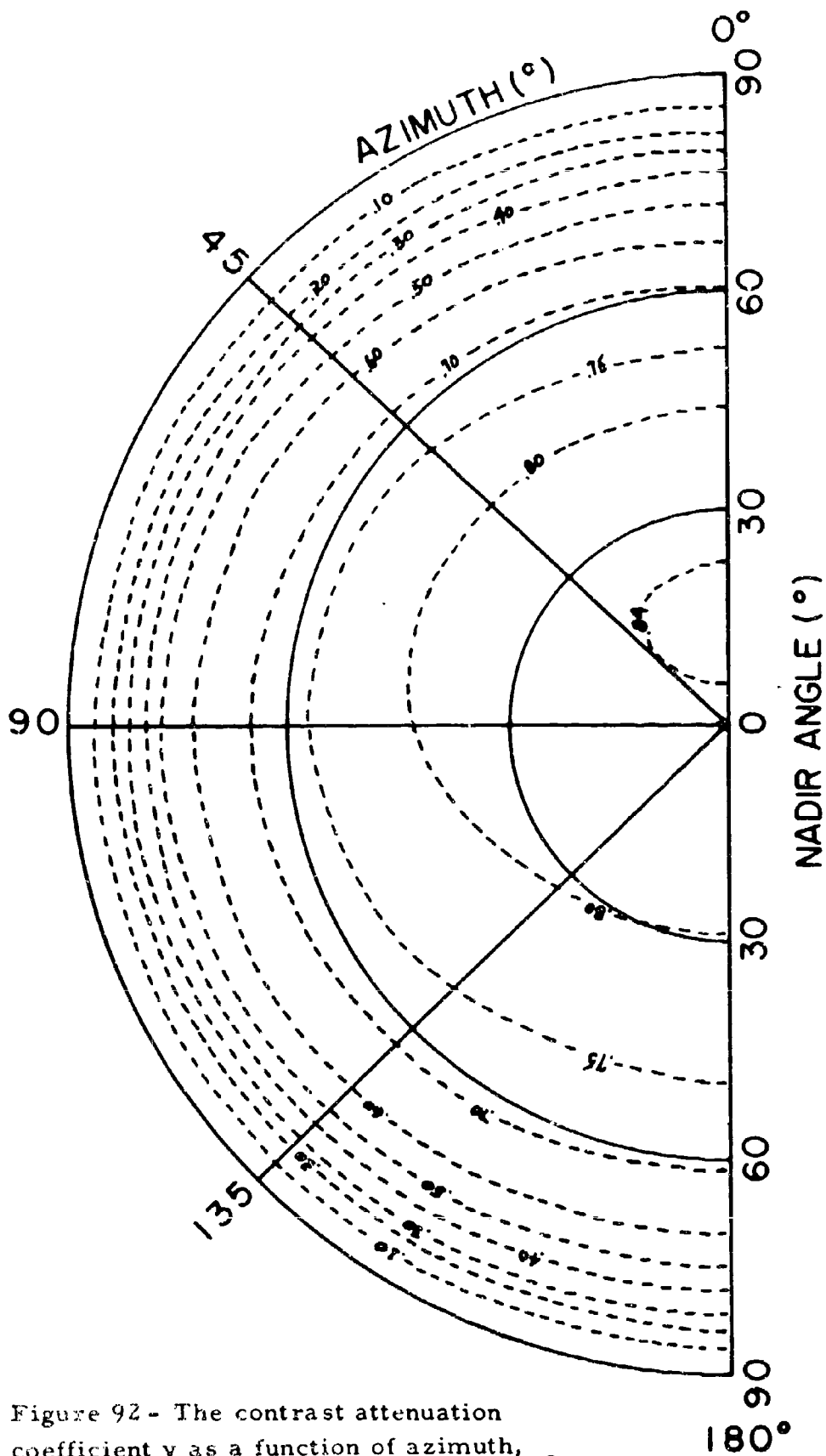


Figure 92 - The contrast attenuation coefficient y as a function of azimuth, for Desert Soil, $\theta_0 = 53.1^\circ$, and $\lambda = 6430\text{\AA}$.

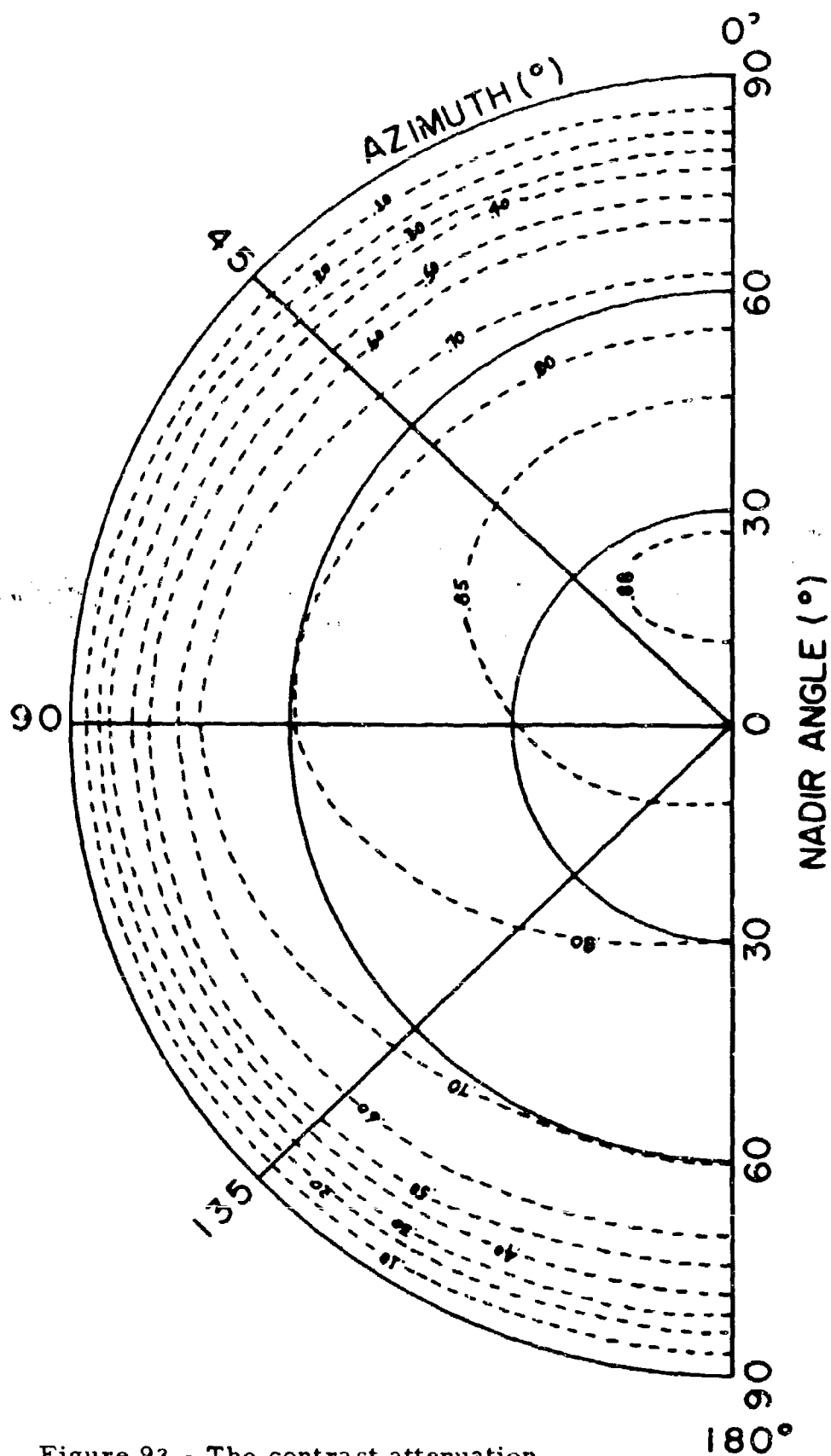


Figure 93 - The contrast attenuation coefficient y_e as a function of azimuth, for Desert Soil, $\theta_0 = 53.1^\circ$ and $\lambda = 6430 \text{ \AA}$.

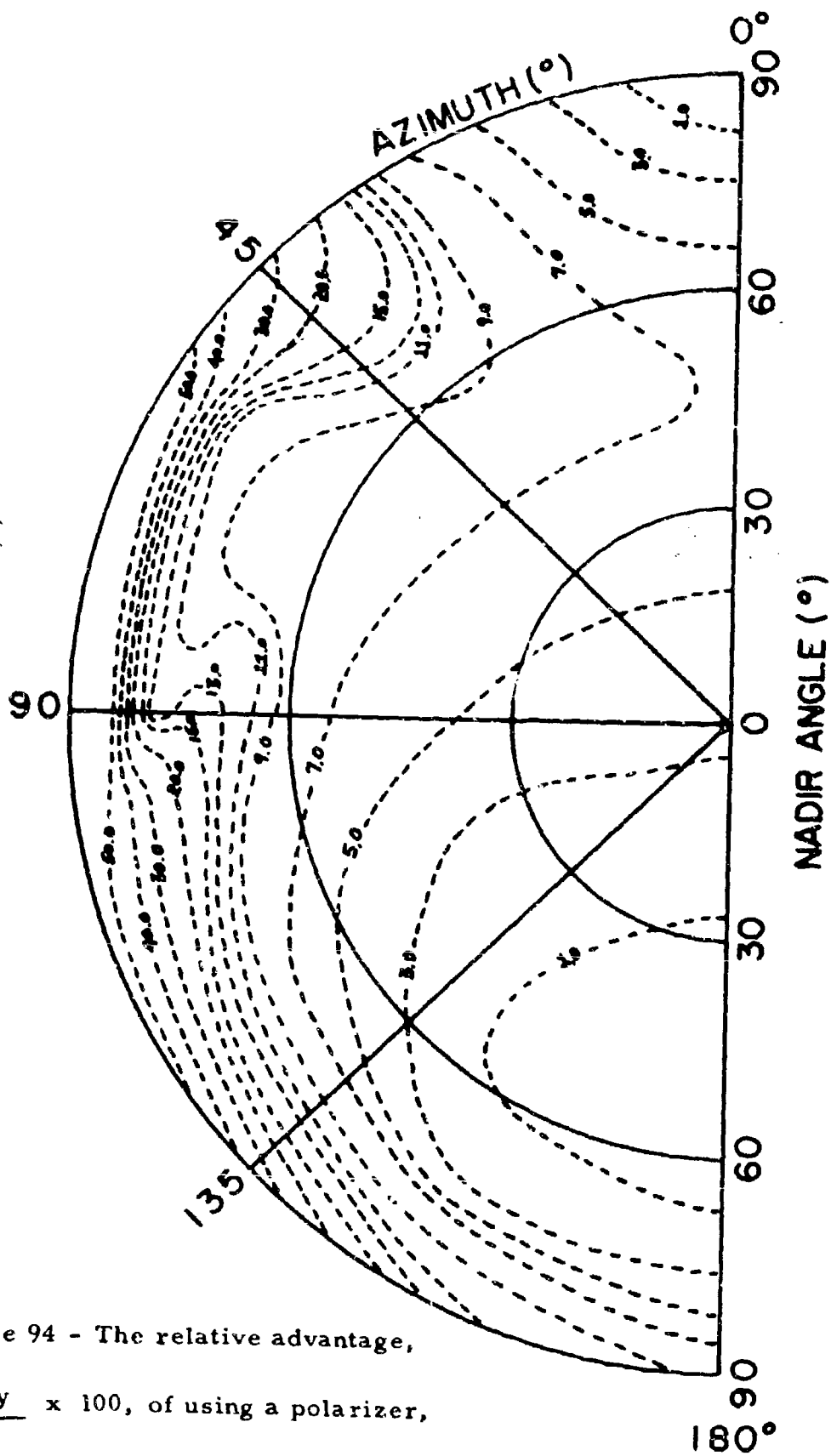


Figure 94 - The relative advantage,

$$\frac{y_e - y}{y} \times 100, \text{ of using a polarizer,}$$

as a function of azimuth, for Desert

Soil, $\theta_0 = 53^\circ.1$, and $\lambda = 6430\text{\AA}$.

and 93 are an extension of figure 90 and show the azimuth dependence of y_r , y , and y_e respectively. Again, the y and y_e plots clearly show the asymmetry with respect to the 90° azimuth.

While these figures show the direction of maximum contrast attenuation coefficient, it cannot be inferred that the apparent contrast is maximum in this direction, since the apparent contrast is the product of the "intrinsic" contrast and the contrast attenuation coefficient. However, in the absence of any knowledge concerning the "intrinsic" contrast, the curves do show in what directions the reduction in contrast due to atmospheric effects can be minimized.

Finally, the relative advantage of using a polarizer is given as a function of direction in figure 94. The relative advantage is defined by
$$\frac{y_e(\mu, \varphi) - y(\mu, \varphi)}{y(\mu, \varphi)} \times 100.$$
 A very strong gradient is seen toward the horizon in the 90° azimuth direction. However, as noted in the previous figures, the contrast attenuation coefficients approach zero as one looks toward the horizon.

VI. Recommended Further Research

As can be seen from the above results and discussion, a good start on an investigation of the problems of object detection by polarized light has been made on this project. There are, however, many aspects to the task, and it has not been possible within the scope of the present effort to cover all of the areas adequately. In view of the importance of this new and relatively unexploited approach to the problems of object detection, it is recommended that further work be devoted to the following specific

tasks:

1. Compute the contrast attenuation coefficients for additional types of surfaces.
2. Determine, for a number of selected cases of object-background combinations, the contrasts which one would observe at the top of the atmosphere.
3. Introduce additional types of atmospheric aerosol models and determine their effects on apparent contrasts as seen from the top of the atmosphere.
4. Extend the measurements to shorter and longer wavelengths.
5. Extend the measurements to more angles of incidence of the radiation and to the case of diffuse incident radiation.
6. Extend the measurements to other samples and surface conditions, and particularly to wet materials.

Most of the support work which would be required for these tasks has already been accomplished. Essentially all of the computer programs have been written and actually run on the machine, so the computation of additional cases is straight forward. The present instrument would require only relatively minor modifications for the additional measurements, and the personnel are now completely checked out on its operation. An extension of the research without interruption is strongly recommended.

References

- Anderson, E. R. (1952) - "Energy Budget Studies. Water-Loss Investigations, Vol. 1 - Lake Hefner Studies," U. S. Geol. Survey Circ. No. 229.
- Ashburn, E. V. and R. G. Weldon (1956) - "Spectral Diffuse Reflectance of Desert Surfaces," Journ. Opt. Soc. Am., 46:8, 583-586.
- Bauer, K. G. and J. A. Dutton (1962) - "Albedo Variations Measured from an Airplane over Several Types of Surface," Jour. Geophys. Res., 67:6,
- Brewster, Sir David (1865) - "On the polarization of light by rough and white surfaces," Trans. Roy. Soc. Edinburgh, XXIII, 205-210.
- Chandrasekhar, S. (1950) - Radiative Transfer, Oxford, Clarendon Press, 385 pp.
- Christie, A. W. (1953) - "The Luminous Directional Reflectance of Snow," Jour. Opt. Soc. Am., 43:7, 621-622.
- Coulson, K. L. (1956) - "Characteristics of Solar Radiation Reflected from Desert Soil," Sci. Rept. No. 2, Contr. AF 19(604)-1303, Univ. of California, Los Angeles, 21 pp.
- Coulson, K. L., J. V. Dave, and Z. Sekera (1960), Tables Related to Radiation Emerging from a Planetary Atmosphere, University of California Press.
- Coulson, K. L., G. M. B. Bouricius, and E. L. Gray (1964), "Effect of Surface Properties on Planet-Reflected Sunlight," General Electric Technical Information Series R64SD74.
- Cox, C. and W. Munk (1955) - "Some Problems in Optical Oceanography," Jour. Marine Res., 14:1, 63-78.
- Deirmendjian, D., (1955) - "The Optical Thickness of the Molecular Atmosphere," Archiv Meteor., Geophys. U. Bioklim, Serie B, vol. 6, p. 452.
- Deirmendjian, D. (1957) Annales de Geophysique, Vol. 13, p. 286.
- Deirmendjian, D. (1959) - "Theory of the Solar Aureole, Part II: Applications to Atmospheric Models", Annales de Geophysique, Vol. 15, p. 218.
- van Diggelen, J. (1959) - "Photometric properties of lunar crater floors," Rech. Obs. Utrecht, 14, 1-114. (NASA TTF-209)

References

Dollfus, A. (1957) - Supplement No. 4, Ann. d'Astrophys.

Dollfus, A. (1961) - "Polarization Studies of the Planets," Chap 9 in Planets and Satellites, Ed. - G. P. Kuiper and B. M. Middlehurst, Univ. of Chicago Press.

Fraser, R. S., (1959) - "Scattering Properties of Atmospheric Aerosols," University of California, Department of Meteorology, Los Angeles, Scientific Report No. 2.

Fraser, R. S., (1964) - "Apparent Contrast of Objects on the Earth's Surface as Seen from above the Earth's Atmosphere," Journal of the Optical Society of America, Vol. 54, p. 289.

Hapke, B. and H. Van Horn (1963) - "Photometric Studies of Complex Surfaces, with Applications to the Moon," Jour. Geophys., Res., 68:15, 4545-4570.

Kondrat'ev, K. Ia and M. P. Manolova (1955) - K voprasu o prikhode rasseiannoi i summarnoi radiatsii na poverkhnost' sklona [The problem of incoming diffuse and total radiation on the surface of a slope], Meteorologiya i Gidrologiya, Leningrad, No. 6: 31-34.

Krinov, E. L. (1947) - "Spektral' naia otrazhatel' naia sposobnost' prirodnykh obrazovaniy," Laboratoriia Aerometodov, Akad. Nauk, SSSR, Moscow, 271 pp. ("Spectral reflectance properties of natural surfaces," Technical Translation TT-439, National Research Council of Canada, Ottawa - 1953).

Lyot, B. and A. Dollfus (1949) - "Polarisation de la lumiere cendree de la Lune," Comptes Rendus Acad. Sci. Paris, 228, 1773-1775.

Middleton, W. E. K. and A. G. Mungall (1952) - "The Luminous Directional Reflectance of Snow," Jour. Opt. Soc. Am., 42:6, 572-579.

Miller, D. H. (1955) - "Snow Cover and Climate in the Sierra Nevada, California," Univ. of California Publications in Geography, Vol. 11, 218 pp.

Orlova, N. S. (1952) - "Radial diagrams of scattering for several materials," Trudy Astron. Obs., Leningrad State Univ., 16, 166-193.

Penndorf, R. (1954) - "The Vertical Distribution of Mie Particles in the Troposphere," J. of Meteorology, 11:3, 245-247.

Sekera, Z. (1956) - "Recent Developments in the Study of the Polarization of Skylight," Advances in Geophysics, 3, p. 43.

References

Sekera, Z., and G. Blanch (1952) - "Tables Relating to Rayleigh Scattering of Light in the Atmosphere," Contract No. AF 19(122)-239, University of California, Department of Meteorology, Los Angeles.